

UNIVERSITY OF CALIFORNIA
SANTA CRUZ

**SEARCH FOR WW AND WZ RESONANCE PRODUCTION IN
 $\ell\nu qq$ FINAL STATES IN pp COLLISIONS AT $\sqrt{s} = 13$ TEV WITH
THE ATLAS DETECTOR**

A dissertation submitted in partial satisfaction of the
requirements for the degree of

DOCTOR OF PHILOSOPHY

in

PHYSICS

by

Natasha Woods

December 2019

The Dissertation of Natasha Woods
is approved:

Abraham Seiden, Chair

Mike Hance

Bruce Schumm

Quentin Williams
Vice Provost and Dean of Graduate Studies

Copyright © by

Natasha Woods

2019

Table of Contents

List of Figures	vi
List of Tables	xv
Abstract	xvii
Dedication	xviii
Acknowledgments	xix
I Theoretical Motivation	2
1 The Standard Model of Particle Physics	3
1.1 Introduction	3
1.2 Quantum Field Theory	3
1.3 $U(1)_{EM}$ Local Gauge Invariance	4
1.4 Yang-Mills Gauge Theories	7
1.5 Particles in the Standard Model	8
1.6 Higgs Mechanism	13
1.7 Electroweak Theory	14
1.8 Quantum ChromoDynamics	15
2 Standard Model Successes and Limitations	20
3 New Physics Models with Diboson Resonances	23
3.1 Randall Sundrum Bulk Model	23
3.2 Extended Scalar Sector	25
3.3 Simple Standard Model Extensions	26

II Experimental Setup	29
4 LHC	30
4.1 LHC Layout and Design	32
5 The ATLAS Detector	37
5.1 Coordinate System	39
5.2 Inner Detector	40
5.2.1 Pixel Detector	43
5.2.2 Semiconductor Tracker	43
5.2.3 Transition Radiation Tracker	43
5.3 Calorimeters	45
5.4 Muon Spectrometer	49
5.5 Magnet System	53
5.6 Trigger System	54
III Method	56
6 Dataset and Simulated Samples	57
6.1 Dataset	57
6.2 Simulated Samples	60
6.3 Object Selection	60
6.3.1 Electrons	60
6.3.2 Muons	61
6.3.3 small-R jets	63
6.3.4 large-R jets	66
6.3.5 Variable Radius jets	69
6.3.6 MET/neutrinos	69
6.3.7 Jet Flavor Tagging	69
6.3.8 Overlap Removal	70
7 Event Selection and Categorization	71
7.1 Pre-selection	71
7.2 Trigger	71
7.3 GGF/VBF RNN	73
7.4 Topological Cuts	78
7.5 Selection Acceptance times efficiency for Signal Events	88
7.6 Background Estimate	89
7.6.1 Control Regions	89
7.6.2 Fake Lepton Backgrounds	89

8 Systematic Uncertainties	103
8.1 Experimental Systematics	103
8.2 Theory Systematics	105
9 Statistical Analysis	113
9.1 Likelihood Function Definition	113
9.2 Fit Configuration	114
9.3 Best Fit μ	116
9.4 Discovery Test	117
9.5 Exclusion Limits	118
IV Results	120
10 Statistical Interpretation	121
10.1 Discovery Tests	121
10.2 Systematic Profiling and Correlations	127
10.3 Expected and Measured Yields	128
10.4 Limits	142
V Quark and Gluon Tagging	144
11 Prospects	145
12 n_{trk} Calibration	152
13 Application	158
VI Conclusion	163
14 Conclusions	164
Bibliography	165

List of Figures

1.1	The particles of the Standard Model.	10
1.2	Summary of how Standard Model particles interact with other Standard Model particles.	11
1.3	This figure shows the three dominant QCD interactions. From Ref. [14]	17
1.4	Strength of the U(1), SU(2), and SU(3) gauge couplings as a function of the energy scale of the interaction (Q). From Ref. [10]	18
2.1	A comparison of cross section measurements at $\sqrt{s} = 7, 8, 13$ TeV from ATLAS compared to theoretical measurements. From Ref. [5]	22
3.1	Cartoon of RS Bulk Model	24
4.1	Scaling of cross sections with \sqrt{s} . Natasha: write more here	31
4.2	LHC Layout. Natasha write more	33
4.3	LHC Accelerator. Natasha write more	35
5.1	Big picture layout of ATLAS detector. Natasha: write more	38
5.2	Big picture layout of ATLAS detector. Natasha: write more	38
5.3	A simplified schematic of how different particles interact and are detected within ATLAS.	39
5.4	Layout of ATLAS Inner Detector	41
5.5	Layout of ATLAS ID Barrel System.	42
5.6	Overview of ATLAS electromagnetic and hadronic calorimeters.	46

5.7	Schematic of ECAL	47
5.8	Schematic of HCAL	48
5.9	Schematic of Muon Spectrometer [cite G35]	51
5.10	Schematic of MDT chamber. [cite G35]	52
5.11	Schematic of RPC chamber, which is used for triggering in the central region of the detector [cite G35].	52
5.12	Schematic of TGC chamber, which is used for triggering in the muon end-cap region. [cite G35]	53
5.13	Layout of ATLAS magnet systems.	54
6.1	Integrated luminosity for data collected from ATLAS from 2011 - 2018	58
6.2	Mean number of interactions per crossing for data collected from ATLAS from 2011 - 2018	59
6.3	This figure shows the breakdown of the muon reconstruction efficiency scale factor measured in $Z \rightarrow \mu\mu$ as a function of p_T [4].	63
6.4	[6] This diagram shows the calibration stages for EM jets.	66
6.5	The upper cut on D_2 (a) and jet mass window cut i.e. the upper and lower boundary of the mass (b) of the W -tagger as a function of jet p_T . Corresponding values for Z -tagger are shown in (c) and (d). The optimal cut values for maximum significance are shown as solid markers and the fitted function as solid lines. Working points from $VV \rightarrow JJ$ [ATLAS-HDBS-2018-31-002] is also shown as dashed lines as a reference. Natasha reword?	68
6.6	Natasha write caption	68
7.1	RNN architecture. Natasha add caption	75
7.2	RNN Score distribution for ggF and VBF signals and backgrounds.	76
7.3	ROC curve using k-fold validation for RNN.	77

7.4	Comparison of GGF Z' limits for different RNN score selections. The bottom panel shows the ratio of the upper limits set for different RNN cuts to the cut-based analysis. In this panel smaller numbers, indicate that the expected upper limit is smaller than the cut-based analysis, which is desired.	78
7.5	Event Categorization. Natasha write more.	81
7.6	Data MC comparison for the merged WW HP TCR. The bottom panel shows the ratio of the difference between data and simulation to simulation. The red bands include the all systematic and statistical uncertainties on the background.	82
7.7	Data MC comparison for the merged WW LP TCR. The bottom panel shows the ratio of the difference between data and simulation to simulation. The red bands include the all systematic and statistical uncertainties on the background.	83
7.8	Data MC comparison for the merged WZ HP TCR. The bottom panel shows the ratio of the difference between data and simulation to simulation. The red bands include the all systematic and statistical uncertainties on the background.	84
7.9	Data MC comparison for the merged WZ LP TCR. The bottom panel shows the ratio of the difference between data and simulation to simulation. The red bands include the all systematic and statistical uncertainties on the background.	85
7.10	Data MC comparison for the resolved WW TCR. The bottom panel shows the ratio of the difference between data and simulation to simulation. The red bands include the all systematic and statistical uncertainties on the background.	86
7.11	Data MC comparison for the resolved WZ TCR. The bottom panel shows the ratio of the difference between data and simulation to simulation. The red bands include the all systematic and statistical uncertainties on the background.	87

7.12 Selection acceptance times efficiency for the $W' \rightarrow WZ \rightarrow \ell\nu qq$ events from MC simulations as a function of the W' mass for (a) Drell-Yan and (b) VBF production, combining the merged HP and LP signal regions of the $WW \rightarrow \ell\nu J$ selection and the resolved regions of the $WW \rightarrow \ell\nu jj$ selection.	88
7.13 Selection acceptance times efficiency for the $G \rightarrow WW \rightarrow \ell\nu qq$ events from MC simulations as a function of the G mass for (a) Drell-Yan and (b) VBF production, combining the merged HP and LP signal regions of the $WW \rightarrow \ell\nu J$ selection and the resolved regions of the $WW \rightarrow \ell\nu jj$ selection.	89
7.14 The E_T^{miss} distribution in MJCR for 2017 data in the electron channel(left), muon channel with W-boson pT < 150 GeV (center) and > 150 GeV (right). Multi-jet templates are calculated as remaining data components after excluding known MC	91
7.15 Postfit Data/MC comparison of distributions of E_T^{miss} , m_T^W , lepton and neutrino p_T , $m_{\ell\nu jj}$, lepton- ν angular distance in the WW electron channel. The MJ template is obtained from the pre-MJ-fit.	92
7.16 Postfit Data/MC comparison of distributions of E_T^{miss} , m_T^W , lepton and neutrino p_T , $m_{\ell\nu jj}$, lepton- ν angular distance in the WW muon channel. The MJ template is obtained from the pre-MJ-fit.	93
7.17 Postfit Data/MC comparison of distributions of E_T^{miss} , m_T^W , lepton and neutrino p_T , $m_{\ell\nu jj}$, lepton- ν angular distance in the WZ untag electron channel. The MJ template is obtained from the pre-MJ-fit.	94
7.18 Postfit Data/MC comparison of distributions of E_T^{miss} , m_T^W , lepton and neutrino p_T , $m_{\ell\nu jj}$, lepton- ν angular distance in the WZ untag muon channel. The MJ template is obtained from the pre-MJ-fit.	95
7.19 Postfit Data/MC comparison of distributions of E_T^{miss} , m_T^W , lepton and neutrino p_T , $m_{\ell\nu jj}$, lepton- ν angular distance in the WZ untag electron channel. The MJ template is obtained from the pre-MJ-fit.	96

7.20 Postfit Data/MC comparison of distributions of E_T^{miss} , m_T^W , lepton and neutrino p_T , $m_{\ell\nu jj}$, lepton- ν angular distance in the WZ untag muon channel. The MJ template is obtained from the pre-MJ-fit.	97
7.21 Postfit Data/MC comparison of distributions of E_T^{miss} , m_T^W , lepton and neutrino p_T , $m_{\ell\nu jj}$, lepton- ν angular distance in the VBF WW electron channel. The MJ template is obtained from the pre-MJ-fit.	98
7.22 Postfit Data/MC comparison of distributions of E_T^{miss} , m_T^W , lepton and neutrino p_T , $m_{\ell\nu jj}$, lepton- ν angular distance in the VBF WW muon channel. The MJ template is obtained from the pre-MJ-fit.	99
7.23 Postfit Data/MC comparison of distributions of E_T^{miss} , m_T^W , lepton and neutrino p_T , $m_{\ell\nu jj}$, lepton- ν angular distance in the VBF WZ electron channel. The MJ template is obtained from the pre-MJ-fit.	100
7.24 Postfit Data/MC comparison of distributions of E_T^{miss} , m_T^W , lepton and neutrino p_T , $m_{\ell\nu jj}$, lepton- ν angular distance in the VBF WZ muon channel. The MJ template is obtained from the pre-MJ-fit.	101
8.1 The W/Z+jet systematics for the a) Merged ggF, b) Resolved ggF, c) Merged VBF, and d) Resolved VBF regions. The top subplot shows the nominal and variation distributions/bands, the middle shows the ratio of the two, and the final shows just the shape of the envelope (the final uncertainty).	107
8.2 The two-point generator comparison between Sherpa and MadGraph for the W/Z+jet samples in the a) Merged ggF, b) Resolved ggF, c) Merged VBF, and d) Resolved VBF regions. The normalization of the Madgraph sample is set to the Sherpa value to consider only shape effects. The bottom inlet shows the ratio of the two.	108
8.3 Ratio between the variations of generator (red) and hadronization (blue) variations for the Merged regime for $t\bar{t}$ sample.	109
8.4 Ratio between the variations of generator (red) and hadronization (blue) variations for the Resolved regime for $t\bar{t}$ sample.	109

8.5	Ratio between the variations of ISR up (red) and down (blue) variations for the Merged regime for $t\bar{t}$ sample.	110
8.6	Ratio between the variations of ISR up (red) and down (blue) variations for the Resolved regime for $t\bar{t}$ sample.	111
8.7	Ratio between the variations of FSR up (red) and down (blue) variations for the Merged regime for $t\bar{t}$ sample.	112
8.8	Ratio between the variations of FSR up (red) and down (blue) variations for the Resolved regime for $t\bar{t}$ sample.	112
9.1	The HVT signal mass resolution as a function of mass fit with a straight line in the Resolved ggF region (left) and VBF (right) region.	116
9.2	The HVT signal mass resolution as a function of mass fit with a straight line in the Merged ggF region (left) and VBF (right) region.	116
10.1	These plots show the measured p_0 value as a function of resonance mass for HVT Z' DY production.	122
10.2	These plots show the measured p_0 value as a function of resonance mass for HVT Z' VBF production.	123
10.3	These plots show the measured p_0 value as a function of resonance mass for HVT W' DY production.	124
10.4	These plots show the measured p_0 value as a function of resonance mass for HVT W' VBF production.	125
10.5	These plots show the measured p_0 value as a function of resonance mass for the RS Graviton DY production.	126
10.6	Ranked systematics and their fitted values for WW DY (right) and VBF (left) selections.	127
10.7	Ranked systematics and their fitted values for WZ DY (right) and VBF (left) selections.	128
10.8	Correlations between systematics for WW DY (right) and VBF (left) selections.	128

10.9 This figure shows the distribution of $m_{\ell\nu qq}$ in the DY WW control regions.	136
10.10 This figure shows the distribution of $m_{\ell\nu qq}$ in the DY WZ control regions.	137
10.11 This figure shows the distribution of $m_{\ell\nu qq}$ in the VBF WW control regions.	138
10.12 This figure shows the distribution of $m_{\ell\nu qq}$ in the VBF WZ control regions.	139
10.13 This figure shows the distribution of $m_{\ell\nu qq}$ in the GGF WW signal regions.	140
10.14 This figure shows the distribution of $m_{\ell\nu qq}$ in the GGF WZ Untag signal regions.	140
10.15 This figure shows the distribution of $m_{\ell\nu qq}$ in the GGF WZ Tag signal regions.	141
10.16 This figure shows the distribution of $m_{\ell\nu qq}$ in the VBF WZ Tag signal regions.	141
10.17 This figure shows the distribution of $m_{\ell\nu qq}$ in the VBF WZ Tag signal regions.	142
10.18 This figure shows theory, expected and observed limits for HVT W' DY (left) and VBF (right) production.	142
10.19 This figure shows theory, expected and observed limits for HVT Z' DY (left) and VBF (right) production.	143
10.20 This figure shows theory, expected and observed limits for RS Gravitons via DY production.	143
11.1 PDGID of the truth-level parton matched to the small-R jets passing the Resolved GGF WW Signal Region selections for the (a) Leading (b) Sub-Leading jets . These distributions are shown for 300, 500, and 700GeV Z' signals and the background.	147

11.2 The number of tracks in small-R jets in events passing the Resolved GGF WW Signal Region selections for the (a) Leading (b) Sub-Leading jets. These distributions are shown for 300, 500, and 700GeV Z' signals and the background.	147
11.3 The number of tracks in background small-R jets in events passing the Resolved GGF WW Signal region selection vs. $\ln(p_T)$ for (a)Leading (b) Sub-Leading jets. The best fit line for the distribution is also shown, as well as the percentage of jets that pass a cut of number of tracks $< 4 \times \ln(p_T) - 5$. Note the number of total entries in these plots has been normalized to one.	148
11.4 The number of tracks in small-R jets in 300GeV Z' events passing the Resolved GGF WW Signal region selection vs. $\ln(p_T)$ for (a)Leading (b) Sub-Leading jets. The best fit line for the distribution is also shown, as well as the percentage of jets that pass a cut of number of tracks $< 4 \times \ln(p_T) - 5$.Note the number of total entries in these plots has been normalized to one.	148
11.5 The number of tracks in small-R jets in 500GeV Z' events passing the Resolved GGF WW Signal region selection vs. $\ln(p_T)$ for (a)Leading (b) Sub-Leading jets. The best fit line for the distribution is also shown, as well as the percentage of jets that pass a cut of number of tracks $< 4 \times \ln(p_T) - 5$.Note the number of total entries in these plots has been normalized to one.	149
11.6 The number of tracks in small-R jets in 700GeV Z' events passing the Resolved GGF WW Signal region selection vs. $\ln(p_T)$ for (a)Leading (b) Sub-Leading jets. The best fit line for the distribution is also shown, as well as the percentage of jets that pass a cut of number of tracks $< 4 \times \ln(p_T) - 5$.Note the number of total entries in these plots has been normalized to one.	149

11.7 The number of tracks in leading small-R jets in background events passing the Resolved GGF WW Signal region selection vs. $\ln(p_T)$ for (a)Gluons (b) Quarks jets. The best fit line for the distribution is also shown, as well as the percentage of jets that pass a cut of number of tracks $< 4 \times \ln(p_T) - 5$.Note the number of total entries in these plots has been normalized to one.	150
11.8 ROC Curve for Quark and Gluon Tagging with a cut on the number of tracks that depends on the $\ln(p_T)$	150
11.9 The top panel shows the distribution of m_{lvqq} with and without quark gluon tagging. The middle panel shows the ratio of the signals and backgrounds with and without quark gluon tagging. The bottom panel shows the change in S/\sqrt{B} with quark gluon tagging.	151
13.1 The top panel shows the distribution of m_{lvqq} with and without requiring jets to be true quarks. The middle panel shows the ratio of the signals and backgrounds with and without requiring jets to be true quarks. The bottom panel shows the change in S/\sqrt{B} when requiring jets to be true quarks.	159
13.2 Unfolded and extracted n_C qg dstbs.	160
13.3 PDGID of the truth-level parton matched to the small-R jets passing the Resolved GGF WW Signal Region selections for the (a) Leading (b) Sub-Leading jets . These distributions are shown for 300, 500, and 700GeV Z' signals and the background.	161
13.4 These figures show the impact of the uncertainties on the number of tracks in the leading jet in the sum of the background sample in the Resolved GGF WW SR (a) tracking efficiency (b) fake (c) PDF (d) ME (e) unfolding uncertainties.	162

List of Tables

1.1	Representations of the SM fermions under $SU(3)_C \times SU(2)_L \times U(1)_Y$ gauge symmetry group. $SU(2)_L$ gauge transformations allow one to go between rows and $SU(3)_C$ transformations allow one to go between columns in these fermion representations. [REWORD]	9
7.1	The list of triggers used in the analysis.	72
7.2	Summary of selection criteria used to define the signal region (SR), W +jets control region (W CR) and $t\bar{t}$ control region ($t\bar{t}$ CR) for merged 1-lepton channel.	80
7.3	The list of selection cuts in the resolved analysis for the WW and WZ signal regions (SR), W +jets control region (WR) and $t\bar{t}$ control region (TR).	81
7.4	Definitions of “inverted” leptons used in multijet control region . .	91
7.5	Fit validation result in WCRs for 2015+16 data. The fit is done in various WCRs, in order to obtain the corresponding scale factors for MJ templates: ggF resolved WCR for the $WW \rightarrow lvqq$ selection, ggF resolved untagged WCR for the $WZ \rightarrow lvqq$ selection, ggF resolved tagged WCR for the $WZ \rightarrow lvqq$ selection, VBF resolved WCR for the $WW \rightarrow lvqq$ selection, and VBF resolved WCR for the $WZ \rightarrow lvqq$ selection. Post-fit event yields for electroweak processes and MJ contributions are shown. The SF column shows the corresponding normalization scale factors for electroweak processes from the fit. R.U. stands for relative uncertainty.	102

10.1	Expected and Measured for DY WW $W+\text{jets}$, $t\bar{t}$ control regions and signal regions.	129
10.2	Expected and Measured for DY WZ $W+\text{jets}$, $t\bar{t}$ tag and untag control regions.	130
10.3	Expected and Measured for DY WZ $W+\text{jets}$, $t\bar{t}$ tag and untag signal regions.	131
10.4	Expected and Measured for VBF WW $W+\text{jets}$, $t\bar{t}$ control regions and signal regions.	132
10.5	Expected and Measured for VBF WZ $W+\text{jets}$, $t\bar{t}$ control regions and signal regions.	133
10.6	Fitted background normalizations for $t\bar{t}$ and $W+\text{jets}$ backgrounds for the DY WW analysis region.	134
10.7	Fitted background normalizations for $t\bar{t}$ and $W+\text{jets}$ backgrounds for the DY WZ analysis region.	134
10.8	Fitted background normalizations for $t\bar{t}$ and $W+\text{jets}$ backgrounds for the VBF WW analysis region.	134
10.9	Fitted background normalizations for $t\bar{t}$ and $W+\text{jets}$ backgrounds for the VBF WZ analysis region.	135

Abstract

Search for WW and WZ resonance production in $\ell\nu qq$ final states in pp collisions at $\sqrt{s} = 13$ TeV with the ATLAS detector

by

Natasha Woods

This thesis reviews a search for WW and WZ resonance production using data from pp collisions at $\sqrt{s} = 13$ TeV using the ATLAS detector, corresponding to an integrated luminosity of 139 fb^{-1} . Diboson resonances are predicted in a number of Standard Model (SM) extensions, such as Extended Gauge Models, Extra dimensions, and technicolor models. This search looks for resonances where one W boson decays leptonically and the other W or Z boson decays hadronically. This search is sensitive to diboson resonance production via vector-boson fusion as well as quark-antiquark annihilation and gluon-gluon fusion mechanisms. No significant excess of events is observed with respect to the Standard Model backgrounds. As the dominant backgrounds in this search contain gluons, classifying jets as quark or gluon initiated would make this analysis more sensitive to new physics. Towards this end, this thesis considers the prospects for adding a quark gluon tagger based on the number of tracks in jets and reviews the calibration of the number of tracks in jets.

A loving dedication.

å

xviii

Acknowledgments

Proper acknowledgments of everyone else who helped you graduate. Write later.

₁ another intro???

²

Part I

³

Theoretical Motivation

⁴ **Chapter 1**

⁵ **The Standard Model of Particle
6 Physics**

⁷ **1.1 Introduction**

⁸ By determining the dynamics of the most elementary degrees of freedom, par-
⁹ ticle physics hopes to uncover the fundamental laws of the universe. The definition
¹⁰ of elementary has evolved through time and currently refers to matter and force
¹¹ mediating particles: fermions and bosons, respectively. The Standard Model of
¹² Particle Physics (SM) describes the quantum behavior of three of the four funda-
¹³ mental forces: weak, strong, and electromagnetic, via boson and fermion interac-
¹⁴ tions. Gravity is not included in the SM and still under investigation.

¹⁵ **1.2 Quantum Field Theory**

¹⁶ In the SM, forces (and particles) are represented as fields. In this context,
¹⁷ fields are mathematical objects that define a tensor (e.g. scalar, vector, etc) at
¹⁸ every point on a manifold, here the manifold is space-time. These fields obey laws

¹⁹ dictated by Quantum Field Theory (QFT). Particles arise naturally in QFT as
²⁰ quantized field excitations localized in spacetime.

²¹ According to Noether's theorem, symmetries of a field give rise to conserved
²² quantities (e.g. time-translation invariance leads to energy conservation). Often
²³ in the history of physics, a conserved quantity of a field is found and then the
²⁴ underlying symmetry of the field is inferred. Gauge symmetries are symmetries
²⁵ among the internal degrees of freedom of the field (components of the tensor),
²⁶ which give rise to quantities associated with fields. By specifying the symmetries
²⁷ of a system the dynamics and conserved quantities of the system may be succinctly
²⁸ defined.

²⁹ 1.3 $U(1)_{EM}$ Local Gauge Invariance

³⁰ The Lagrangian of Quantum Electrodynamics (QED) describes the electro-
³¹ magnetic force. QED may be derived by requiring local $U(1)_{EM}$ gauge invariance
³² of the free dirac fermion Lagrangian, ψ :

$$\mathcal{L} = i\bar{\psi}\gamma^\mu\partial_\mu\psi - m\bar{\psi}\psi \quad (1.1)$$

³³ This symmetry may be represented as a complex number with unit modulus,
³⁴ $e^{i\theta}$. $U(1)$ gauge invariance requires this gauge transformation of ψ will leave the
³⁵ Lagrangian unchanged.

$$\psi(x) \rightarrow \psi'(x) = e^{i\theta(x)}\psi(x) \quad (1.2)$$

³⁶ NB: This transformation is a local gauge transformation as θ depends on the
³⁷ spacetime coordinate.

³⁸ By requiring this symmetry of the free Dirac fermion Lagrangian:

$$\mathcal{L} = i\bar{\psi}\gamma^\mu\partial_\mu\psi - m\bar{\psi}\psi \quad (1.3)$$

³⁹ The mass term is unaffected, but the kinetic term is modified due to $\theta(x)$.

$$\mathcal{L} \rightarrow \mathcal{L}' = i\bar{\psi}e^{-i\theta(x)}\gamma^\mu\partial_\mu\psi e^{i\theta(x)} - m\bar{\psi}e^{-i\theta(x)}\psi e^{i\theta(x)} \quad (1.4)$$

⁴⁰

$$= i\psi\gamma^\mu(\partial_\mu\psi + i\psi\partial_\mu\theta) - m\bar{\psi}\psi \quad (1.5)$$

⁴¹ The $\partial_\mu\theta$ terms breaks the gauge invariance of the Lagrangian. By introducing a
⁴² new field, A_μ we can recover the gauge invariance of the derivative. Now redefining
⁴³ the derivative as the covariant derivative:

$$D_\mu\psi \equiv (\partial_\mu - iqA_\mu)\psi \quad (1.6)$$

⁴⁴ And letting A_μ transform under $U(1)$ as:

$$A_\mu \rightarrow A_\mu + \delta A_\mu \quad (1.7)$$

⁴⁵ The transformed covariant derivative becomes:

$$D_\mu\psi \rightarrow D_\mu\psi' = (\partial_\mu - iqA_\mu)\psi' \quad (1.8)$$

⁴⁶

$$= (\partial_\mu - iq(A_\mu + \delta A_\mu))\psi e^{i\theta} \quad (1.9)$$

⁴⁷

$$= e^{i\theta}D_\mu + ie^{i\theta}\psi(\partial_\mu\theta - q\delta A_\mu) \quad (1.10)$$

⁴⁸ The covariant derivative can be made gauage invariant by setting the last term
⁴⁹ to zero.

$$\delta A_\mu = \frac{1}{q} \partial_\mu \theta \quad (1.11)$$

50 So now A_μ transforms as:

$$A_\mu \rightarrow A_\mu + \frac{1}{q} \partial_\mu \theta \quad (1.12)$$

51 Finally, replacing the derivative with the covariant derivative the Dirac La-
52 grangian we have:

$$\mathcal{L} = i\bar{\psi}\gamma^\mu D_\mu \psi - m\bar{\psi}\psi - \frac{1}{4}F_{\mu\nu}F^{\mu\nu} \quad (1.13)$$

53

$$= \mathcal{L}_{QED} \quad (1.14)$$

54 Here $F_{\mu\nu} \equiv \partial_\mu A_\nu - \partial_\nu A_\mu$. This last term in the Lagrangian is the kinetic
55 energy of the gauge boson field.

56 So we have derived the QED Lagrangian. By requiring the free Dirac La-
57 grangian to be invariant under U(1) transformations we have generated a new
58 gauge boson field, A_μ , which describes the photon. As expected the photon inter-
59 acts with fermions.

60 Stepping back, a global U(1) gauge symmetry of the free Dirac Lagrangian
61 implies we cannot measure the absolute phase of a charged particle. A local U(1)
62 gauge symmetry changes the phase of fields differently across space time. For this
63 type of transformation to leave the Lagrangian invariant, we had to introduce an
64 additional field, A_μ , which "communicates" these phase changes across space-time.
65 In less formal language this effectively means: if the field at one location changes,
66 this change is conferred to other particles via A_μ .

67 1.4 Yang-Mills Gauge Theories

68 Requiring $U(1)_{EM}$ gauge invariance of the free Dirac Lagrangian gave us QED.

69 Requiring different gauge symmetries we can derive the structure of other inter-
70 actions. Any gauge symmetry may be written as:

$$\psi_i \rightarrow \exp(i\theta^a T_{ij}^a) \psi_j \quad (1.15)$$

71 Here θ is a dimensionless real parameter and T is the generator of the gauge
72 symmetry group. With this the covariant derivative can be written as:

$$D_\mu \psi_i \equiv \partial_\mu \psi_i + ig A_\mu^a T_{ij}^a \psi_j \quad (1.16)$$

73 Then the gauge field must transform as:

$$A_\mu^a \rightarrow A_\mu^a - \frac{1}{g} \partial_\mu \theta^a - f^{abc} \theta^b A_\mu^c \quad (1.17)$$

74 Here f is the structure constant of the gauge group. The field strength tensor
75 is given by:

$$F_{\mu\nu}^a \equiv \partial_\mu A_\nu^a - \partial_\nu A_\mu^a - g f^{abc} A_\mu^b A_\nu^c \quad (1.18)$$

76

$$F_{\mu\nu}^a \rightarrow F_{\mu\nu}^a - f^{abc} \theta^b F_{\mu\nu}^c \quad (1.19)$$

77 This gives the Yang-Mills Lagrangian:

$$\mathcal{L}_{YM} = -\frac{1}{4} F_{\mu\nu}^a F_{\mu\nu}^a + i \bar{\psi}_i \gamma^\mu D_\mu \psi_i + m \bar{\psi}_i \psi_i \quad (1.20)$$

78 1.5 Particles in the Standard Model

79 The SM consists of fermions (half-integer spin matter constituents) and bosons
80 (integer spin force mediators). Fermions are spinor representations of the Poincare
81 group and can be further separated into leptons and quarks. Bosons are the result
82 of requiring a particular symmetry among the spinor fields:

$$SU(3)_C \times SU(2)_L \times U(1)_Y \quad (1.21)$$

83 $SU(3)_C$ is the symmetry group of the strong force and generates eight gluon
84 fields, G_μ . $SU(2)_L$ is the symmetry group of the Electroweak force and generates
85 three electroweak boson fields. The mixing of this $SU(2)_L$ and $U(1)_Y$ gives rise
86 to the photon field, where Y is the weak-hypercharge:

$$Y = 2(Q - T_3) \quad (1.22)$$

87 Q is the electromagnetic charge, and T_3 is the z-component of the weak isospin.
88 Weak isospin is the charge associated with the $SU(2)_L$ symmetry. The correspond-
89 ing covariant derivative is then:

$$D_\mu \phi \equiv (\partial_\mu + ig_1 B_\mu Y_{L/R} + [ig_2 W_\mu^\alpha T^\alpha]_L + [ig_3 G_\mu^\alpha \tau^\alpha]_C) \psi \quad (1.23)$$

90 It is important to note that the gauge symmetry of the SM yields a particular
91 structure of the fermion representations. So for a given fermion to interact with
92 a given gauge field it must have a non-zero corresponding Noether charge for
93 that gauge symmetry. If the corresponding Noether charge is zero, that fermion
94 transforms as a singlet and does not participate in that gauge interaction.

95 Fermions are divided into quarks and leptons based on their transformations
96 under $SU(3)_C$. Quarks transform as color triplets. Leptons transform as color

singlets and consequently do not interact with gluons. Fermions may be further
 classified by their $SU(2)_L$ interactions. Only the left-chiral part of fermions (denoted by L here) transform as $SU(2)_L$ doublets, the right-chiral part forms singlets under this gauge. Lastly, all these groups of particles come in three generations, each a heavier copy of the previous, but with differing flavor quantum numbers.
 This is summarized in Table 1.1 and shown in Figures 1.1 and 1.2.

SM Fermion Gauge Group	First Generation	Second Generation	Third Generation	$(SU(3)_C, SU(2)_L, U(1)_Y)$ Representations
Left-handed quarks	$\begin{pmatrix} u_L^r & u_L^g & u_L^b \\ d_L^r & d_L^g & d_L^b \end{pmatrix}$	$\begin{pmatrix} c_L^r & c_L^g & c_L^b \\ s_L^r & s_L^g & s_L^b \end{pmatrix}$	$\begin{pmatrix} t_L^r & t_L^g & t_L^b \\ b_L^r & b_L^g & b_L^b \end{pmatrix}$	$(3, 2, \frac{1}{6})$
Right-handed quarks	(u_R^r, u_R^g, u_R^b) (d_R^r, d_R^g, d_R^b)	(c_R^r, c_R^g, c_R^b) (s_R^r, s_R^g, s_R^b)	(t_R^r, t_R^g, t_R^b) (b_R^r, b_R^g, b_R^b)	$(3, 1, \frac{2}{3})$ $(3, 1, -\frac{1}{3})$
Left-handed leptons	$\begin{pmatrix} \nu_e^L \\ e_L \end{pmatrix}$	$\begin{pmatrix} \mu_e^L \\ \mu_L \end{pmatrix}$	$\begin{pmatrix} \tau_e^L \\ \tau_L \end{pmatrix}$	$(1, 2, -\frac{1}{2})$
Right-handed leptons	e_R	μ_R	τ_R	$(1, 1, -1)$

Table 1.1: Representations of the SM fermions under $SU(3)_C \times SU(2)_L \times U(1)_Y$ gauge symmetry group. $SU(2)_L$ gauge transformations allow one to go between rows and $SU(3)_C$ transformations allow one to go between columns in these fermion representations. [REWORD]

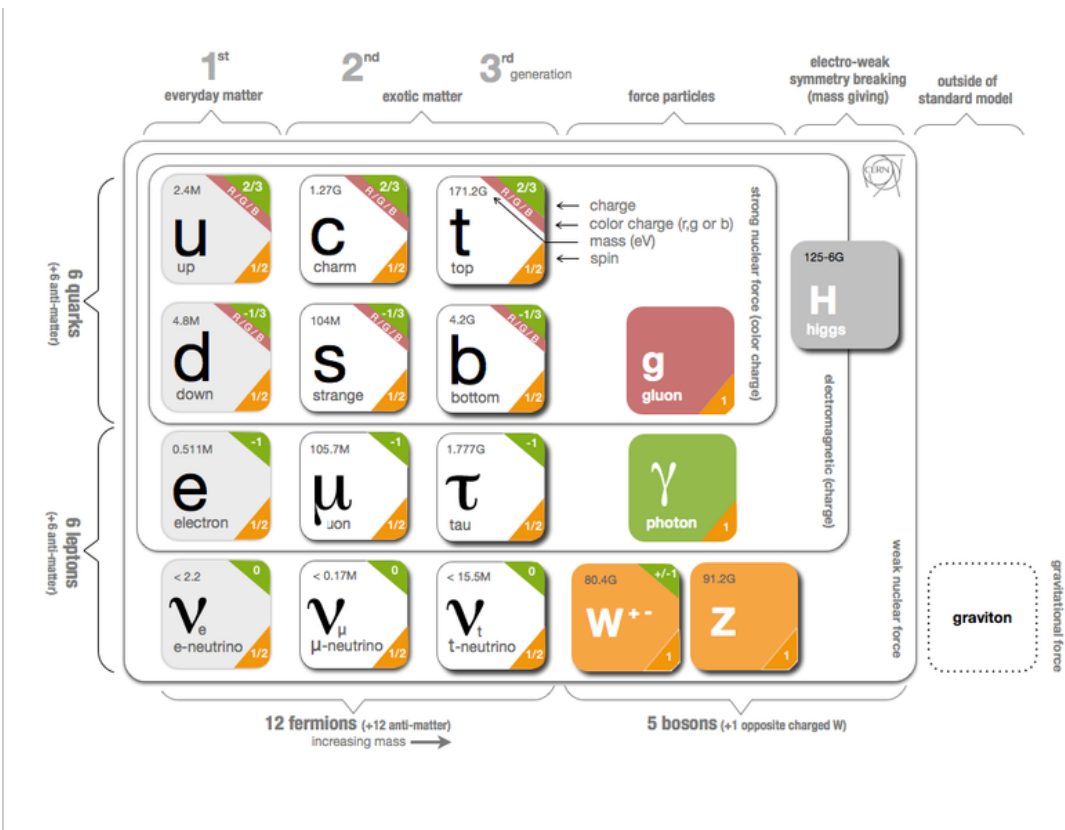


Figure 1.1: The particles of the Standard Model.

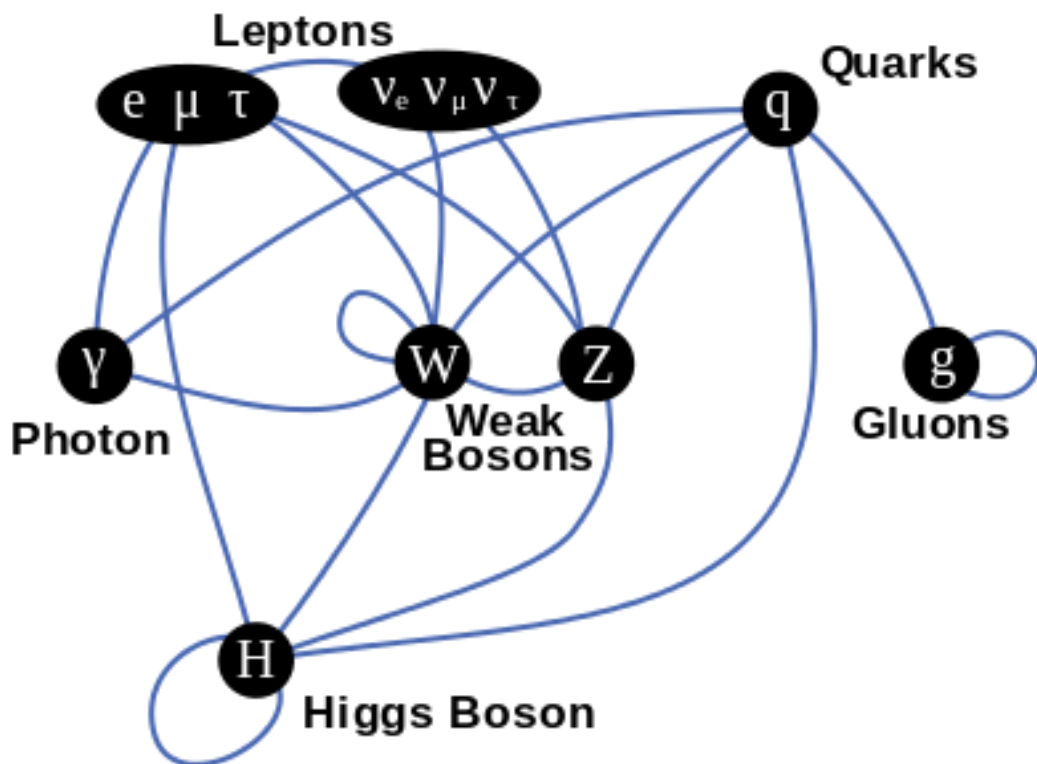


Figure 1.2: Summary of how Standard Model particles interact with other Standard Model particles.

¹⁰³ Now we can understand the SM Lagrangian density as a Yang-Mills theory
¹⁰⁴ with the gauge group: $SU(3)_C \times SU(2)_L \times U(1)_Y$ with an additional $SU(2)$ complex
¹⁰⁵ scalar Higgs field doublet that will be discussed later.

$$\begin{aligned} \mathcal{L}_{SM} = & \underbrace{-\frac{1}{4}B_{\mu\nu}B^{\mu\nu} - \frac{1}{4}W_{\mu\nu}^aW^{a\mu\nu} - \frac{1}{4}G_{\mu\nu}^\alpha G^{\alpha\mu\nu}}_{\text{Kinetic Energies and Self-Interactions of Gauge Bosons}} \\ & + \underbrace{\bar{L}_i \gamma^\mu (i\partial_\mu - \frac{1}{2}g_1 Y_{iL} B_\mu - \frac{1}{2}g_2 \sigma^a W_\mu^a) L_i}_{\text{Kinetic Energies and EW Interactions of Left-handed Fermions}} \\ & + \underbrace{\bar{R}_i \gamma^\mu (i\partial_\mu - \frac{1}{2}g_1 Y_{iR} B_\mu) R_i}_{\text{Kinetic Energies and EW Interactions of Right-Handed Fermions}} \\ & + \underbrace{\frac{ig_3}{2} \bar{Q}_j \gamma^\mu \lambda^\alpha G_\mu^\alpha Q_j}_{\text{Strong Interactions between Quarks and Gluons}} \\ & + \underbrace{\frac{1}{2} |(i\partial_\mu - \frac{1}{2}g_1 B_\mu - \frac{1}{2}g_2 \sigma^a W_\mu^a)\Phi|^2 - V(\Phi)}_{\text{Electroweak Boson Masses and Higgs Couplings}} \\ & - (\underbrace{y_{kl}^d \bar{L}_k \Phi R_l + y_{kl}^u \bar{R}_k \tilde{\Phi} L_l}_{\text{Fermion Mass terms and Higgs Couplings}} + h.c.) \end{aligned}$$

¹⁰⁶ Here several abstract spaces are being spanned:

- ¹⁰⁷ – a spans the three $SU(2)_L$ gauge fields with generators expanded in Pauli
¹⁰⁸ matrices, $T^\alpha = \frac{1}{2}\sigma^\alpha$
- ¹⁰⁹ – α spans the eight $SU(3)_C$ gauge fields, with generators expanded in Gell-
¹¹⁰ Mann matrices, $\tau^\alpha = \frac{1}{2}\lambda^\alpha$
- ¹¹¹ – L/R represent left and right projections of Dirac fermion fields. The Strong
¹¹² interaction is not chiral, so $Q = L+R$

113 – μ and ν are four-vector indices

114 – i, j, k are summed over the three generations of SM particles.

115 1.6 Higgs Mechanism

116 The SM Lagrangian without the addition of a Higgs field does not allow for
117 gauge boson and fermion mass terms: $\frac{1}{2}m_A^2 A_\mu A_\mu$ and $m(\bar{\psi}\psi)$, as these terms are
118 not gauge invariant. By introducing the Higgs field, mass terms for these particles
119 may be included in a gauge invariant way. This field is a complex doublet with a
120 potential $V(\Phi)$:

$$\Psi = \begin{pmatrix} \Phi^\dagger \\ \Phi^0 \end{pmatrix} \quad (1.24)$$

121 $V(\Phi) = \mu^2 \Phi^\dagger \Phi + \lambda |\Phi^\dagger \Phi|^2 \quad (1.25)$

122 The minima of this field occurs for $|\Phi| = \sqrt{\frac{\mu^2}{2\lambda}} \equiv \frac{v}{2}$. This yields degenerate
123 minima, this symmetry is broken by choosing a specific minima (a.k.a. sponta-
124 neous symmetry breaking). By convention $\Phi_{min} = \frac{1}{\sqrt{2}} \begin{pmatrix} 0 \\ v \end{pmatrix}$ is chosen. This means
125 the ground state of the Higgs field (Higgs vacuum) is non-zero, $\sqrt{\frac{-\mu^2}{\lambda}}$. The Higgs
126 Field may now be expanded around this new ground state:

$$\Phi(x) = \frac{1}{\sqrt{2}} \begin{pmatrix} 0 \\ v + h(x) \end{pmatrix} \quad (1.26)$$

127 This non-zero Higgs vacuum now generates mass terms for the gauge bosons
128 from the following term in the Lagrangian:

$$|(-\frac{1}{2}g_1B_\mu - \frac{1}{2}g_2\sigma^aW_\mu^a)\Phi|^2 = \frac{1}{2}m_W^2W_\mu^+W^{-\mu} + \frac{1}{2}m_Z^2Z_\mu Z^\mu \quad (1.27)$$

129 where:

$$W_\mu^\pm \equiv \frac{1}{\sqrt{2}}(W_\mu^1 \mp iW_\mu^2) \quad (1.28)$$

$$\begin{aligned} \text{130} \quad Z_\mu &\equiv \frac{1}{\sqrt{g_1^2 + g_2^2}}(g_2W_\mu^2 - g_1B_\mu) \end{aligned} \quad (1.29)$$

$$\begin{aligned} \text{131} \quad m_W &= \frac{vg_2}{\sqrt{2}} \end{aligned} \quad (1.30)$$

$$\begin{aligned} \text{132} \quad m_Z &= \frac{v}{\sqrt{2}}\sqrt{g_1^2 + g_2^2} \end{aligned} \quad (1.31)$$

133 The Higgs field also generates a mass term for the Higgs boson and self-
134 interactions for the Higgs boson.

135 1.7 Electroweak Theory

136 $SU(2)_L$ generates W^\pm, W^0 gauge bosons, which would be massless if $SU(2)_L$
137 was a perfect symmetry. These bosons are massive as this symmetry is broken.

138 The mass eigenstates, Z and γ given by:

$$\begin{pmatrix} Z_\mu \\ A_\mu \end{pmatrix} = \begin{pmatrix} \cos\theta_W & -\sin\theta_W \\ \sin\theta_W & \cos\theta_W \end{pmatrix} \begin{pmatrix} W_\mu^3 \\ B_\mu \end{pmatrix} \quad (1.32)$$

139 Here θ_W is the Weinberg angle given by:

$$\cos\theta_W = \frac{g_2}{\sqrt{g_1^2 + g_2^2}} = \frac{m_W}{m_Z} \quad (1.33)$$

¹⁴⁰ 1.8 Quantum ChromoDynamics

¹⁴¹ As mentioned earlier the Strong Force, which binds the proton together, is
¹⁴² mediated by gluons. Quantum Chromodynamics is the QFT which describes the
¹⁴³ interactions of quarks and gluons via $SU(3)_C$ symmetry. QCD contains features
¹⁴⁴ not present in Electroweak Interactions due to $SU(3)_C$ generators not commuting
¹⁴⁵ (a.k.a. $SU(3)_C$ is a non-abelian group). For example, in QCD there is color
¹⁴⁶ confinement and asymptotic freedom due to the structure constants being non-
¹⁴⁷ zero. Requiring $SU(3)_C$ local gauge invariance implies:

$$\psi(x) \rightarrow \psi(x)' = \exp[i g_S \alpha(x) \cdot \hat{T}] \psi(x) \quad (1.34)$$

¹⁴⁸ where $\alpha(x)$ is the local phase function, g_S is the strong coupling constant, and
¹⁴⁹ \hat{T} are the eight generators of $SU(3)$ (note $\hat{T}^a = \frac{1}{2}\lambda^a a$, where λ^a are the Gell-Mann
¹⁵⁰ matrices). As the Gell-Mann matrices are 3x3, this means ψ has three degrees of
¹⁵¹ freedom under these $SU(3)$ rotations. So we represent ψ under $SU(3)$ rotations
¹⁵² as:

$$\psi = \begin{pmatrix} \psi_{red} \\ \psi_{green} \\ \psi_{blue} \end{pmatrix} \quad (1.35)$$

¹⁵³ Consequently, particle fields transforming under $SU(3)$ rotations have three
¹⁵⁴ components which physicists describe as color components (red, green, and blue).
¹⁵⁵ A particle's corresponding antiparticle has the corresponding anticolor. This color
¹⁵⁶ is the "charge" of QCD and is conserved under $SU(3)$ rotations. Combining colors,
¹⁵⁷ color neutral states (e.g. red and antired, or red, green and blue) may be created.
¹⁵⁸ For the Free Dirac Lagrangian to remain invariant under $SU(3)$ transformations,
¹⁵⁹ we must again postulate a boson field that modifies the derivative. The gluon

₁₆₀ field tensor is given by ($\alpha = 1, \dots, 8$):

$$G_{\mu\nu}^k = \partial^\mu G_\alpha^\nu - \partial^\nu G_\alpha^\mu - g_S f^{\alpha\beta\gamma} G_\beta^\mu G_\gamma^\nu \quad (1.36)$$

₁₆₁ Here $f^{\alpha\beta\gamma}$ are the structure constants of $SU(3)$. Combining all this gives the
₁₆₂ QCD Lagrangian:

$$\mathcal{L}_{QCD} = \bar{\psi}_q i\gamma^\mu (D_\mu)_{ij} \psi^{qj} - m \bar{\psi}^{qi} \psi_{qi} - \frac{1}{4} G_{\mu\nu}^\alpha G^{\alpha\mu\nu} \quad (1.37)$$

₁₆₃ Here i are the color indices, and q are the quark flavors. It is important to
₁₆₄ note that quarks transform under the fundamental representation of $SU(3)$, while
₁₆₅ gluons transform under the adjoint representation. This means quarks carry a
₁₆₆ single color charge (red, green, blue, antired, antigreen, antiblue) and gluons carry
₁₆₇ a color and anticolor charge.

₁₆₈ Figure 1.3 shows the three dominant QCD interactions. Since gluons carry
₁₆₉ color charge, they interact with one another. This does not occur in QED, as
₁₇₀ photons do not have electric charge and therefore do not interact with each other.
₁₇₁ In QED, a bare electron's effective charge is largest closest to the electron and
₁₇₂ decreases as a function of distance. This is because the QED vacuum fills with
₁₇₃ particle antiparticle pairs spontaneously, which screen the charge of the bare elec-
₁₇₄ tron. The larger the distance from the electron, the smaller the effective charge
₁₇₅ and therefore the weaker the force. So for a pair of electrons, as the distance
₁₇₆ between them increases the repulsive force decreases and they may be observed
₁₇₇ separately.

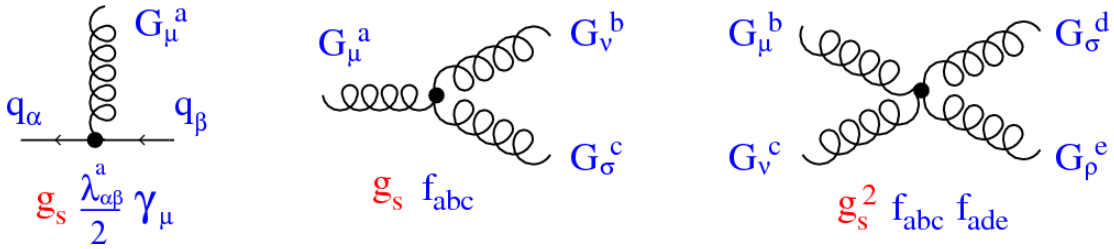


Figure 1.3: This figure shows the three dominant QCD interactions. From Ref. [14]

178 As the distance from a quark increases it's effective color charge increases due
 179 to the vacuum polarization in QCD. Color charge grows as the distance from
 180 the source increases (a.k.a. color is anti-screened in QCD). In this way, strong
 181 interactions become stronger at large distances (low momenta interactions). At
 182 small distances (large momenta interactions) strong interactions are significantly
 183 weaker and considered nearly free. This effect of referred to as asymptotic freedom.
 184 At large distances, a quark's effective charge is large and the strong force is more
 185 significant. This force becomes so strong that quarks form colorless bound states
 186 instead of remaining free particles. This effect is known as color confinement.
 187 This running of all SM fields is shown in Figure 1.4.

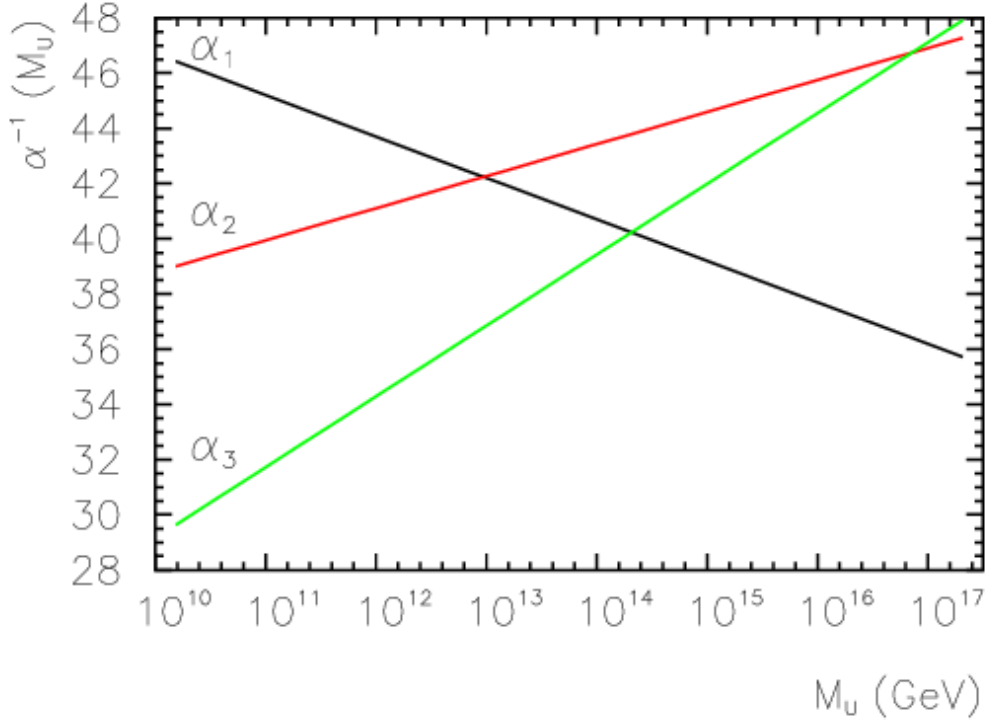


Figure 1.4: Strength of the U(1), SU(2), and SU(3) gauge couplings as a function of the energy scale of the interaction (Q). From Ref. [10]

Commonly the change in a particle's effective charge under a given force is quantified with $\beta(r) \equiv -\frac{de(r)}{d\ln r}$, where $e(r)$ is the effective charge of a given particle under a force. In QED this function is positive but in QCD this function is negative leading to confinement and asymptotic freedom. Moreover, one can calculate how the coupling (α) of a force varies with energies. (More deeply this amounts to incorporating renormalization and vacuum polarization in the boson propagators).

For QCD this is:

$$\alpha_s(x) = \frac{\alpha_s(\mu^2)}{1 + \beta_0 \alpha_s(\mu^2) \ln(Q^2/\mu^2)} \quad (1.38)$$

195

$$\beta_0 = \frac{11N_c - 2n_f}{12\pi} \quad (1.39)$$

196 where Q is the momentum of the the force is probed at, μ^2 is the renormalization scale.

198 As stated previously, quarks and gluons have not been observed in isolation.
 199 Instead they form bound colorless states. Hadronization is the process by which
 200 quarks and gluons form hadrons. The process of hadronization is still an active
 201 area of research. One qualitative description is show in Figure [Natasha add
 202 figure]. In this figure, as two quarks separate the color field between them is
 203 restricted to a tube with energy density of 1GeV/fm. As they separate further,
 204 the energy in the color field increases, until there is enough energy to produce
 205 $q\bar{q}$ pairs, which breaks the color field. This process repeats until quarks and
 206 antiquarks have low enough energy to form colorless hadrons. The resulting spray
 207 of hadrons is called a jet.

208 Since quarks and gluons carry different color charges, their respective jets have
 209 different properties. As quarks carry only a single color charge (vs. gluons which
 210 have color and anticolor charge), so their jets have less constituent particles. More
 211 precisely, the Altarelli-Parisi splitting functions [3] contain a factor C_A for gluon
 212 radiation off a gluon and C_F for gluon radiation off a quark ($C_A/C_F = 9/4$). These
 213 color factors are the prefactor in the Feynman diagrams for these processes [1],
 214 which leads to gluon jets having more constituents and therefore more tracks than
 215 quark jets. Gluon jets also tend to have a larger radius with lower momentum
 216 constituents than quarks. There are many novel techniques to distinguish quarks
 217 from gluons. For this study the number of charged particles will be focused on.

²¹⁸ **Chapter 2**

²¹⁹ **Standard Model Successes and
Limitations**

²²¹ The Standard Model has consistently described much of reality to an extreme
²²² degree of accuracy. It has predicted cross sections for strong and electroweak pro-
²²³ cesses that span over ten order of magnitude correctly [see Fig 2.1] and contains
²²⁴ no known logical inconsistencies. Despite the strength and reality of the Stan-
²²⁵ dard Model, it still fails to describe aspects of reality and suffers from aesthetic
²²⁶ issues. To date, dark matter and energy comprise 95% of the universe, but are
²²⁷ not accounted for in the SM. Additionally, neutrinos are known to have mass but
²²⁸ are massless in the SM. There are mechanisms for introducing massive neutrinos
²²⁹ in the SM, but these mechanisms create hierarchy problems.

²³⁰ Possibly the most significant aesthetic issue is the hierarchy between the elec-
²³¹ troweak and Planck scales. The electroweak scale is the scale of electroweak
²³² symmetry breaking. The Planck scale is the scale where the gravitational force
²³³ is comparable in strength to the other forces. The Planck scale is where the SM
²³⁴ breaks down, as there is not an experimentally verified theory of quantum gravity,
²³⁵ and at this scale gravity cannot be ignored (like it can at the electro-weak scale).

²³⁶ These scales differ by ~ 30 orders of magnitude. Understanding the difference
²³⁷ in these energy scales, may help explain the weakness of gravity at electroweak
²³⁸ scales, and possibly a QFT for gravity. (NB: This hierarchy can also be framed in
²³⁹ terms of the corrections to the Higgs mass, which depend on the UV cutoff scale -
²⁴⁰ where the SM is suppose to break, which is taken at the Planck scale. This leads
²⁴¹ the quantum corrections to the Higgs mass to force the Higgs mass to 10^{18} TeV.)

²⁴² These stark contrasts in scales may indicate that a more fundamental theory
²⁴³ exists. It is hoped that such a theory would explain and motivate some of the ad-
²⁴⁴ hoc features of the SM. In particular, there currently are no experimentally verified
²⁴⁵ explanations of why there are three generations of fermions, the values of the 19
²⁴⁶ SM parameters (6 quark masses, 3 charged lepton masses, 3 gauge couplings,
²⁴⁷ Higgs parameters (μ^2, λ)), the structure of the fermion representations, etc.

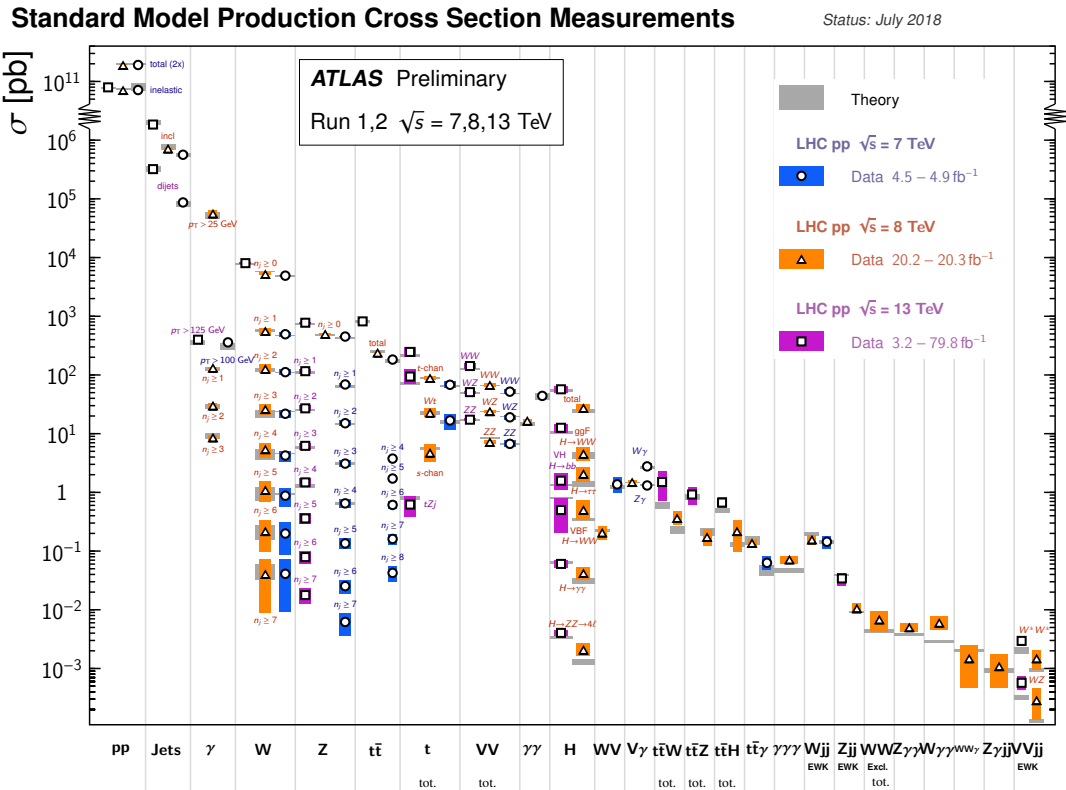


Figure 2.1: A comparison of cross section measurements at $\sqrt{s} = 7,8,13$ TeV from ATLAS compared to theoretical measurements. From Ref. [5]

²⁴⁸ **Chapter 3**

²⁴⁹ **New Physics Models with**

²⁵⁰ **Diboson Resonances**

²⁵¹ **3.1 Randall Sundrum Bulk Model**

²⁵² The electroweak-planck hierarchy may be explained by the existence of extra
²⁵³ dimensions, like the 5D Randall Sundrum Bulk Model ([15], [2]). In this model,
²⁵⁴ there is one extra warped spatial dimension, y , with a metric:

$$ds^2 = e^{-2k|y|} \eta_{\mu\nu} dx^\mu dx^\nu + dy^2 \quad (3.1)$$

²⁵⁵ where $e^{-k|y|}$ is the warp factor of the extra dimension, which is compactified on
²⁵⁶ a S^1/Z_2 orbifold (a.k.a. a circle where $y \rightarrow -y$). This can be visualized as every
²⁵⁷ point in space time having a line extending from it a distance L , representing
²⁵⁸ this fifth dimension. At the end of this line is the Planck brane. This fourth
²⁵⁹ spatial dimension separates two 4-D branes: Planck brane and TeV brane. We
²⁶⁰ live on the TeV brane, as shown in Figure 3.1. The Higgs field (and to a lesser
²⁶¹ degree the top quark and graviton fields) is localized near the TeV Brane, while

262 the light fermion fields are localized more near the Planck brane. Fundamental
 263 parameters are set on the Planck brane. The warp factor may be scaled away from
 264 all dimensionless SM terms by field redefinitions. However, the only dimensionful
 265 parameter, $m_H^2 = v^2$ is rescaled by $\tilde{v} \sim e^{-kL} M_{Pl} \sim 1\text{TeV}$ for $kL \sim 35$, explaining
 266 why gravity is so weak on the TeV brane. Also, by localizing the light fermion
 267 fields near the Planck brane and top and graviton fields near the TeV brane, the
 268 light quarks will have smaller masses.

269 The two free parameters of this theory are M_{Pl} and k . Based on this RS Bulk
 270 model, all SM particles should have Kaluza-Klein (KK) excitations. In particular,
 271 the graviton would have KK excitations that prefer to decay to WW or ZZ, which
 272 is why this analysis searches for RS Gravitons.

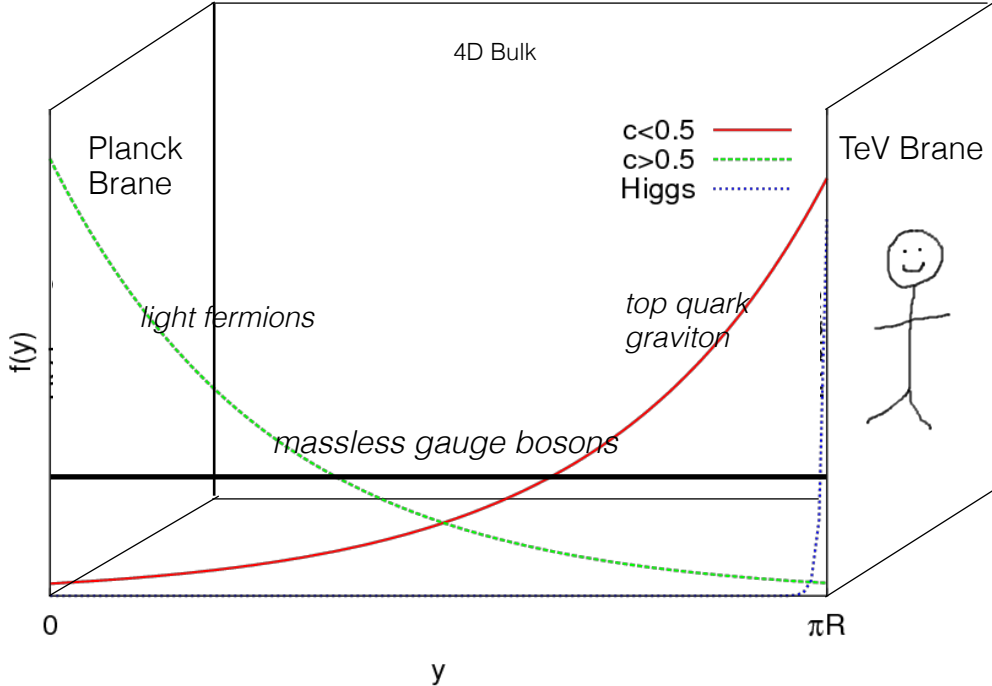


Figure 3.1: Cartoon of RS Bulk Model

²⁷³ 3.2 Extended Scalar Sector

²⁷⁴ A further striking asymmetry of the SM is the simplicity of the scalar sector in
²⁷⁵ comparison to the boson and fermion sectors. To date, the scalar sector has only
²⁷⁶ one member, the Higgs boson. Therefore, it is natural to posit an extension to the
²⁷⁷ scalar sector. From a theoretical standpoint this could also help generate baryon
²⁷⁸ asymmetry through additional sources of CP violation. This analysis searches for
²⁷⁹ a simple extension to the scalar sector as proposed in Ref. [16]. The extended
²⁸⁰ scalar sector includes a real Higgs singlet (S) and complex $SU(2)_L$ doublet (Φ)
²⁸¹ (the SM Higgs), where mass eigenstates are mixtures of the fields. S has a vev of
²⁸² v and Φ has a vev of x . This then gives a Lagrangian of:

$$\mathcal{L} \supset (D^\mu \Phi)^\dagger D_\mu \Phi + \partial^\mu S \partial_\mu S - m^2 \Phi^\dagger \Phi - \mu^2 S^2 + \lambda_1 (\Phi^\dagger \Phi)^2 + \lambda_2 S^4 + \lambda_3 \Phi^\dagger \Phi S^2 \quad (3.2)$$

²⁸³ The mass eigenstates of the scalar sector are then mixtures of S and Φ and
²⁸⁴ the free parameters of the theory are m_H , $\sin \alpha$, and $\tan \beta = v/x$. The fields are
²⁸⁵ then given by:

$$\Phi \equiv \begin{pmatrix} 0 \\ \frac{\tilde{h}+v}{\sqrt{2}} \end{pmatrix} \quad (3.3)$$

²⁸⁶

$$S \equiv \frac{h' + x}{\sqrt{2}} \quad (3.4)$$

²⁸⁷ Diagonalizing the mass matrix leads to the mass eigenstates h (discovered
²⁸⁸ Higgs boson) and H (the physical particles):

$$\begin{pmatrix} h \\ H \end{pmatrix} = \begin{pmatrix} \cos \alpha & -\sin \alpha \\ \sin \alpha & \cos \alpha \end{pmatrix} \quad (3.5)$$

289 This suppressed h and H production and SM H couplings:

$$BR_{H \rightarrow SM} = \sin^2 \alpha \times \frac{\Gamma_{SM, H \rightarrow SM}}{\Gamma_{tot}} \quad (3.6)$$

290 Moreover, in the case that $m_H > m_h$, $H \rightarrow hh$ is possible. This further suppresses
291 $H \rightarrow VV/ff$. This search is most sensitive to $H \rightarrow WW$.

292 3.3 Simple Standard Model Extensions

293 The RS Bulk model is motivated by resolving the hierarchy problem. Extending the Scalar sector is a natural space to look for new physics due to the complexity of fermion and boson groups. There are many other interesting and well motivated frameworks, but there is a lack of completely predictive models, due to model flexibility (free parameters). Therefore it is hard for experimentalists to know which theories to search for in data. However, as seen in [13], a "Simplified Model" approach may be taken. In the search for reasonably narrow width particles, as in this search, the search is not sensitive to all the details and free parameters of the theory. Generally such searches are only sensitive to the resonance mass and its interactions. Therefore, a theory's Lagrangian may be reduced to only retain this information (mass parameters and couplings). Experimental results using this framework may then be reinterpreted in a given theory.

305 In the simplified approach, the new resonance searched for is represented as a real vector field in the adjoint representation of $SU(2)_L$ with vanishing hypercharge. This results in one neutral and two charged bosons. Defined as:

$$V^\pm = \frac{V_\mu^1 \mp iV_\mu^2}{\sqrt{2}} \quad (3.7)$$

308 $V_\mu^0 = V_\mu^3 \quad (3.8)$

309 The SM Lagrangian is then augmented with the additional terms:

$$\mathcal{L} \supset -\frac{1}{4}D_{[\mu}V_{\nu]}^a D^{[\mu}V^{\nu]}_a + \frac{m_V^2}{2}V_\mu^a V^{a\mu} + ig_V c_H V_\mu^a H^\dagger \tau^a \overset{\leftrightarrow}{D}^\mu H + \frac{g^2}{g_V} c_F V_\mu^a J_F^{\mu a} \quad (3.9)$$

310 In order the terms represent: the kinetic, V mass, Higgs- V interaction, and
311 V -left-handed fermion interaction terms. Phenomenologically the three physical
312 particles this predicts are degenerate, where V couples most strongly to VV , via
313 the g_V coupling factor. The dominant production modes are DY and VBF.

314 Two versions of HVT are considered, Model A and B. Model A is a weakly
315 coupled model where $g_V \sim 1$, like the extended gauge symmetry discussed in Ref
316 . [16]. Model B is a strongly coupled model, where $1 < g_V < 4\pi$. The width
317 of the resonance grows with g_V so for this narrow resonance search only g_V is
318 chosen to be less than 6 (so $\Gamma/M < 10\%$). More precisely, the coupling of these
319 resonances to fermions scales as $g_f = g^2 c_F/g_V$, where g is the SM $SU(2)_L$ gauge
320 coupling and c_F is the free parameter (expected to be of order 1 for Model A and
321 B). This then means that for Model B the coupling to fermions is more suppressed
322 than for Model A, leading to a smaller DY production rate and BR to fermionic
323 final states. The coupling of V to SM bosons scales as $g_H = g_V c_H$, where c_H is
324 a free parameter on the order of 1 for Model A and B. So for small values of g_V
325 (i.e. Model A - weakly coupled theories) the BR to gauge bosons is smaller than
326 for Model B. So weakly coupled vectors have large production cross sections and
327 decay prominently to leptons or jets, while strongly coupled vectors are produced
328 less and decay predominantly to gauge bosons.

329 Vectors in Model A and B are generally produced via quark-anti-quark annihi-
330 lation. The more rare production via vector-boson-fusion is considered by setting
331 $g_H = 1$ and $g_F = 0$. In Model B diboson final states are enhanced as stated
332 previously due to g_H and moreover the BR to WZ , WH , WW , and ZH are the

³³³ same.

³³⁴ In summary, V couples most strongly to left-handed fermions and VV dependent on g_V .

336

Part II

337

Experimental Setup

³³⁸ **Chapter 4**

³³⁹ **LHC**

³⁴⁰ The Large Hadron Collider (LHC) is the highest-energy particle collider in the
³⁴¹ world. It was designed to expand the frontier of high energy particle collisions in
³⁴² energy and luminosity. This enables LHC experiments to test the Standard Model
³⁴³ and search for new physics at higher energies than tested with previous colliders.
³⁴⁴ Collisions at higher energies not only produce more massive particles but also
³⁴⁵ more weakly interacting particles. Fig. 4.1 shows production cross sections for
³⁴⁶ various processes at hadron colliders. The rate for electroweak physics processes
³⁴⁷ including W and Z scale with the center-of-momentum energy, \sqrt{s} .

³⁴⁸ The LHC consists of a 26.7 km (17 miles) ring, approximately 100 m un-
³⁴⁹ derground, outside Geneva, Switzerland. Counter-circulating proton (and occa-
³⁵⁰ sionally heavy ions) beams collide inside four experiments along the beam line:
³⁵¹ ATLAS, CMS, LHCb, ALICE. ATLAS and CMS are general purpose detectors de-
³⁵² signed to explore the high energy frontier. LHCb is designed to study the physics
³⁵³ of b -quarks. ALICE specializes in studying heavy ion collisions.

proton - (anti)proton cross sections

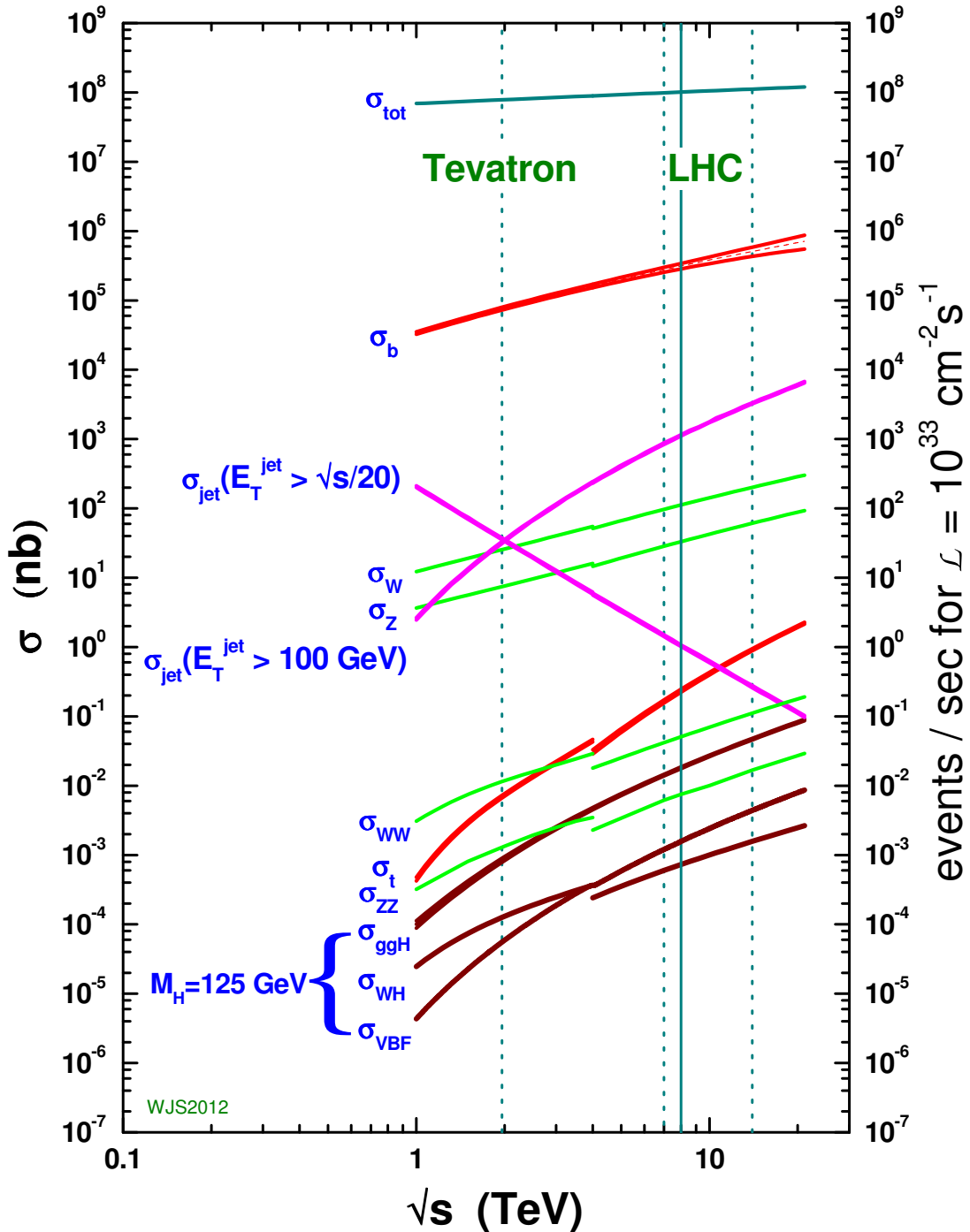


Figure 4.1: Scaling of cross sections with \sqrt{s} . Natasha: write more here

354 The first proton beams circulated in September, 2008. Nine days later an elec-
355 trical fault lead to mechanical damage and liquid helium leaks in the collider. This
356 incident delayed further operation until November 2009, when the LHC became
357 the world's highest energy particle collider, at 1.18TeV per beam. This first oper-
358 ational run continued until 2013, reaching 7 and 8 TeV collision energies. During
359 this run a particle with properties consistent with the Standard Model Higgs bo-
360 son was discovered. The next run began after a two year shutdown after upgrades
361 to the LHC and experiments. This run lasted from 2013 to 2018 reaching 13 TeV
362 collision energies. This analysis uses data from the second operational run.

363 **4.1 LHC Layout and Design**

364 The layout of the LHC is shown in Figure 4.2. The red and blue lines in the
365 figure represent the counter-circulating proton beams. The LHC is divided into
366 eight octants. Octant 4 contains the RF cavities that accelerate the protons and
367 octant 6 contains the beam dump system. Octants 3 and 7 house the collimation
368 systems for beam cleaning. The beams collide inside the four aforementioned
369 experiments. Each octant contains a curved and straight section. The LHC
370 magnets are built with NbTi superconductors cooled with super-fluid Helium to
371 2K, creating a 8.3T magnetic field to bend the proton beams.

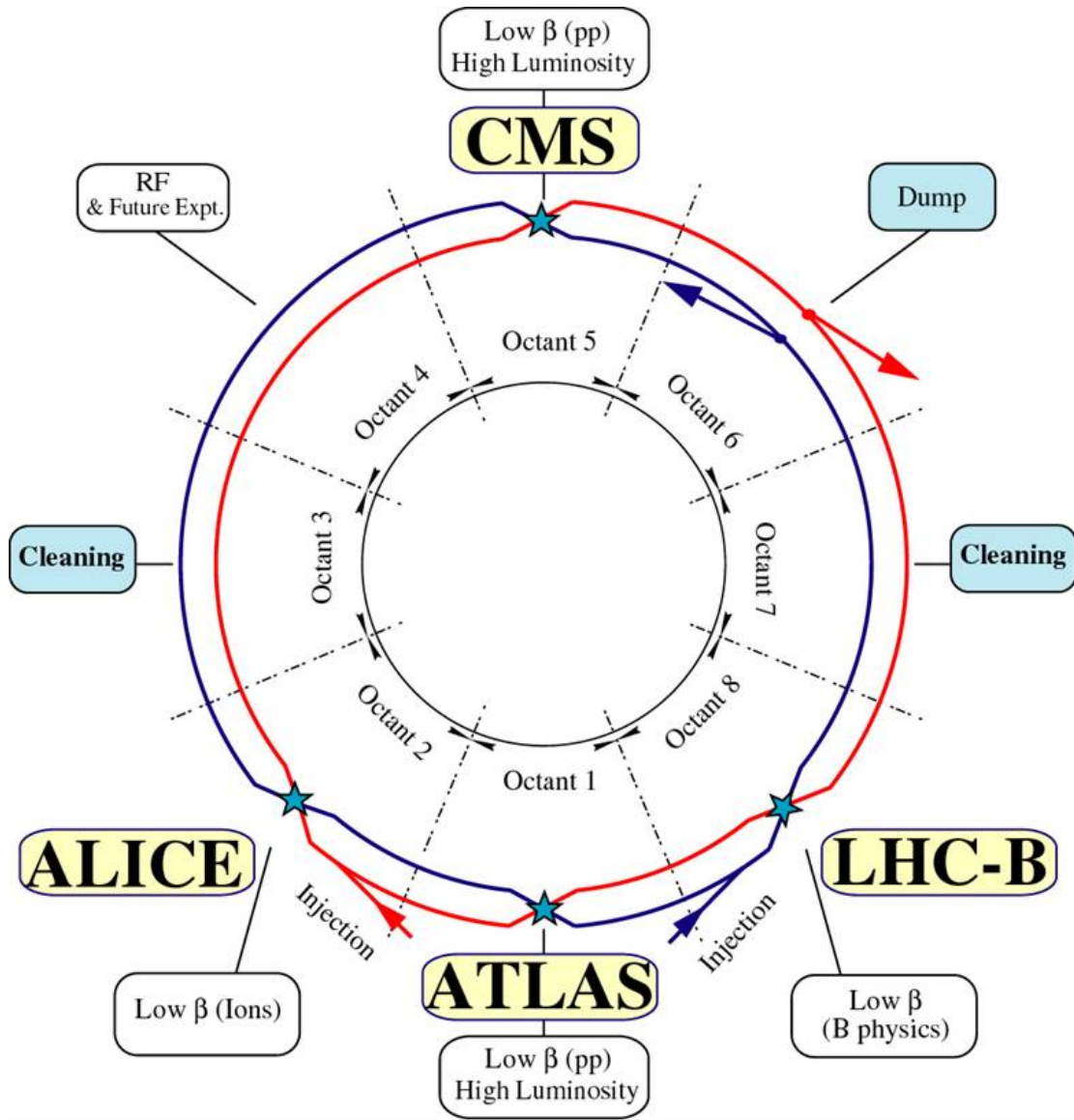
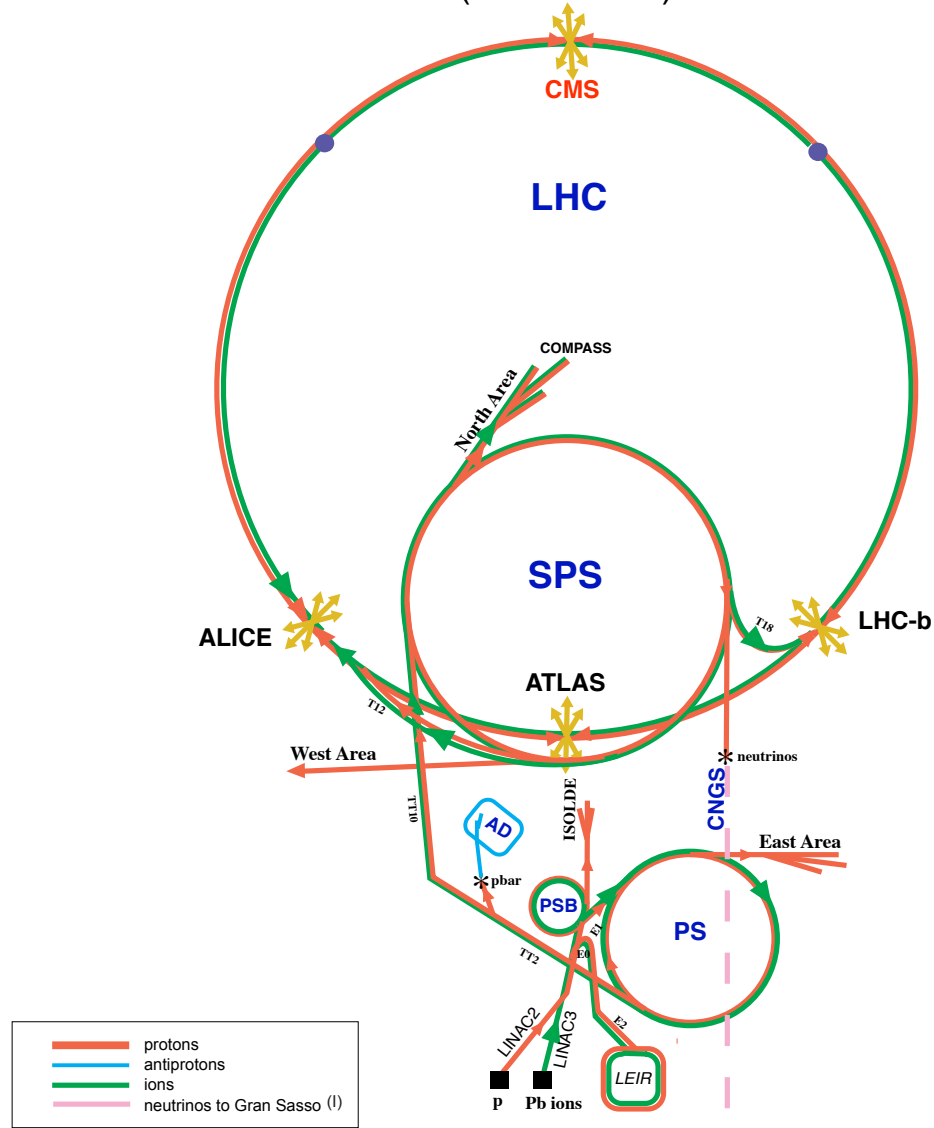


Figure 4.2: LHC Layout. Natasha write more

372 Four sequential particle accelerators are used to accelerate protons from rest
 373 as shown in Figure 4.3. First, Hydrogen gas is ionized to produce protons which
 374 are then accelerated to 50 MeV using Linac 2, a linear accelerator. The result-
 375 ing proton beam is then passed to three circular particle accelerators: Proton
 376 Synchrotron Booster, Proton Synchrotron, and Super Proton Synchrotron (SPS),

³⁷⁷ accelerating protons to 1.4, 25, and 450 GeV, respectively. Once the protons exit
³⁷⁸ the SPS, they are injected into the LHC at octant 2 and 8. Each proton bunch
³⁷⁹ contains $\sim 10^{11}$ protons. The spacing between bunches is 25 ns, which means
³⁸⁰ each beam contains 3564 bunches. However, some bunches are left empty due
³⁸¹ to injection and safety requirements, yielding 2808 bunches per beam. Once the
³⁸² proton beams are injected they are accelerated to 13 TeV.

CERN Accelerators (not to scale)



LHC: Large Hadron Collider

SPS: Super Proton Synchrotron

AD: Antiproton Decelerator

ISOLDE: Isotope Separator OnLine DEvice

PSB: Proton Synchrotron Booster

PS: Proton Synchrotron

LINAC: LINear ACcelerator

LEIR: Low Energy Ion Ring

CNGS: Cern Neutrinos to Gran Sasso

Rudolf LEY, PS Division, CERN, 02.09.96
Revised and adapted by Antonella Del Rosso, ETT Div.,
in collaboration with B. Desforges, SL Div., and
D. Manglunki, PS Div. CERN, 23.05.01

Figure 4.3: LHC Accelerator. Natasha write more

383 As many new physics models predict cross-sections below the weak scale it was
384 important to design the LHC to be capable of collecting enough data, by running
385 in high luminosity conditions. The machine luminosity depends only on beam
386 parameters:

$$L = \frac{N_p^2 f}{4\epsilon\beta^*} F \quad (4.1)$$

387 where N_p is the number of protons per bunch, f is the bunch crossing frequency,
388 ϵ is the transverse beam emittance, β^* is the amplitude function at the collision
389 point, and F is the geometric luminosity reduction factor due to the beams crossing
390 at an angle (rather than head-on).

³⁹¹ **Chapter 5**

³⁹² **The ATLAS Detector**

³⁹³ The ATLAS detector measures the position, momentum and energy of parti-
³⁹⁴ cles produced in the proton collisions by using magnetic fields, silicon detectors,
³⁹⁵ sampling calorimeters, and gaseous wire detectors. It is located approximately
³⁹⁶ 100 m underground at Point-1 around the LHC beam line and weighs 7000 metric
³⁹⁷ tons. The detector is 46 m long, 25 m high, 25 m wide as shown in Figure 5.2.
³⁹⁸ The detector can be divided into three subsystems: the Inner Detector (ID), the
³⁹⁹ Calorimeters, and the Muon Spectrometer (MS). Figure 5.3 shows an overview of
⁴⁰⁰ how different particles interact in the detector.

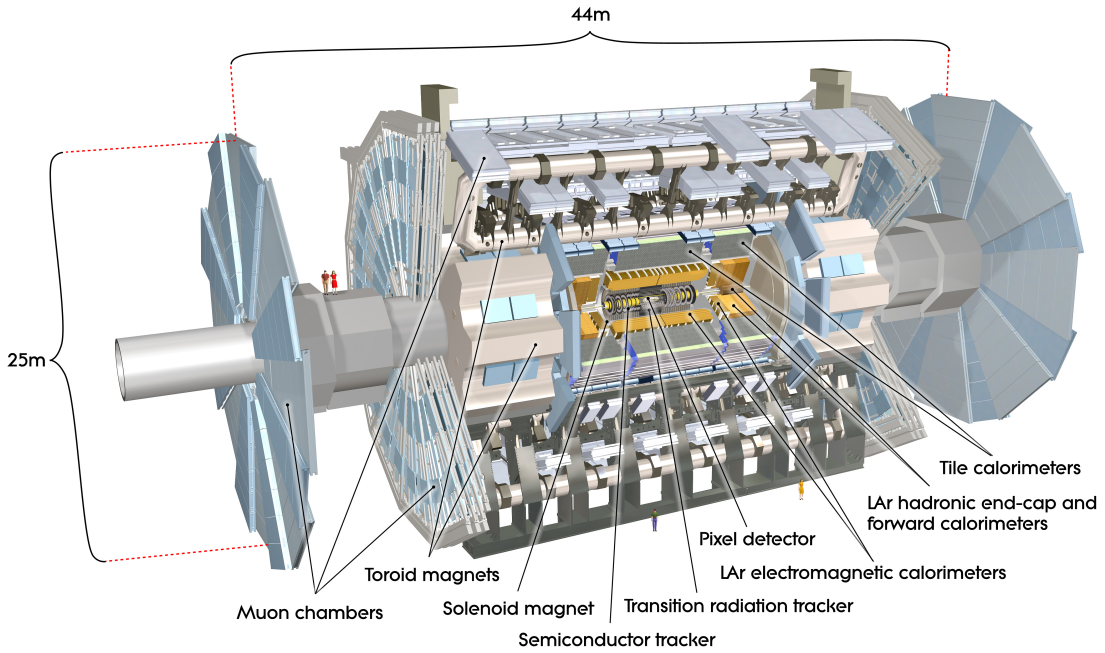


Figure 5.1: Big picture layout of ATLAS detector. Natasha: write more

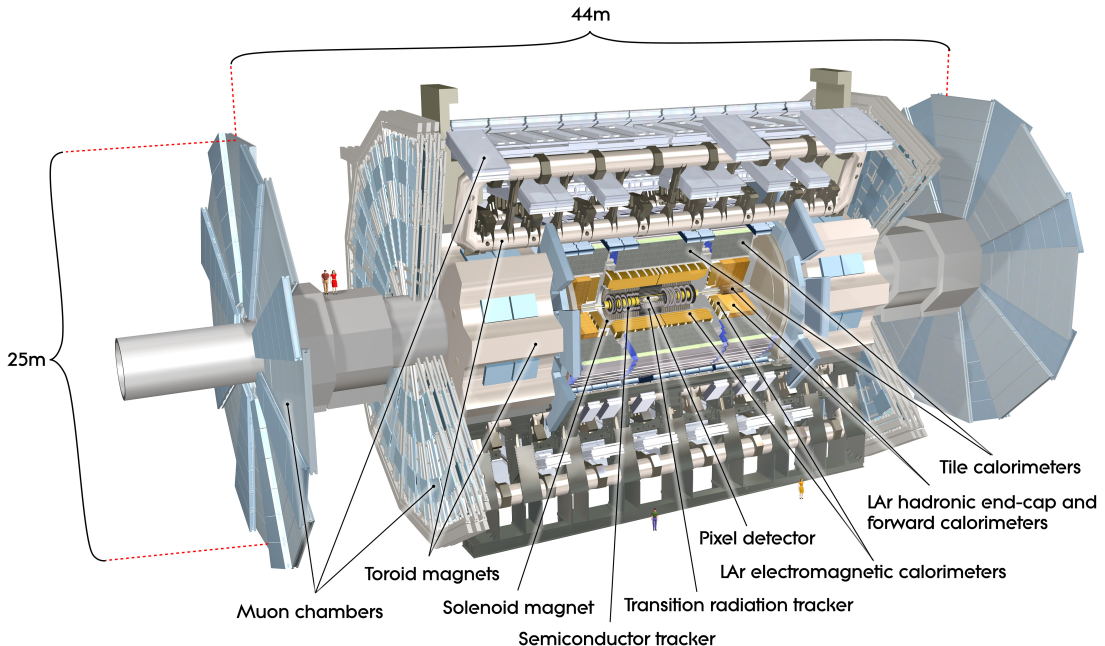


Figure 5.2: Big picture layout of ATLAS detector. Natasha: write more

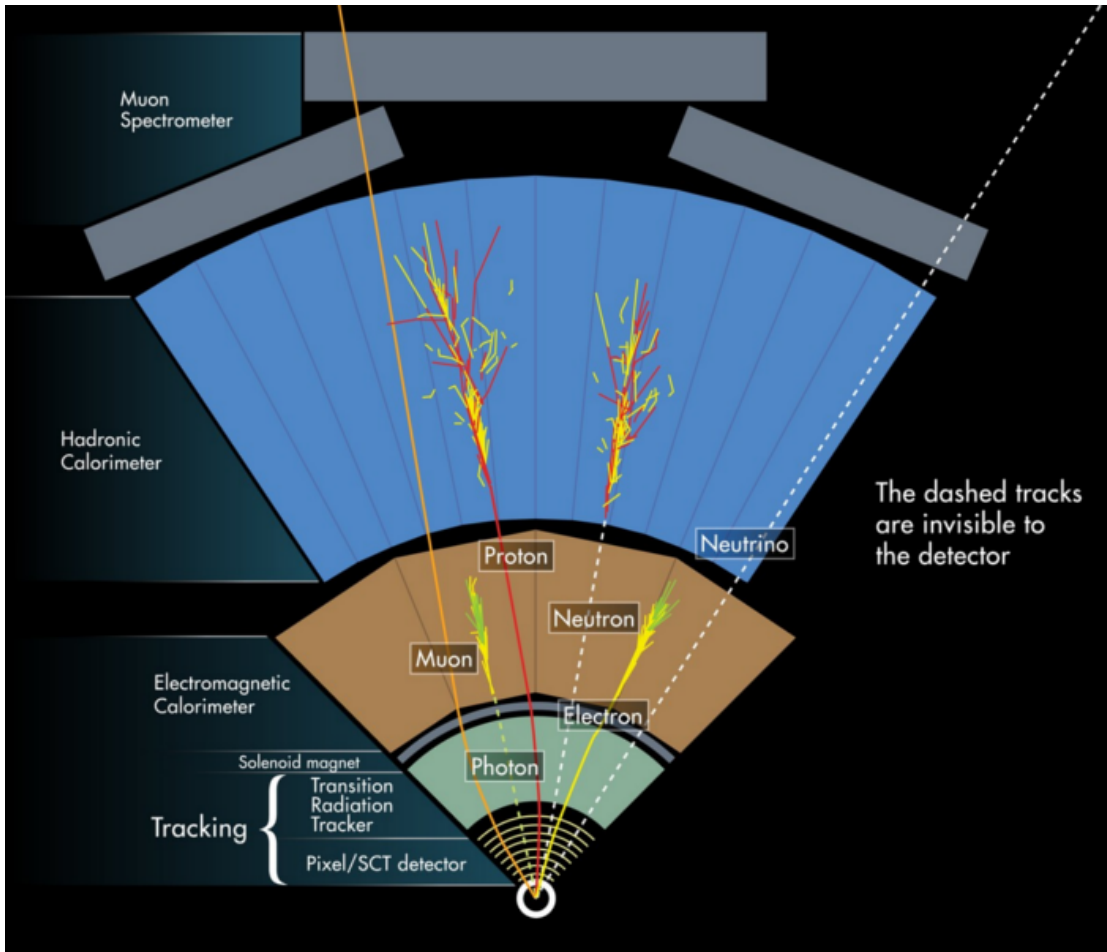


Figure 5.3: A simplified schematic of how different particles interact and are detected within ATLAS.

401 5.1 Coordinate System

402 The trajectory of particles within ATLAS is measured relative to the nominal
 403 interaction point. The z -axis points along the beam line, such that when the
 404 LHC is viewed from above, the counter-clockwise circulating beam points along
 405 the positive- z direction. The $x - y$ plane is transverse to the beam line, with the
 406 positive x -axis pointing towards the center of the LHC ring. The positive y -axis
 407 points vertically upward. The azimuthal angle, ϕ , is the angular distance about

408 the z -axis, with $\phi = 0$ along the x -axis. The polar angle from the z -axis is denoted
409 as θ . However, this quantity is not Lorentz invariant, like rapidity, $y = \frac{1}{2} \ln \frac{E+p_z}{E-p_z}$,
410 where E is the energy of the particle considered, and p_z , is it's momentum along
411 the z -axis. Pseudo-rapidity is preferred as $\Delta\eta$ is invariant under boosts along z
412 and particle production is approximately invariant under η . For massless particles,
413 rapidity and a related quantity, pseudorapidity, are the identical. The pseudora-
414 pidity is defined as: $\eta = -\ln \tan(\frac{\theta}{2})$. This quantity is preferred as it is purely a
415 geometric quantity, independent of particle energy. Angular separation between
416 particles in ATLAS are given by $\Delta R = \sqrt{\Delta\eta^2 + \Delta\phi^2}$. The distance from the
417 beamline is given by $r = \sqrt{x^2 + y^2}$

418 5.2 Inner Detector

419 The Inner Detector (ID) was designed to identify and reconstruct vertices,
420 distinguish pions from electrons, and measure the momentum of charged particles.
421 The ID uses three different technologies for particle reconstruction: the Pixel
422 Detector, Semiconductor Tracker (SCT), and the Transition Radiation Tracker
423 (TRT), shown in Figure 5.4 and 5.5. The entire ID is immersed in a 2T solenoidal
424 magnetic field parallel to the $+z$ -axis, causing charged particles to bend in the
425 transverse-plane, allowing particle momentum measurements.

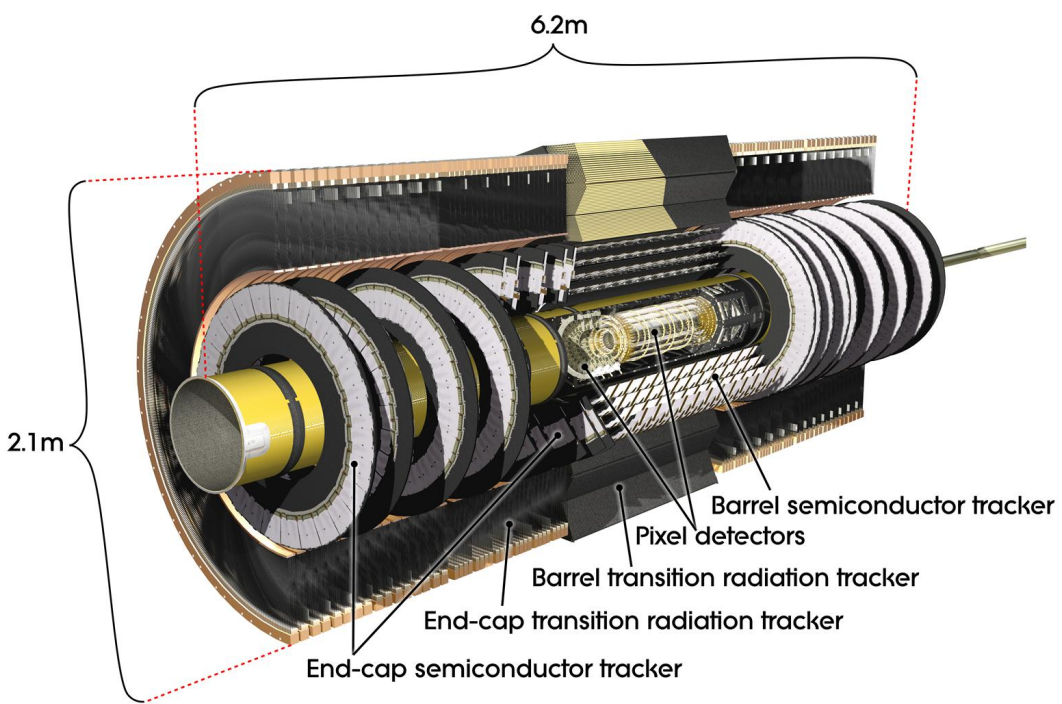


Figure 5.4: Layout of ATLAS Inner Detector

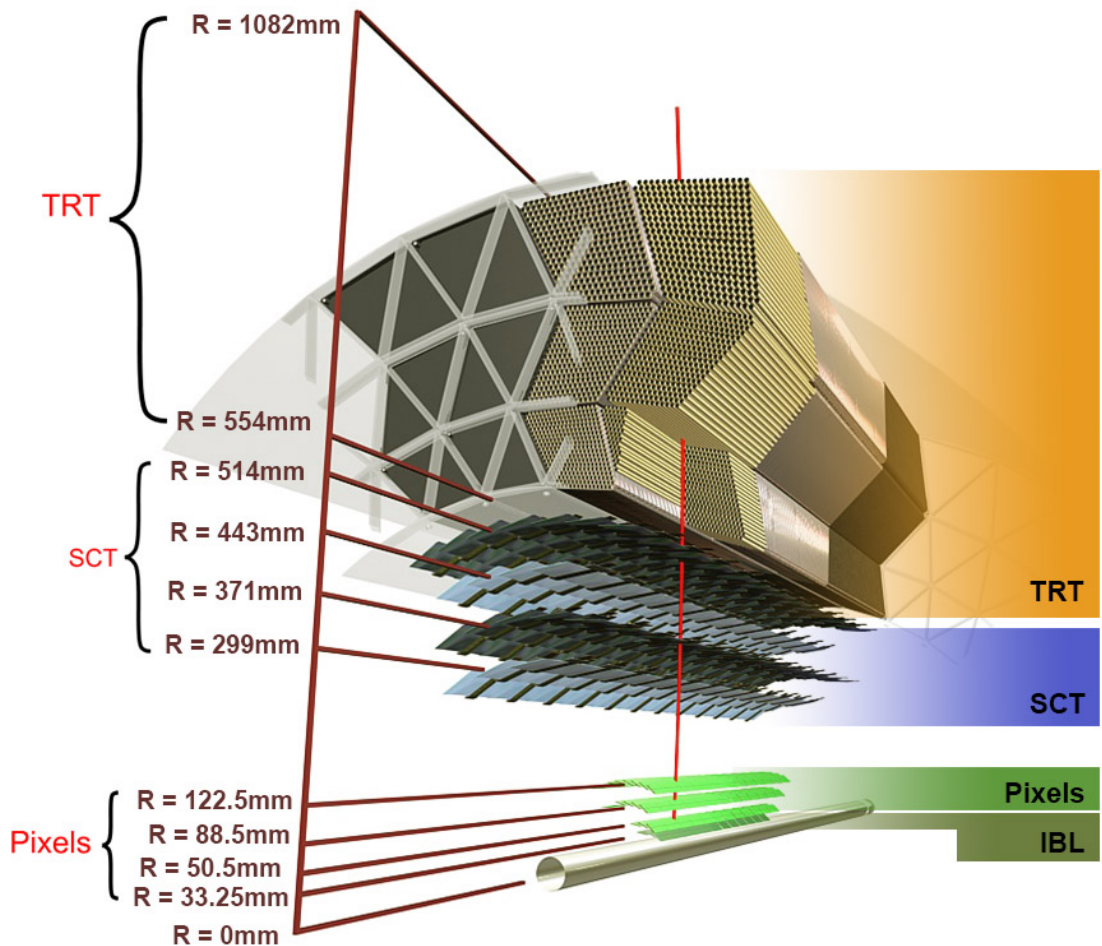


Figure 5.5: Layout of ATLAS ID Barrel System.

426 **5.2.1 Pixel Detector**

427 The pixel detector consists of four barrel layers between $r = 32.7$ and 122.5
428 mm, extending to $|z| = 400.5$ mm. The remaining detectors are arranged in bar-
429 rels and forward and backward rings. The innermost pixel barrel, the Insertable
430 b-Layer (IBL), only extends to $|z| = 332$ mm. The pixel detectors closer to the
431 beam line (larger η values) consists of six parallel cylindrical rings of pixel de-
432 tectors transverse to the beam line. The entire pixel detector consists of 1744
433 identical pixel sensors each with 46080 readout channels, totaling about 80 mil-
434 lion individual pixels. Most of the pixel sensors are $50 \times 400 \mu\text{m}^2$. Each pixel has
435 a position resolution of $14 \mu\text{m}$ in ϕ and $115 \mu\text{m}$ in the z direction.

436 **5.2.2 Semiconductor Tracker**

437 The SCT is located outside the pixel detector and has the same barrel and
438 endcap geometry as the pixel detector. SCT sensors are $80 \mu\text{m} \times 12$ cm with
439 a $80 \mu\text{m}$ strip pitch. In the barrel the strips are parallel to the z -axis and are
440 segmented in ϕ . In the endcaps, the strips extend radially. Sensors are grouped in
441 modules containing two layers of strips rotated 40 mrad with respect to each other.
442 This offset allows for the two-dimensional position of a track to be determined by
443 identifying the crossing point of the strips that registered a hit. SCT modules
444 measure tracks with an accuracy of $17 \mu\text{m}$ in $r - \phi$ and $580 \mu\text{m}$ in $z(r)$ in the
445 barrel (end-cap) region.

446 **5.2.3 Transition Radiation Tracker**

447 The transition radiation tracker (TRT), enveloping the SCT, is a gaseous
448 straw-tube tracker mainly used for electron/pion track separation. Each straw
449 is 4 mm in diameter and filled with a Xe- CO_2 - O_2 gas mixture. An anode wire at

450 the center of the straw is held at ground potential, while the walls of the straw
451 are kept at -1.4kV. When a charged particle passing through the TRT ionizes the
452 gaseous mixture, the resulting ions form an avalanche on the anode wire with a
453 gain of $\sim 10^4$. The signal from the anode wire is then digitized and discriminated.
454 Signals passing a low threshold cutoff are used to distinguish noise from tracks.
455 Signals passing a high threshold cutoff are sensitive to transition radiation (TR).
456 TR photons are emitted when charged particles pass between materials with dif-
457 ferent dielectric constants. The probability that a charged particle with energy E
458 and mass m passing between two materials emits a TR photon in the keV range
459 is proportional to $\gamma = E/m$. In the TRT staws these often then convert via the
460 photoelectric effect, causing a large avalanche triggering the high-threshold. Since
461 electrons have a smaller mass than pions, electron tracks are more likely to trig-
462 ger the high threshold. This then provides discrimination between electrons and
463 charged hadrons.

464 The barrel region of the TRT extends from $r = 563\text{-}1066$ mm and $|z| < 712$
465 mm. Barrel Straws are 144 cm long (divided $\sim \eta \approx 0$) and orientated parallel to
466 the beam direction. End-cap straws extend radially and are 37 cm long. There
467 are 53,544 straws in the barrel and 160,000 straws in the end-caps. Radiator mats
468 of polypropylene/polyethylene fibers in the barrel are aligned perpendicular to the
469 barrel straws (with holes for the straws to pass through). In the end-cap region,
470 radiator foils are layered between the radial TRT straws.

471 The arrival time of the signal pulse is sensitive to the distance between the
472 charged particle track and the anode wire and allows for a hit resolution of $130\mu\text{m}$.
473 The TRT extends to $|\eta| = 2.0$ and provides about 36 hits per track.

474 **5.3 Calorimeters**

475 The ATLAS electromagnetic and hadronic calorimeters (EMC and HCAL,
476 respectively) absorb and measure the energy of high energy hadrons, photons,
477 and electrons with $|\eta| < 4.9$. Both systems use sampling calorimeters which
478 consist of alternating layers of dense absorbing and active layers. In the absorbing
479 layer particles interact and lose energy, creating showers. These showers are then
480 detected and measured in the active layer. The amount of charge measured in the
481 active material scales with the energy of the incident particle, and thus provides a
482 measurement of the particle's energy. An overview of the layout of the calorimeter
483 system is shown in Figure 5.6.

484 The EMC measures and contains the energy of electromagnetically interacting
485 particles. It consists of layered accordion-shaped Lead absorber plates and elec-
486 trodes immersed in liquid Argon with 170k channels.. Using accordion-shaped
487 electrode and absorbers ensures ϕ symmetry and coverage. The EMC is com-
488 posed of a barrel part ($|\eta| < 1.475$), two end-caps ($1.375 < |\eta| < 3.2$), and a
489 presampler ($|\eta| < 1.8$). The presampler, containing only liquid Argon, corrects
490 for upstream energy losses of electrons and photons. The EMC barrel is segmented
491 into three layers. The first layer has finest segmentation with readout cells ex-
492 tending $\Delta\eta \times \Delta\phi = 0.025/8 \times 0.1$. This provides a precise shower measurements
493 used to separate prompt photons from $\pi^0 \rightarrow \gamma\gamma$ decays. The second layer has
494 coarser segmentation and is approximately 16 radiation lengths long. A radiation
495 length is the average distance an electron travels before losing all but $1/e$ of its
496 energy to bremsstrahlung. The last layer is the most coarse and measures the tail
497 of the electromagnetic shower. A schematic of the ECAL is shown in Figure 5.7.

498 The hadronic calorimeter located outside the EMC and is used to contain
499 and measure the energy of hadronically interacting particles. It consists of a tile

500 calorimeter (TileCal), hadronic end-cap calorimeter (HEC), and liquid Argon for-
 501 ward calorimeter (FCAL). TileCal is located behind the LAr EMC and uses steel
 502 absorbers and liquid Argon as the active material. TileCal consists of three barrel
 503 layers in the central and forward regions, extending up to $|\eta| < 1.7$. Photons
 504 generated from hadronic interactions are collected via wavelength-shifting fibers
 505 connected to photomultiplier tubes, as shown in Figure 5.8. The HEC lies behind
 506 the EMC endcap wheels. It uses copper absorbers and liquid Argon as the active
 507 material and covers $1.5 < |\eta| < 3.2$. Finally, the FCAL covers $3.1 < |\eta| < 4.9$
 508 and consists of three modules all using liquid Argon as the active material. The
 509 first module uses copper absorber and was designed for electromagnetic measure-
 510 ments. The second and third modules consist of tungsten absorber and are used
 511 to measure the kinematics of hadronically interacting particles. A schematic of
 512 the HCAL is shown in Figure 5.8.

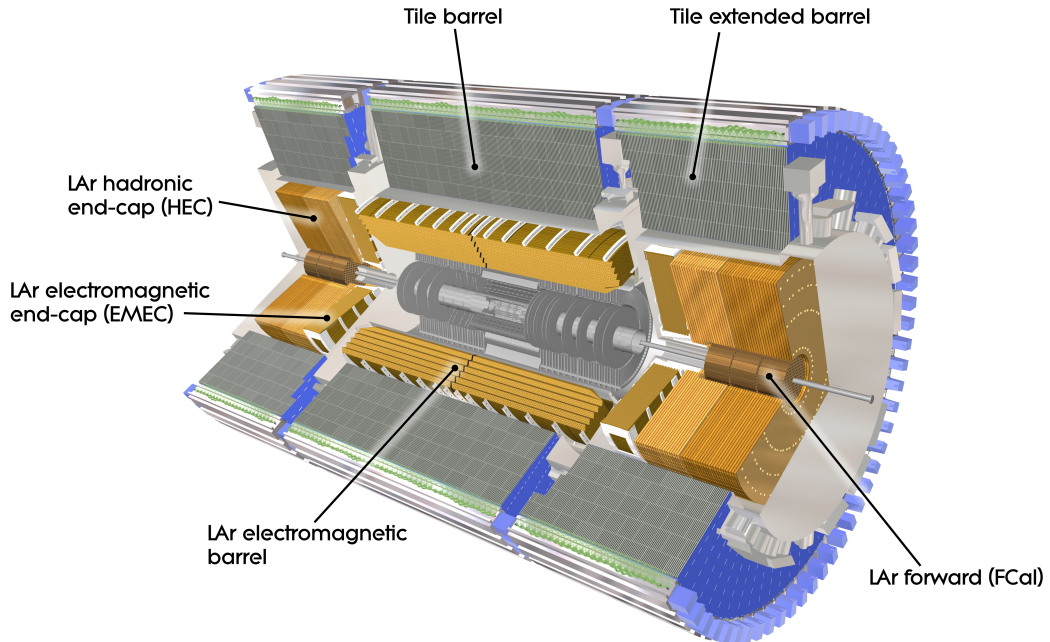


Figure 5.6: Overview of ATLAS electromagnetic and hadronic calorimeters.

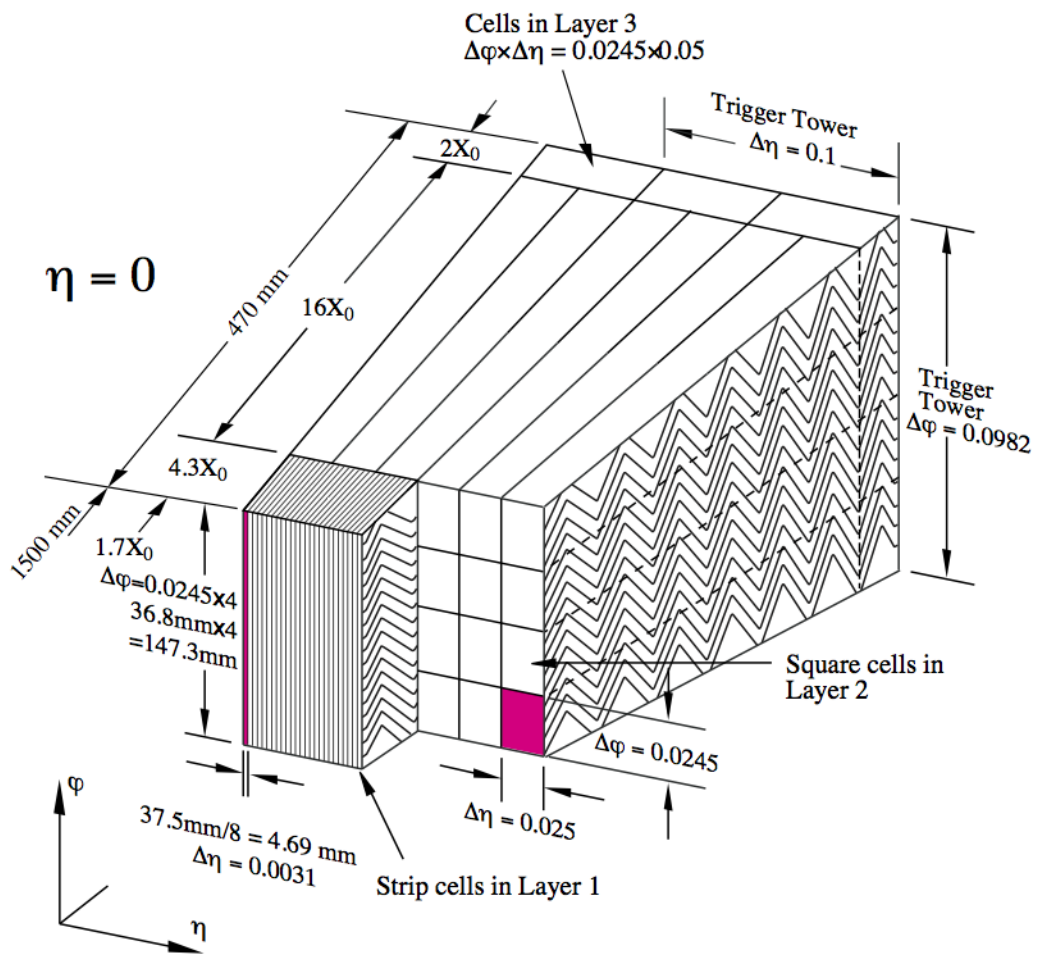


Figure 5.7: Schematic of ECAL.

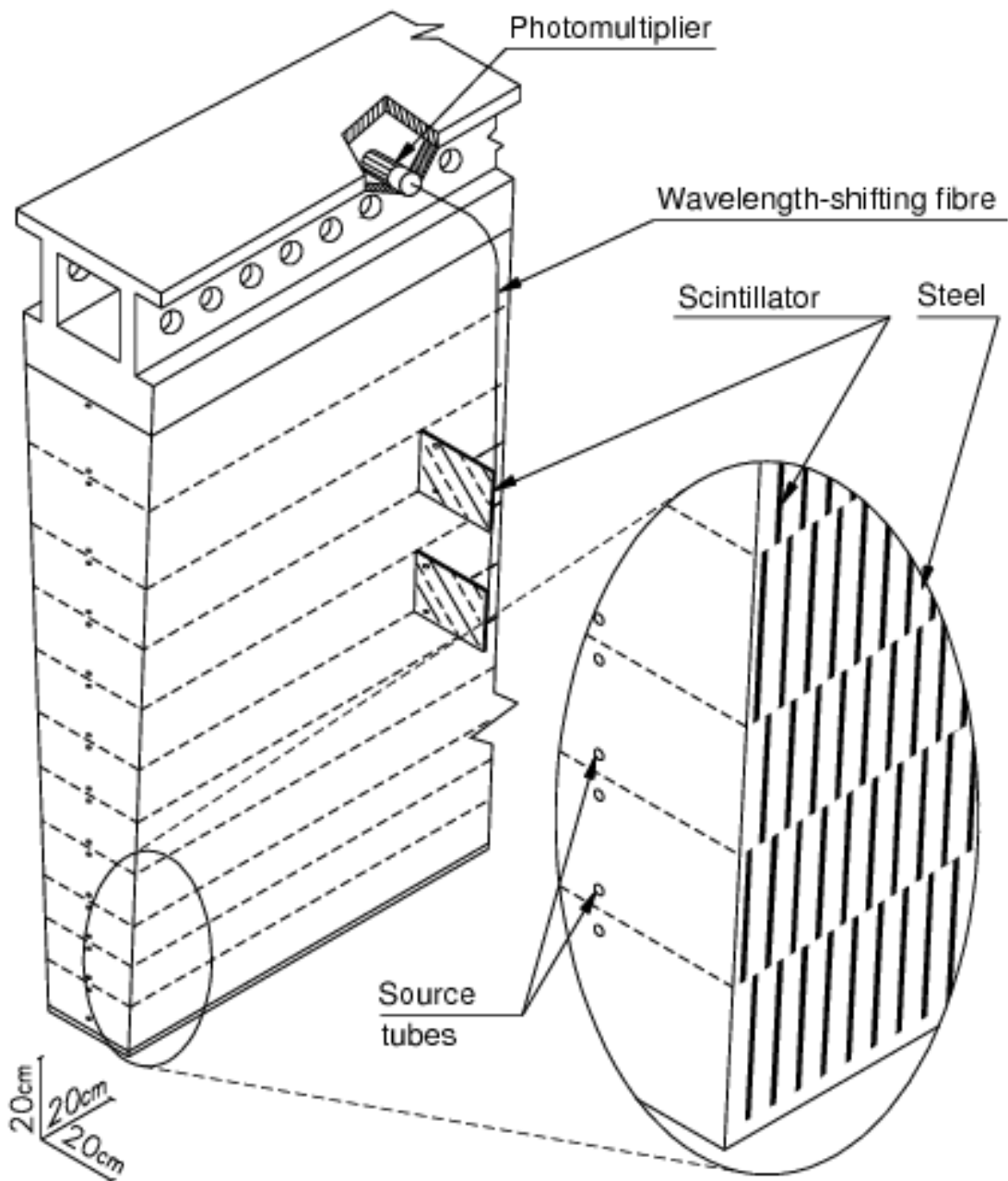


Figure 5.8: Schematic of HCAL.

513 The energy resolution of the calorimeter subsystems are:

514 $\frac{\sigma_E}{E} = \frac{10\%}{\sqrt{E}} \oplus 0.7\% \text{ EMC}$

515 $\frac{\sigma_E}{E} = \frac{50\%}{\sqrt{E}} \oplus 3\% \text{ hadronic barrel}$

516 $\frac{\sigma_E}{E} = \frac{100\%}{\sqrt{E}} \oplus 10\% \text{ hadronic end-cap}$

517 5.4 Muon Spectrometer

518 The muon spectrometer (MS) is the outermost detector system in ATLAS.

519 Muons with a $p_T > 4$ GeV are energetic enough to reach the MS. To measure the
520 momentum of these muons barrel and end-cap toroid magnets are used covering
521 $|\eta| < 1.4$ and $1.6 < |\eta| < 2.7$. For $1.4 < |\eta| < 1.6$, a combination of the barrel
522 and end-cap toroidal magnetic fields bend muon trajectories. The detector in the
523 barrel region form three concentric rings at $R = 5, 7.5, 10$ m and are segmented
524 in ϕ to accommodate the magnets. The end-cap region consists of three circular
525 planes perpendicular to z and located at $|z| = 7.4, 14, 21.5$ m from the interaction
526 region. An additional detector at $|z| = 10.8$ m covers the transition region between
527 the barrel and end-cap.

528 The MS readout consists of four subsystems: Monitored Drift Tubes (MDT),
529 Cathode Strip Chambers (CSC), Resistive Plate Chambers (RPC), and Thin Gap
530 Chambers (TGC). The first two subsystems are used primarily for measuring
531 muon track parameters, while the RPC and TGC subsystems are used for muon
532 triggering. A schematic of this system is shown in Figure 5.9.

533 The MDT subsystem consists of precision tracking chambers for $|\eta| < 2.7$,
534 except for the inner most end-cap layer ($2.0 < |\eta| < 2.7$), where CSCs are used.
535 The basic unit of MDT chambers are thin walled Aluminum tubes with a diameter
536 of 3 cm and length of 0.9-6.2 m. These tubes are filled with a mixture of Ar-CO₂
537 gas with a 50μm W-Rn wire running down the center of the tube, which is kept at

538 3080 V. Since the maximum drift time of these chambers is ~ 700 ns, they are not
539 used for triggering. MDT chambers consist of 3-4 layers of tubes mounted on a
540 rectangular support system, as seen in Figure 5.10, orientated along ϕ to measure
541 the coordinate in the bending plane of the magnetic field with a resolution of 35
542 μm .

543 The MDT subsystem can only handle hit rates below $150\text{Hz}/\text{cm}^2$. For this
544 reason, CSCs are used in the innermost end-cap layer where hit rates are larger.
545 CSCs can handle hit rates up to $1000\text{Hz}/\text{cm}^2$. CSC are multiwire proportional
546 chambers. These chambers are filled with a Ar- CO_2 gas mixture and evenly spaced
547 wires kept at 1900 V. These wires are orientated in the radial direction but not
548 read out. Instead on one side of the cathode are copper strips parallel to the wires,
549 measuring η , while on the other side of the cathode are strips parallel to the wires
550 measuring ϕ . The width between strips is approximately 1.5 mm providing a
551 resolution of 60 μm in the bending-plane and 5 mm in the non-bending plane.

552 Since the CSC and MDT systems do not have prompt timing signals, the RPC
553 and TGC systems are used for triggering. The RPC system is used in the barrel
554 region ($|\eta| < 1.05$). RPC consist of two parallel resistive plates separated by a 2
555 mm insulated spacer with 100 mm spacing kept at 9.8 kV, as shown in Figure 5.11.
556 A gaseous mixture of $\text{C}_2\text{H}_2\text{F}_4$, C_4H_{10} , and SF_6 fills the space between the two
557 plates. Metallic strips on the outer faces of the plates are used to read out signals
558 produced by the gas ionizing. The middle barrel layer consists of two layers of
559 RPCs on either side of the MDT layer and one layer on the outermost MDT
560 layer. Each layer contains two orthogonal sets of metallic strips providing η and
561 ϕ measurements. The timing resolution of RPCs is 1.5 ns, and therefore may be
562 used to identify bunch crossings.

563 Finally, the TGCs are used in the end-cap regions and are primarily used to

564 provide L1 trigger decisions and ϕ measurements. TGCs are multi-wire propor-
 565 tional chambers consisting of arrays of gold-coated tungsten wires placed between
 566 two cathode planes. These wires are separated by 1.8 mm and cathodes are 1.4 mm
 567 from the wires. Orthogonal to the wires, on the opposite side of the cathode plane
 568 are copper strips held at 2900 V. The chambers are filled with a mixture of CO_2
 569 and n-pentane gas, the latter acts as a quenching gas to prevent avalanches initi-
 570 ated by secondary γ -rays from the primary avalanche. Figure 5.12 is a schematic
 571 of a TGC. The timing resolution of TGCs is less than 25 ns and therefore they
 572 are used for bunch crossing measurements.

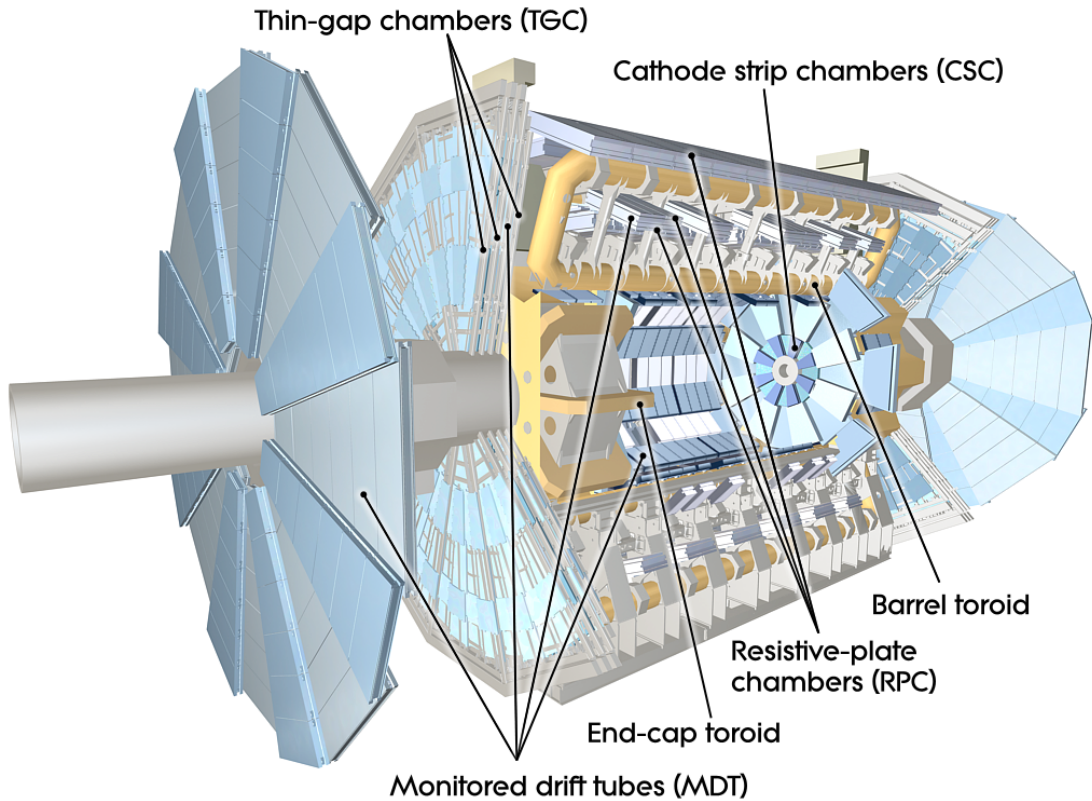


Figure 5.9: Schematic of Muon Spectrometer [cite G35]

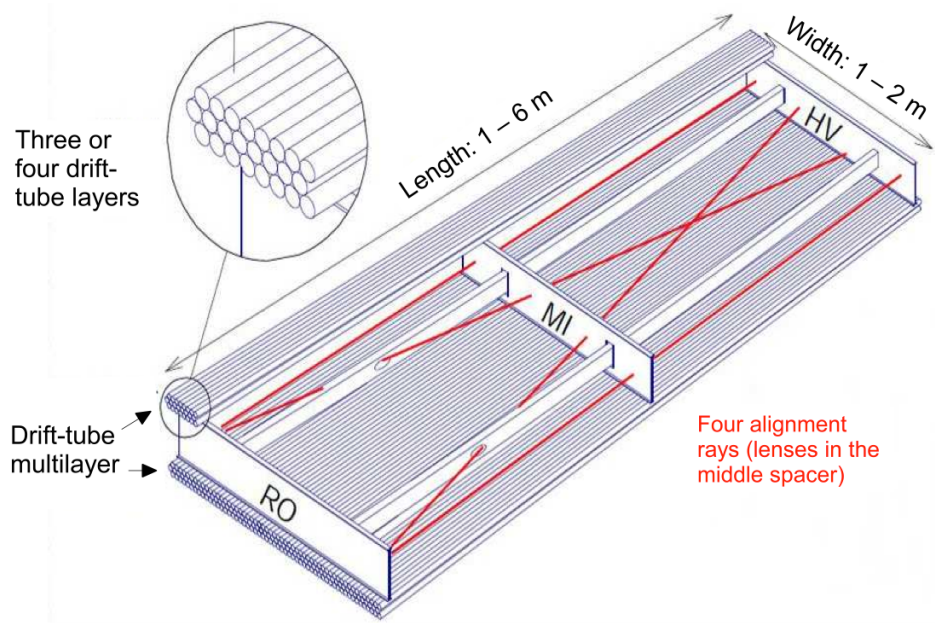


Figure 5.10: Schematic of MDT chamber. [cite G35]

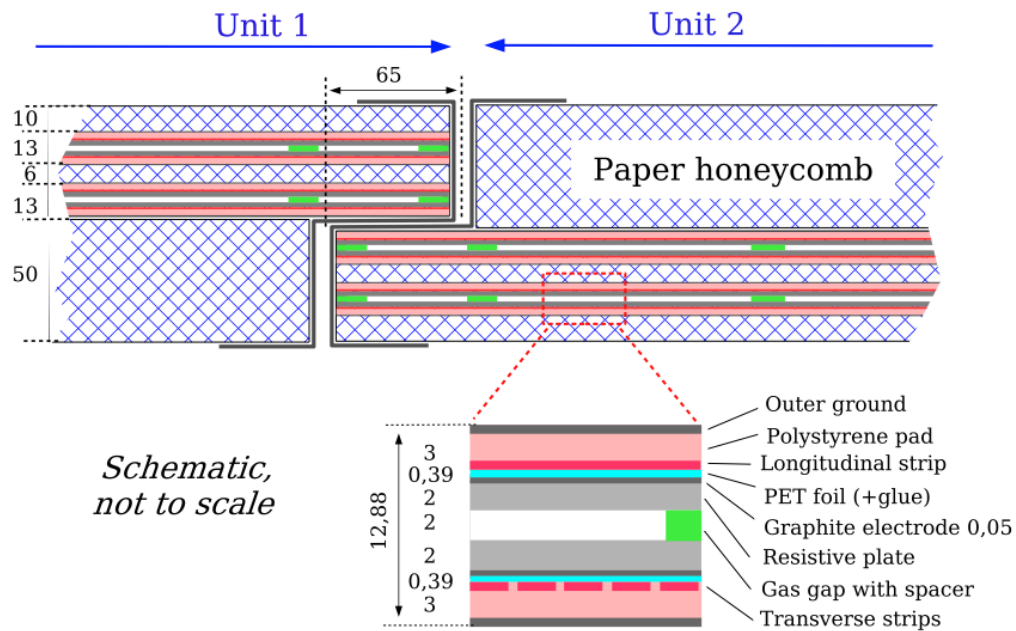


Figure 5.11: Schematic of RPC chamber, which is used for triggering in the central region of the detector [cite G35].

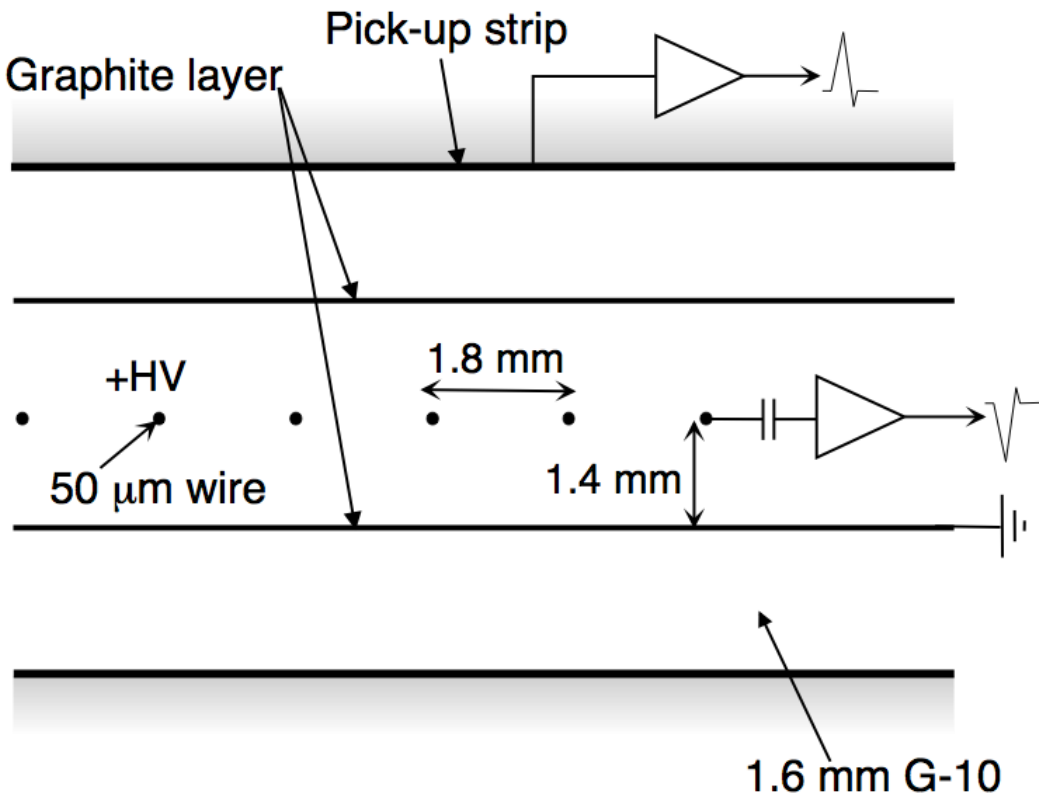


Figure 5.12: Schematic of TGC chamber, which is used for triggering in the muon end-cap region. [cite G35]

5.5 Magnet System

A particles with charge, q , and velocity v , moving in magnetic field, B , experiences a force, $F = qv \times B$. This force can cause charged particles to have a curved trajectory in magnetic fields, which the ID and MS use to determine the particles p_T . The central solenoid provides the magnetic field for the ID and the toroidal magnets provide the magnetic field for the MS.

The layout of the magnet system is shown in Figure 5.13. The central solenoid consists of a single-layer Al-stabilized NbTi conductor coil wound inside an Al

581 support cylinder. The solenoid is 5.8 m long, 50 cm thick and has an inner radius
582 of 1.23 m. It is cooled to 4.5 K to reach superconducting temperatures and shares
583 the liquid argon calorimeter vacuum vessel to minimize material in the detector.
584 A current of 7.730kA produces a 1.998 T solenoidal magnetic field, pointing in
585 the $+z$ direction.

586 The toroidal magnet system consists of a barrel and two end-cap toroidal
587 magnets used to create a magnetic field outside the calorimeters that is orientated
588 along ϕ . Each barrel toroid is 25.3 m long with an inner and outer diameter of 9.4
589 and 20.1 m and weighs 830 tonnes. Endcap toroids are 5 m long with an inner and
590 outer radius of 1.65 and 10.7 m. Both toroid systems use Al-stabilized Nb/Ti/Cu
591 conductors. The magnetic field strength in the barrel and endcap regions are 0.5
592 and 1 T, respectively.

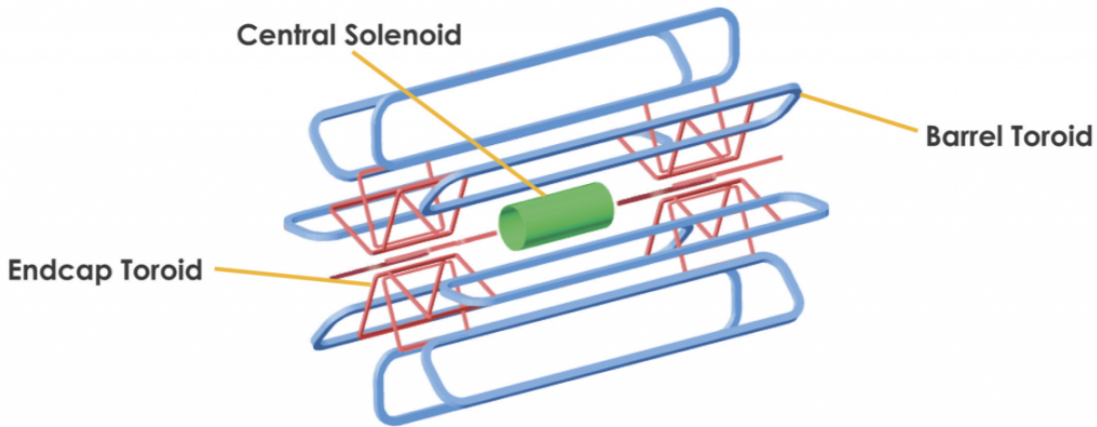


Figure 5.13: Layout of ATLAS magnet systems.

593 5.6 Trigger System

594 Since collisions occur every 25 ns and reading out all detector channels and
595 storing that information is not currently feasible (would require saving 60 million
596 megabytes per second), the majority of events are not kept for analysis. ATLAS

597 uses a multi-stage trigger system to select approximately 1,000 of the 1.7 billion
598 collisions that occur each second (corresponding to a rate of 1 kHz from the 40
599 MHz proton collision rate). The first stage of the trigger system is the hardware
600 level (L1) trigger. This trigger reduces the event rate to \sim 100 kHz by identifying
601 Regions-of-Interest (ROIs) containing high p_T leptons, photons, jets, or E_T^{miss} by
602 using information from RPCs, TGCs, and calorimeters to make a $2.5 \mu\text{s}$ decision.
603 This information is then passed to a high-level trigger (HLT) which further de-
604 creases event rates to \sim 1 kHz. The HLT uses finer granularity measurements
605 from the MS and ID to perform simplified offline reconstruction to decide which
606 events to keep.

Part III

607

Method

608

609 **Chapter 6**

610 **Dataset and Simulated Samples**

611 **6.1 Dataset**

612 This analysis uses pp collision data collected from 2015 to 2018 at $\sqrt{s} = 13$
613 TeV, corresponding to 139/fb of data as shown in Figure 6.1 and 6.2. From this
614 dataset, only those events in which the tracker, calorimeters, and muon spectrom-
615 eter have good data quality are used. For a given event, the solenoid and toroidal
616 magnets must also be operating at their nominal field strengths. In addition to
617 this, events must pass further quality checks to reject events where detector sub-
618 systems may have failed. These selections reject events that containing LAr noise
619 bursts, saturation in the electromagnetic calorimeter, TileCal errors, and failures
620 in event recovery due to tracker failures. Events with information missing from
621 subsystems (usually due to busy detector conditions) are rejected. Events must
622 also contain a primary vertex with at least two associated tracks, where the pri-
623 mary vertex is selected as the vertex with the largest $\sum p_T^2$ over tracks associated
624 with the vertex and $p_T > 0.5$ GeV.

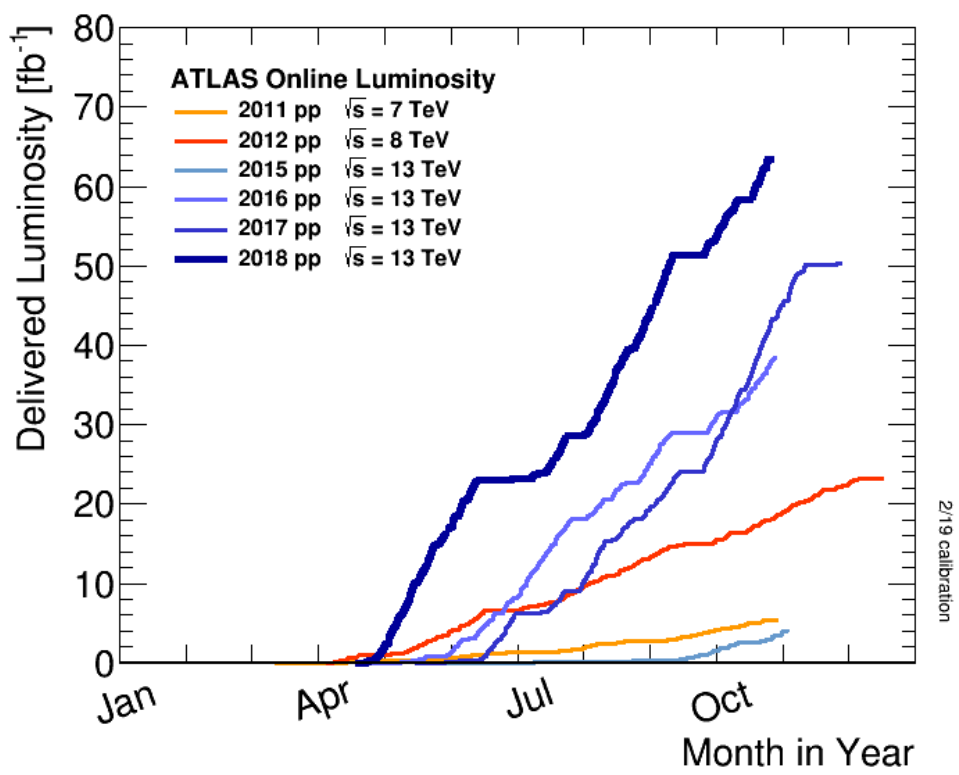


Figure 6.1: Integrated luminosity for data collected from ATLAS from 2011 - 2018

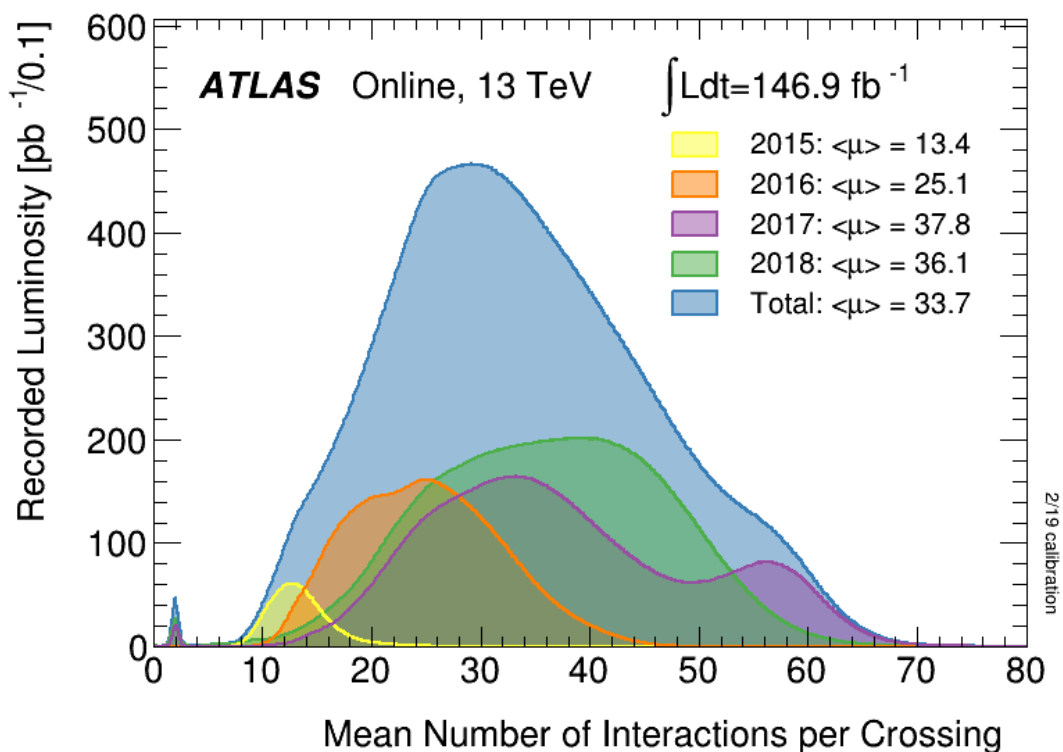


Figure 6.2: Mean number of interactions per crossing for data collected from ATLAS from 2011 - 2018

625 **6.2 Simulated Samples**

626 Samples are simulated in order to model backgrounds, evaluate signal ac-
627 ceptance, optimize event selection and estimate systematic and statistical uncer-
628 tainties. The dominant backgrounds for this analysis are $W/Z + \text{jets}$, diboson
629 (WZ/WW), $t\bar{t}$, single top and multijet production.

630 $W/Z+\text{jet}$ events are simulated using Sherpa 2.2.1 at NLO [cite [29]] and merged
631 with the Sherpa parton shower using the ME+PS@NLO prescription [11]. These
632 events are then normalized to NNLO cross sections. The $t\bar{t}$ and single-top back-
633 grounds are generated with Powheg-Box with NNPDF3.0NLO PDF sets in the
634 matrix element calculation [cite[35]]. For all processes, the parton shower, frag-
635 mentation, and underlying event are simulated using Pythia 8.320 with the A14
636 tune set[cite[ATL-PHYS-PUB-2014-02]]. Diboson processes are generated using
637 Sherpa 2.2.1.

638 Signal samples are simulated using MadGraph 5-2.2.2 [cite 42] and Pythia
639 8.186 with NNPDF230LO. RS Graviton samples are generated with $k/M_{PL}=1$.
640 HVT Model A (B) samples are simulated with $g_V = 1(3)$, as the difference in the
641 width of the samples is smaller than detector resolution. Model C is generated by
642 setting $g_H = 1$ and $g_f = 0$ to model VBF production of HVT bosons. Signals are
643 generated for masses between 300 GeV and 5 TeV.

644 **6.3 Object Selection**

645 **6.3.1 Electrons**

646 Electrons are reconstructed from electromagnetic showers in the LAr EM
647 calorimeter. During reconstruction cells of $\Delta\eta \times \Delta\phi = 0.025 \times 0.025$ are grouped
648 into 3×5 clusters. These clusters are then scanned for local maxima that seed

649 electron clusters. These clusters must then be matched to ID track from the PV.
650 This requirement minimizes non-prompt electron and fake electron backgrounds.
651 Electrons must pass identification and isolation requirements. Electron identifica-
652 tion (loose, medium, tight) classification is based on a multivariate discriminant
653 that identifies electrons using a likelihood based method. For this analysis tight
654 electrons are used. Electrons are also required to be isolated. The electrons are
655 considered isolated if the quotient of the sum of the transverse momentum (of
656 calorimeter energy deposits) in a cone around the electron of size $\Delta R = 0.2$ and
657 the transverse momentum of the electron to be less than $0.015 * p_T$ or 3.5 GeV,
658 whichever is smaller. This requirement rejects non-prompt photons and other
659 fake leptons. Electrons in this analysis are also required to have $p_T > 30$ GeV and
660 $|\eta| < 2.47$. Electrons are also required to have $p_T > 30$ GeV.

661 Electrons are calibrated to determine data-driven scale factors using $J/\Psi \rightarrow$
662 ee , $Z \rightarrow ee$, $Z \rightarrow \ell\ell\gamma$ processes. These corrections account for the non-uniform
663 response of the detector which introduces modeling and reconstruction uncertain-
664 ties.

665 6.3.2 Muons

666 As muons traverse the entire detector, they are reconstructed from ID and MS
667 tracks. For this analysis the muon identification and isolation working points are
668 chosen to minimize the contributions from non-prompt muons. Towards this end,
669 the medium muon identification working point is used. For this working point,
670 two types of reconstructed muons are used: combined and extrapolated muons
671 (CB and ME, respectively). For CB muons, ID and MS tracks are reconstructed
672 independently and a combined track fit is performed by adding or removing MS
673 tracks to improve the fit quality. ME muons are reconstructed from only MS

674 tracks with hits in at least two layers, which ensures the track originates from the
675 PV. ME muons extend the acceptance for muon reconstruction outside the ID
676 from $2.5 < |\eta| < 2.7$. The medium identification working point uses CB and ME
677 tracks. CB tracks must have at least 3 hits in two MDT layers. ME tracks are
678 required to have at least three MDT/CSC hits. To further minimize contributions
679 from fake muons, the selected muons are required to be isolated from other tracks,
680 as muons from W, Z decays are often isolated from other particles. To insure the
681 selected muons are isolated, the scalar sum of the transverse momentum of tracks
682 in a cone of $\Delta R = 0.3$ compared to the transverse momentum of the muon must
683 be less then 0.06. Muons are also required to have $p_T > 30$ GeV.

684 Muons are calibrated using well-studied resonances $J/\Psi \rightarrow \mu\mu$ (low- p_T), $Z \rightarrow$
685 $\mu\mu$ (high- p_T). Figure 6.3 shows the combined muon p_T uncertainty from this
686 calibration. The total systematic uncertainty is less then 1% for all p_T ranges
687 considered in this analysis.

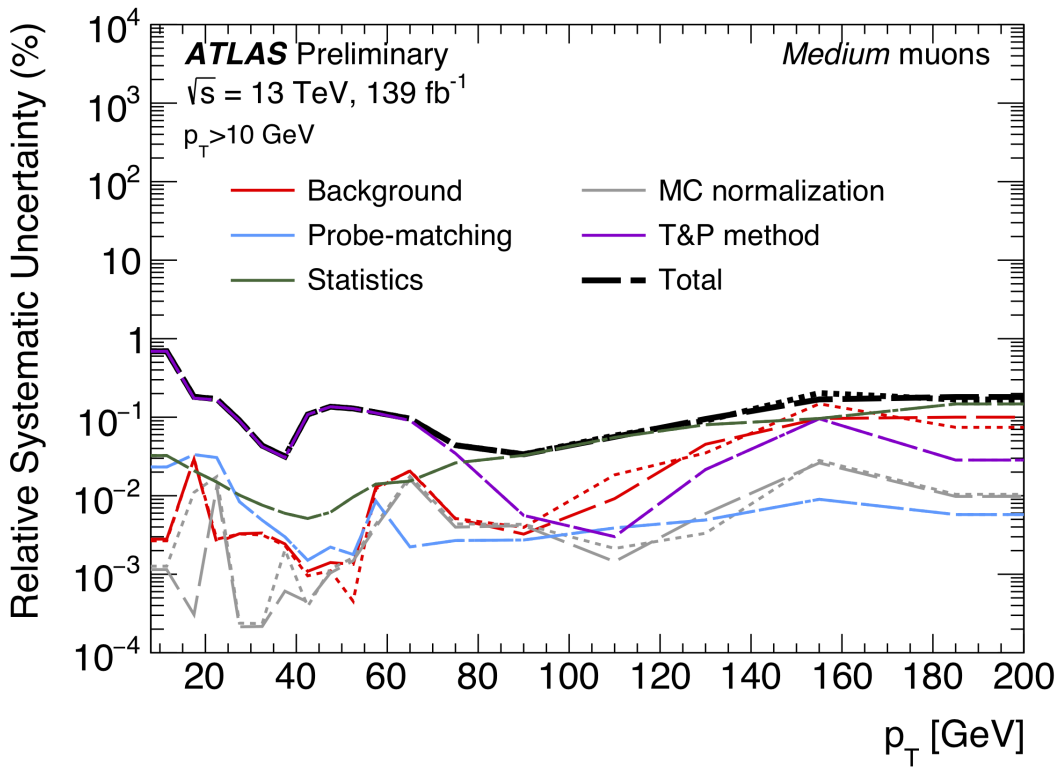


Figure 6.3: This figure shows the breakdown of the muon reconstruction efficiency scale factor measured in $Z \rightarrow \mu\mu$ as a function of p_T [4].

688 6.3.3 small-R jets

689 Small-R jets are used to reconstruct the hadronically decaying W/Z candi-
 690 dates in the resolved analysis and VBF jets. These jets are less boosted and
 691 therefore spatially separated and reconstructed separately. These jets are con-
 692 structed from topologically connected clusters of calorimeter cells (topoclusters),
 693 seeded from calorimeter cells with energy deposits significantly above the noise
 694 threshold. These cells are then used as inputs to the $anti - k_t$ algorithm [12] with
 695 a distance = 0.4, here called small-R jets. These jets are calibrated to compensate
 696 and account for biases from jet reconstruction.

697 The jet energy is calibrated sequentially as shown in Figure 6.4. After the jet

698 direction is corrected to point to the PV, the energy of the jet is corrected. First,
699 the jet energy is corrected to account for pileup contributions based on the p_T and
700 area of the jet (these corrections are extracted from a $pp \rightarrow jj$ sample). Following
701 this, another pileup correction is applied that scales with μ and N_{PV} .

702 MC-based corrections are then applied that are meant to transform the jet
703 energy and η back to truth level. Therefore, these corrections account for the
704 non-compensating nature of the ATLAS calorimeters and inhomogeneity of the
705 detector. Following this, the Global Sequential Calibration is applied that re-
706 duces flavor dependence of jet calibrations and accounts for energy leakage of jets
707 outside the calorimeters. Finally, in-situ corrections are applied that account for
708 differences in jet responses between data and simulation ($\gamma/Z+jet$ and multijet
709 samples are used). These differences can be due to mismodelling of the hard
710 scatter event, pile-up, jet formation, etc.

711 Jets used in this analysis must have $p_T > 30$ GeV and $|\eta| < 2.5$. To further
712 reduce fake jets the jet-vertex-tagger (JVT) is used to reject pile-up jets [cite 43
713 P]. The JVT uses two track-based variables, corrJVF and R_{p_T} to calculate the
714 likelihood that the jet originated from the PV. The corrJVF compares the scalar
715 sum of the p_T of tracks associated with the jet and PV to the scalar sum of the
716 p_T of tracks associated with the jet. This variable also includes a correction that
717 reduces the dependency of corrJVF with the number of reconstructed vertices in
718 the event. The other discriminant, R_{p_T} , is given by the ratio of the scalar sum
719 of the p_T of tracks associated with the jet and PV to the p_T of the jet. Both of
720 these variables peak around zero for pileup jets, as these jets are unlikely to have
721 tracks associated with the PV. JVT cuts are applied to all jets with $p_T > 120$
722 GeV. Central jets ($|\eta| < 2.4$) are required to have a $JVT > 0.59$ and forward jets
723 ($2.4 < |\eta| < 2.5$) are required to have $JVT > 0.11$.

724 To further reject fake jets, jets must pass quality requirements based on the
725 following variables ([cite P42]):

- 726 - f_Q^{LAr} : fraction of energy of jet's LAr cells with poor signal shape
- 727 - f_Q^{HEC} : fraction of energy of jet's HEC cells with poor signal shape
- 728 - E_{neg} : sum of cells with negative energy
- 729 - f_{EM} : fraction of jet's energy deposited in EM calorimeter
- 730 - f_{HEC} : fraction of jet's energy deposited in HEC calorimeter
- 731 - f_{max} : maximum energy fraction in any single calorimeter layer
- 732 - f_{ch} : ratio of the scalar sum of the p_T of a jet's charged tracks to the jet's p_T

733 Jets selected for the resolved analysis must pass one of the following criteria:

- 734 - $f_{HEC} > 0.5$ and $|f_Q^{HEC}| > 0.5$ and $\langle Q \rangle > 0.8$
- 735 - $|E_{neg}| > 60$ GeV
- 736 - $f_{EM} > 0.95$ and $f_Q^{LAr} > 0.8$ and $\langle Q \rangle > 0.8$ and $|\eta| < 2.8$
- 737 - $f_{max} > 0.99$ and $|\eta| < 2$
- 738 - $f_{EM} < 0.05$ and $f_{ch} < 0.05$ and $|\eta| < 2$
- 739 - $f_{EM} < 0.05$ and $|\eta| > 2$

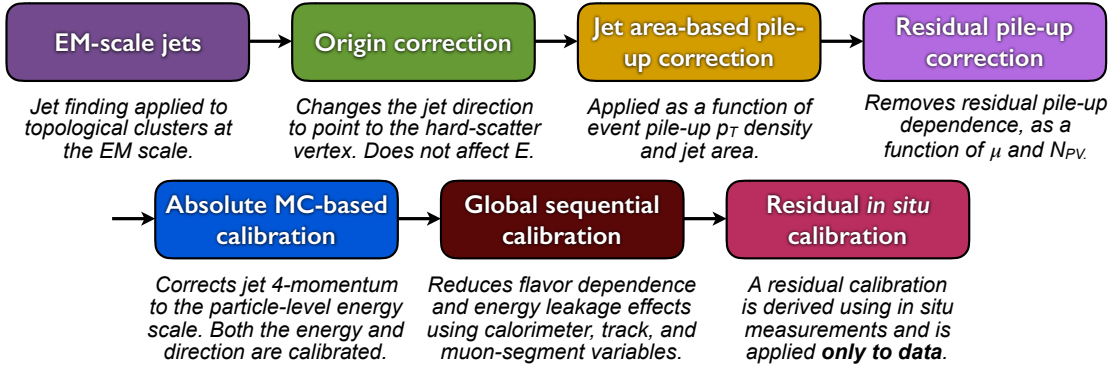


Figure 6.4: [6] This diagram shows the calibration stages for EM jets.

740 6.3.4 large-R jets

741 Large-R ($\Delta R = 1.0$) jets are used to reconstruct the high- $p_T W/Z \rightarrow qq$ candi-
 742 dates in the merged analysis. Track-Calorimeter Clusters (TCCs) are used to reconstruct
 743 these jets [cite ANA 50]. These jets are constructed via a pseudo particle flow
 744 method using ID tracks matched to calorimeter clusters. The angular resolution
 745 of the calorimeter degrades sharply with jet p_T , but the jet energy resolution
 746 improves. The tracker has excellent angular resolution which improves with p_T .
 747 Therefore, by matching tracks to jets, TCCs have more precise energy and angular
 748 resolution than jets constructed from calorimeter information only. These jets are
 749 required to have $p_T > 200$ GeV, $|\eta| < 2.0$ and $m_J > 50$ GeV.

750 TCC jets are trimmed as detailed in [cite ANA 45], which suppresses pileup
 751 and soft radiation in the jet, the jet mass is calculated as the four-vector sum
 752 of the jet's constituents (assuming massless constituents). The jet mass peaks
 753 around the W/Z boson mass for $W/Z \rightarrow qq$ jets, and more broadly for quark and
 754 gluon induced jets.

755 These jets are then tagged as W/Z jets if they pass the jet mass and D_2
 756 cuts. The jet substructure variable D_2 is given by the ratio of energy correlation
 757 functions based on energies and pair-wise angles of a jet's constituents [cite ANA

758 46, 47]:

$$D_2^{\beta=1} = E_{CF3} \left(\frac{E_{CF1}}{E_{CF2}} \right)^3 \quad (6.1)$$

759 Where the energy correlation functions are defined as:

$$E_{CF1} = \sum_i p_{T,i} \quad (6.2)$$

760

$$E_{CF2} = \sum_{ij} p_{T,i} p_{T,j} \Delta R_{ij} \quad (6.3)$$

761

$$E_{CF3} = \sum_{ijk} p_{T,i} p_{T,j} p_{T,k} \Delta R_{ij} \Delta R_{jk} \Delta R_{ki} \quad (6.4)$$

762 A two-dimensional optimization of the jet mass and D_2 thresholds was per-
763 formed to provide maximum sensitivity for this analysis. Figure 6.5 shows the
764 optimized thresholds on D_2 and jet mass as a function of p_T . Figure 6.6 shows
765 the efficiency of the optimized W/Z taggers as a function of jet p_T .

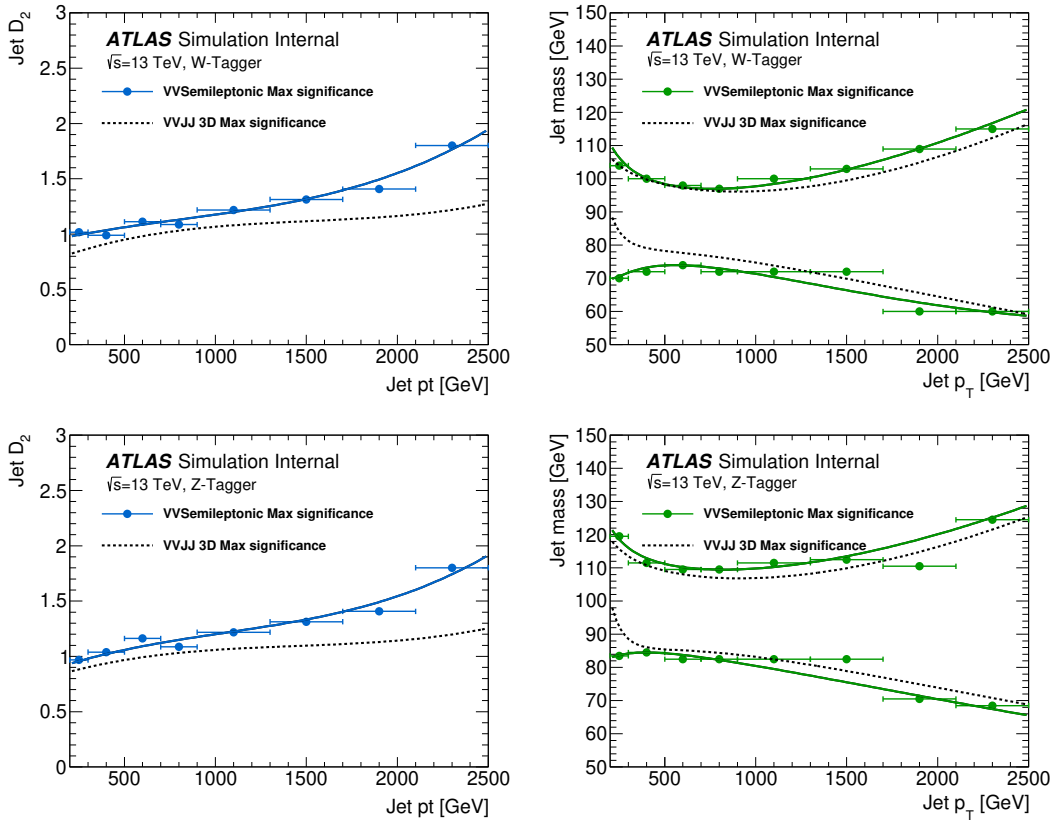


Figure 6.5: The upper cut on D_2 (a) and jet mass window cut i.e. the upper and lower boundary of the mass (b) of the W -tagger as a function of jet p_T . Corresponding values for Z -tagger are shown in (c) and (d). The optimal cut values for maximum significance are shown as solid markers and the fitted function as solid lines. Working points from $VV \rightarrow JJ$ [ATLAS-HDBS-2018-31-002] is also shown as dashed lines as a reference. Natasha reword?

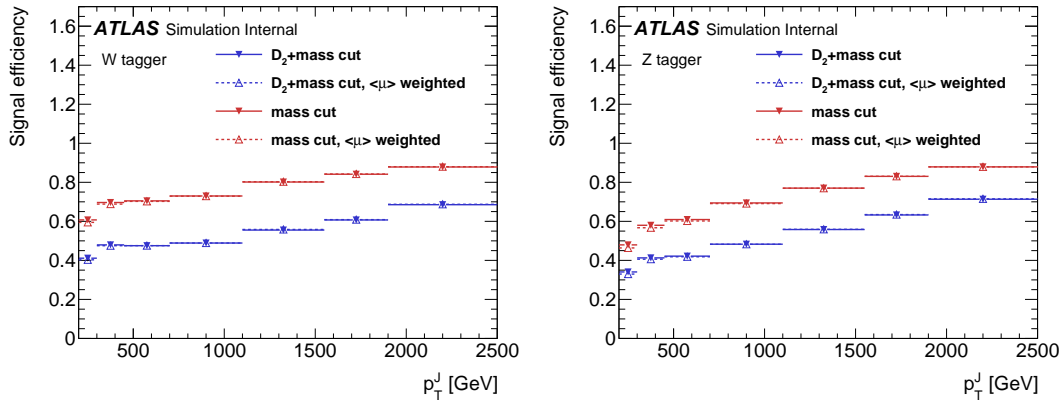


Figure 6.6: Natasha write caption

766 **6.3.5 Variable Radius jets**

767 Variable-radius (VR) track jets are used to identify b-quark induced jets within
768 the catchment area of large-R jets [cite ANA 52]. These jets use a p_T dependent
769 cone size defined as:

$$R_{eff}(p_{T,i}) = \frac{\rho}{p_{T,i}} \quad (6.5)$$

770 for building jets from ID tracks with an anti- k_t algorithm. For this analysis $\rho = 30$
771 GeV and an upper and lower limit on cone size are set to 0.02 and 0.4, respectively.
772 Collinear VR jets are possible, so track jets that are not separated by the the
773 smaller jet's cone size are not used. These jets are also required to have $p_T > 10$
774 GeV and $|\eta| < 2.5$.

775 **6.3.6 MET/neutrinos**

776 As neutrinos are uncharged and colorless they do not leave tracks or jets in the
777 detector. For this reason, neutrinos are reconstructed calculated the E_T^{miss} , the
778 negative vector sum of p_T all the physics objects and an extra "soft" term. The
779 "soft" term accounts for energy deposits not associated with any of the objects in
780 the event. For this analysis the soft term is given by the sum p_T of all ID tracks
781 not associated with objects in the event. The selected tracks must be matched to
782 the primary vertex, which decreases pile-up contamination [cite G 217 218]. The
783 tight working point is used [Natasha look up what this means].

784 **6.3.7 Jet Flavor Tagging**

785 To further classify events, the small radius jets originating from a b-quark are
786 classified using a multivariate b -tagging algorithm (BDT), MV2c10 [cite G 210
787 199]. This algorithm uses the impact parameters of the jet's ID tracks, secondary

788 vertices (if they exist), and reconstructed flight paths of b and c hadrons in the
789 jet to determine if the jet was induced by a b -quark. For this analysis the 85%
790 efficient working point of this algorithm is used giving c , τ , and light-flavor jet
791 rejection of 3, 8, and 34 respectively in a simulated $t\bar{t}$.

792 6.3.8 Overlap Removal

793 Reconstructed jets and leptons in this analysis can arise from the same energy
794 deposits. For instance, a cluster of energy from an electron can also be a valid
795 calorimeter seed for a jet. To mitigate this confusion of multiple objects originating
796 from a single jet or lepton overlapping objects are removed via a procedure referred
797 to as overlap removal. In this procedure the separation of the two objects, $\Delta(R) =$
798 $\sqrt{(\Delta\eta)^2 + (\Delta\phi)^2}$ determines which object is removed from the event.

799 The overlap selections used in this analysis are:

- 800 - when an electron shares a track with another electron with the lower p_T
801 electron is rejected, as it is more likely to be a fake electron
- 802 - when a muon and electron share a track the muon is rejected if it is a
803 calo-muon, otherwise the electron is rejected
- 804 - when $\Delta R < 0.2$ for an electron and jet, the jet is rejected to maximize signal
805 acceptance
- 806 - when $\Delta R > 0.2$ for an electron and jet, the electron is rejected as likely
807 originated from decays within the jet
- 808 - when $\Delta R < \min(0.4, 0.04 + 10\text{GeV}/p_T^\mu)$ the muon is rejected, again maximiz-
809 ing signal acceptance, otherwise the jet is rejected
- 810 - when $\Delta R < 1.0$ for the a large-R jet and electron, the jet is rejected

811 **Chapter 7**

812 **Event Selection and**

813 **Categorization**

814 **7.1 Pre-selection**

815 Before applying topological cuts to suppress backgrounds and reduce data
816 size in this search, preselection cuts are applied which include trigger and event
817 requirements. Events must contain exactly one tight lepton (no additional loose
818 leptons), the $p_T^{\ell\nu} > 75$ GeV, and there must be at least two small-R jets or one
819 large-R jet.

820 **7.2 Trigger**

821 The data were collected using the lowest unprescaled single-lepton or E_T^{miss}
822 triggers, as summarized in Table ???. Since the muon term is not considered in the
823 trigger E_T^{miss} calculation, the E_T^{miss} trigger is fully efficient to events with high- p_T
824 muons. For this reason, the E_T^{miss} trigger is used for events where $p_T^\mu > 150$ GeV, to
825 compensate for the poor efficiency of the single muon trigger above $p_T^\mu > 150$ GeV.

Table 7.1: The list of triggers used in the analysis.

Data-taking period	$e\nu qq$ channel	$\mu\nu qq$ ($p_T(\mu\nu) < 150$ GeV) channel	$\mu\nu qq$ ($p_T(\mu\nu) > 150$ GeV) channel
2015	HLT_e24_lhmedium_L1EM20 OR HLT_e60_lhmedium OR HLT_e120_lhloose	HLT_mu20_iloose_L1MU15 OR HLT_mu50	HLT_xe70
2016a (run < 302919) $(L < 1.0 \times 10^{34} \text{ cm}^{-2} \text{ s}^{-1})$	HLT_e26_lhtight_nod0_ivarloose OR HLT_e60_lhmedium_nod0 OR HLT_e140_lhloose_nod0 HLT_e300_etcut	HLT_mu26_ivarmedium OR HLT_mu50	HLT_xe90_mht_L1XE50
2016b (run ≥ 302919) $(L < 1.7 \times 10^{34} \text{ cm}^{-2} \text{ s}^{-1})$	same as above	same as above	HLT_xe110_mht_L1XE50
2017	same as above	same as above	HLT_xe110_pufit_L1XE55
2018	same as above	same as above	HLT_xe110_pufit_xe70_L1XE50

826 **7.3 GGF/VBF RNN**

827 To classify events as originating from GGF/DY or VBF production a recursive
828 neural network (RNN [17]) is used. This approach is more powerful than a cut-
829 based classification as it improves signal efficiency and analysis sensitivity by
830 exploiting correlations between variables that the RNN learns. In particular, a
831 RNN architecture is ideal as it can handle variable numbers of jets in the events.

832 The RNN uses the four-momentum of candidate VBF jets to classify events
833 as VBF or GGF topologies. As sometimes jets will be incorrectly reconstructed
834 the number of jets in the event are expected to vary across the inputs samples.
835 VBF candidate jets are identified by removing jets from the event that are likely
836 from $W/Z \rightarrow qq$. For the resolved regime this means removing the two leading
837 small-R jets from the VBF candidate jet list. For the merged regime this means
838 removing small-R jets separated by less than 1.0 in dR from the large-R jet. VBF
839 candidate jets are also required to be within $|\eta| < 4.5$. From the list of remaining
840 VBF candidate jets, the two highest- p_T jets are chosen.

841 The architecture of the RNN is show in Figure 7.1. LSTMs are a type of
842 RNN that extract meaningful information and can retain it (unlike other neural
843 networks architectures). This is useful for VBF event classification for events with
844 two jets, where using the kinematic properties of both jets (and their correlations)
845 will lead to more efficient event classification.

846 In this RNN architecture, the VBF candidates are first passed to a masking
847 layer which checks the number of jets in the event. If there is only one jet, only one
848 LSTM layer is used. The output of masking is then passed to a Long Short-Term
849 Memory (LSTM) cell, with a tanh activation function. This output is passed to
850 a dropout layer, that has a probability of 0.3 to completely forget the output of
851 the LSTM. Dropout is a regularization method, that prevents over-fitting. The

852 output of the dropout layer is then passed to the second LSTM and then through
853 another dropout layer with a probability of 0.3.

854 The weights and other parameters of the network are learned by training the
855 network with VBF and GGF signals over 200 epochs with an Adam Optimizer
856 [natasha add reference]. The training is truncated if the network parameters are
857 unchanged after ten iterations. The training, testing and validation sets are 56,
858 30, and 14 percent of the input samples, respectively. Figure [add INT figure
859 32] shows the loss function of the network as a function of training epochs. The
860 validation test set has a smaller loss function as dropout was not applied. Figure
861 7.3 shows the ROC curve for the RNN using k-fold cross validation.

862 Finally this output is passed to a dense layer [natasha ask antonio about this]
863 and then to a sigmoid activation layer, leading to an overall RNN score. Figure 7.2
864 shows the RNN discriminant for backgrounds, GGF signals, and VBF signals. The
865 RNN score is ~ 0 for GGF and background processes and ~ 1 for VBF processes.
866 Figure 7.4 shows the limits for various signal processes based on the RNN cut
867 applied. Requiring the RNN score to be > 0.8 was chosen as it provided the best
868 significance (and signal efficiency) across for this final state and the $\nu\nu qq$ and $\ell\ell qq$
869 channels this channel will be combined with for future publications.

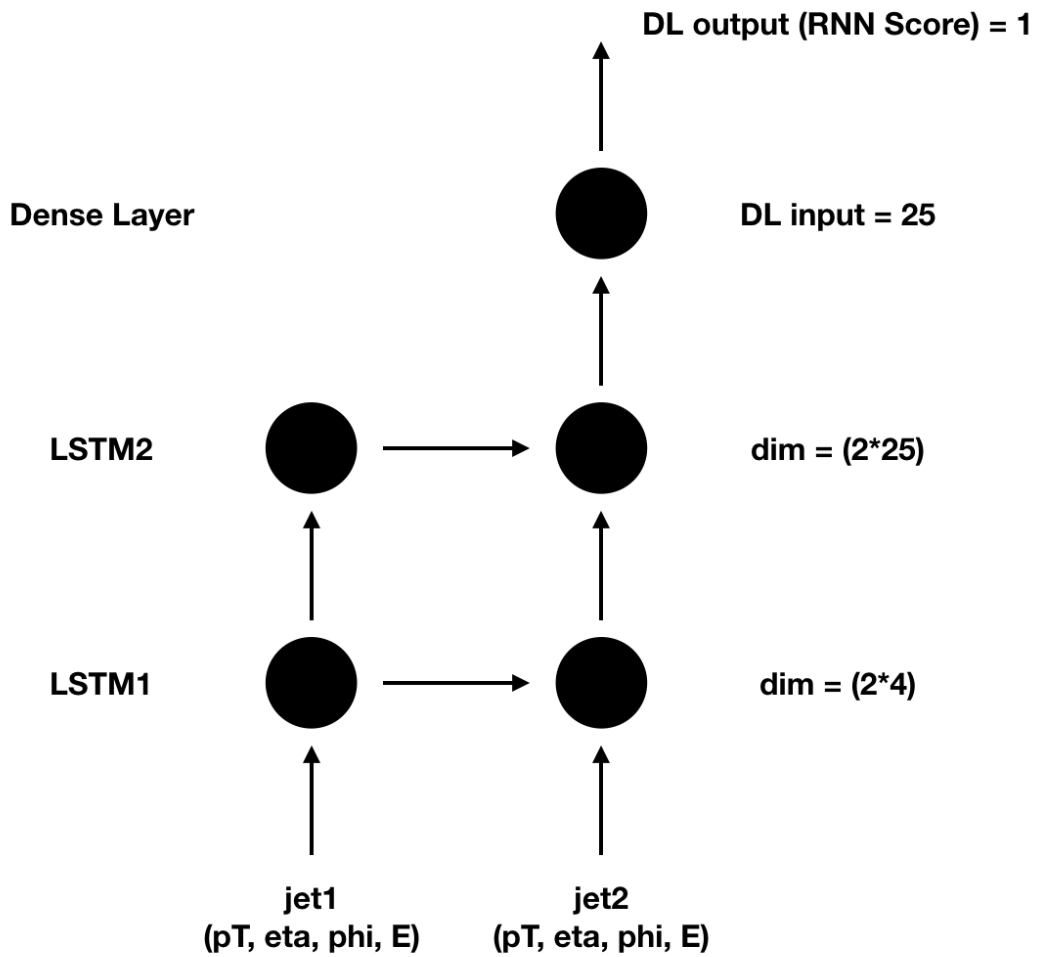


Figure 7.1: RNN architecture. Natasha add caption

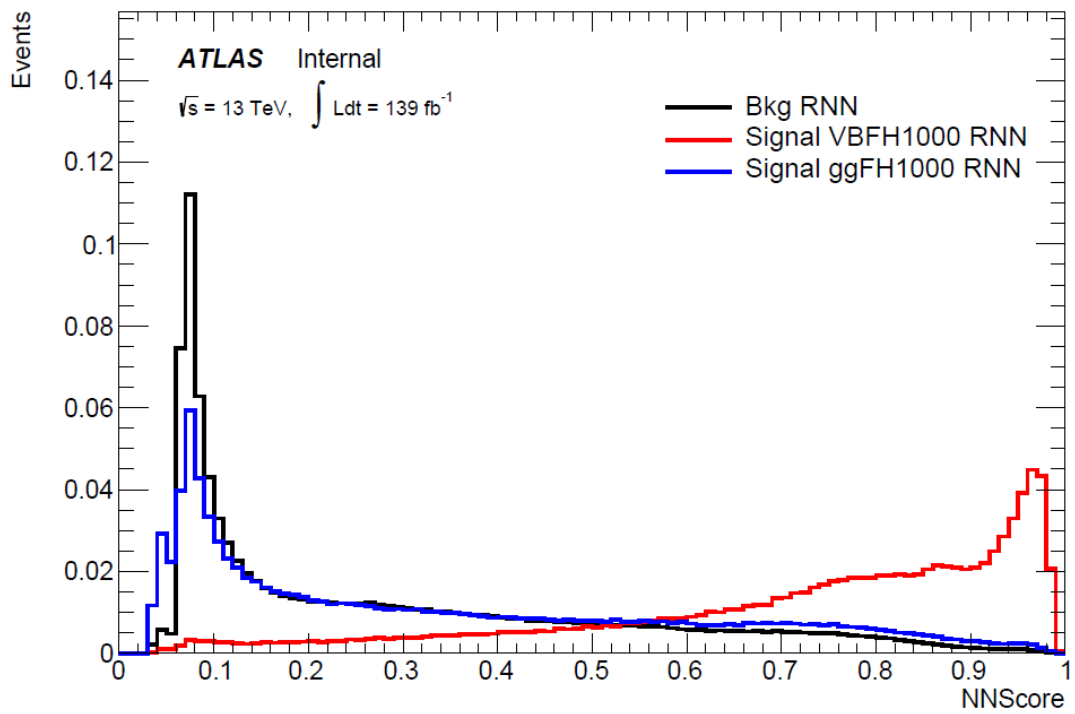


Figure 7.2: RNN Score distribution for ggF and VBF signals and backgrounds.

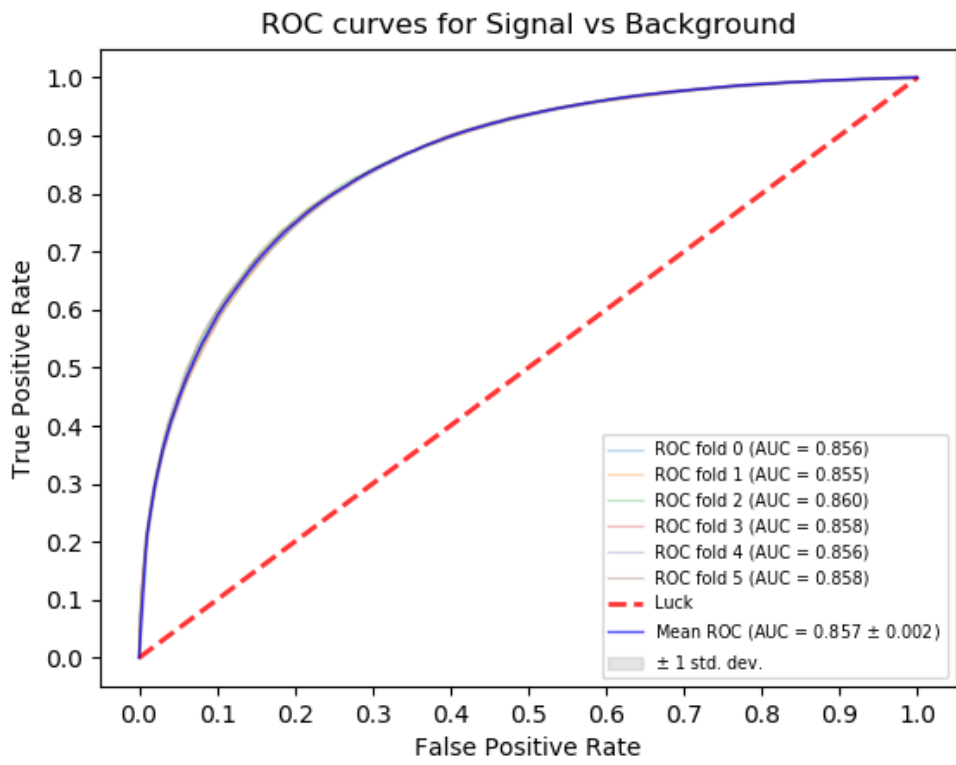


Figure 7.3: ROC curve using k-fold validation for RNN.

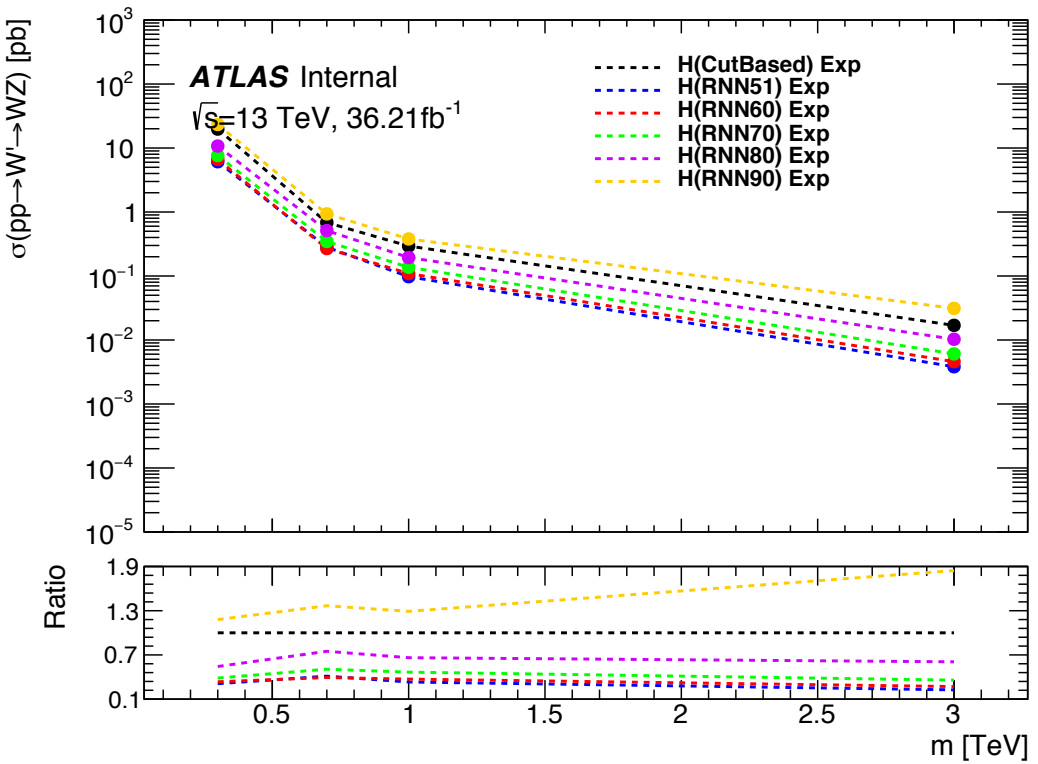


Figure 7.4: Comparison of GGF Z' limits for different RNN score selections. The bottom panel shows the ratio of the upper limits set for different RNN cuts to the cut-based analysis. In this panel smaller numbers, indicate that the expected upper limit is smaller than the cut-based analysis, which is desired.

870 7.4 Topological Cuts

871 Once an event is classified as VBF or GGF via the RNN, it must pass other
 872 topological cuts that maximize S/\sqrt{B} . First, to efficiently select events with a
 873 $W \rightarrow \ell\nu$ candidate exactly one tight lepton is required and $E_T^{miss} > 100(60)$
 874 GeV and $p_{T,\ell\nu} > 200(75)$ GeV in the merged (resolved) analysis to suppress the
 875 multi-jet background.

876 For the merged analysis, in addition to the $W \rightarrow \ell\nu$ and $W/Z \rightarrow J$ selections
 877 above, the $\min(p_{T,\ell\nu}, p_{T,J})/m_{WV} > 0.35(0.25)$ for the GGF (VBF) category. To
 878 reduce $t\bar{t}$ contamination events with the signal region and $W+jets$ control region

879 events with at least one b jet with $\Delta R > 1.0$ from the large-R jet are excluded.
 880 High purity signal regions require the D_2 and W/Z mass window cut to be passed,
 881 whereas the low purity region only requires the W/Z mass window cut to be
 882 passed. Finally for events to be classified as tagged the large-R jet must contain
 883 exactly two b-tagged jets. Untagged events must have no more than one b-tagged
 884 jet matched to the large-R jet. These selections are shown in Table 7.2. The
 885 distributions for the variables used in merged analysis for top control regions are
 886 shown in Figure 7.6-7.9.

887 Events failing the merged selection are then re-analyzed in the resolved cat-
 888 egory. To enhance resolved signals, the event should contain two high- p_T boson
 889 candidates that are back-to-back in the ϕ as shown by the cuts in Table 18. Again
 890 to suppress the $t\bar{t}$ background in the WCR and SR events are required to have no
 891 additional b-jets.

892 The WV system mass, m_{WV} is reconstructed from the lepton, neutrino, and
 893 hadronically-decaying boson candidate. The momentum of the neutrino along the
 894 z -direction is obtained by constraining the W boson mass of the lepton neutrino
 895 system to be $80.3 \text{ GeV}/c^2$. For complex solutions to this constraint, p_Z is taken
 896 as either the real component of the solution or the one with the smaller absolute
 897 value of the two real solutions. For the resolved analysis, m_{WV} is reconstructed
 898 by constraining the $W(Z)$ dijet system:

$$p_{T,jj}^{corr} = p_{T,jj} \times \frac{m_{W/Z}}{m_{jj}} \quad (7.1)$$

899

$$m_{jj}^{corr} = m_{W/Z} \quad (7.2)$$

900 where m_{jj} and $m_{W/Z}$ are the reconstructed invariant mass of the hadronically-
 901 decaying W/Z boson and the PDG values of the W/Z boson masses, respectively.

Table 7.2: Summary of selection criteria used to define the signal region (SR), W +jets control region (W CR) and $t\bar{t}$ control region ($t\bar{t}$ CR) for merged 1-lepton channel.

Selection		SR		W CR (WR)		$t\bar{t}$ CR (TR1)	
		HP	LP	HP	LP	HP	LP
$W \rightarrow \ell\nu$	Num of Tight leptons	1					
	Num of Loose leptons	0					
	E_T^{miss}	$> 100 \text{ GeV}$					
	$p_T(\ell\nu)$	$> 200 \text{ GeV}$					
$W/Z \rightarrow J$	Num of large- R jets	≥ 1					
	D_2 cut	pass	fail	pass	fail	pass	fail
	W/Z mass window cut	pass	pass	fail	fail	pass	pass
	Numb. of associated VR track jets b -tagged	For $Z \rightarrow J$: ≤ 1 ($= 2$) for untagged (tagged) category					
	$\min(p_{T,\ell\nu}, p_{T,J}) / m_{WV}$	$> 0.35(0.25)$ for DY/ggF (VBF) category					
	Top-quark veto	Num of b -tagged jets outside of large- R jet	0			≥ 1	
Pass VBF selection			no (yes) for DY/ggF (VBF) category				

902 A summary of the resolved selections is shown in Table 7.3. The distributions for
903 the variables used in the resolved analysis in the TCR are shown in Figure 7.10,
904 7.11.

905 The analysis cutflow is shows in Figure 7.5. Events classified as VBF events
906 are classified as Merged High purity, low purity or resolved signal region selections
907 sequentially. If the event does not pass any of these selections but passes a VBF
908 control region selection it is classified as a VBF CR event. If the event fails the
909 VBF selection it is then checked if it passes the Merged High purity, Low purity
910 or resolved signal region selections (NB: for the WZ decay modes all the regions
911 have tagged and untagged categories). If the event fails all the GGF signal region
912 selections, it is then kept for GGF control region selections, if it passes those
913 selections.

Table 7.3: The list of selection cuts in the resolved analysis for the WW and WZ signal regions (SR), $W+\text{jets}$ control region (WR) and $t\bar{t}$ control region (TR).

cuts	SR	W CR (WR)	$t\bar{t}$ CR (TR1)
$W \rightarrow \ell\nu$	Number of Tight leptons	1	
	Number of Loose leptons	0	
	E_T^{miss}	$> 60 \text{ GeV}$	
	$\cancel{p}_T(\ell\nu)$	$> 75 \text{ GeV}$	
$W/Z \rightarrow jj$	Number of small-R jets	≥ 2	
	Leading jet p_T	$> 60 \text{ GeV}$	
	Subleading jet p_T	$> 45 \text{ GeV}$	
	$Z \rightarrow q\bar{q}$ $W \rightarrow q\bar{q}$	$78 < m_{jj} < 105 \text{ GeV}$ $68 < m_{jj} < 98 \text{ GeV}$	$50 < m_{jj} < 68 \text{ GeV}$ or $105 < m_{jj} < 150 \text{ GeV}$
Topology cuts	Num. of b -tagged jets	For $Z \rightarrow jj$: ≤ 1 ($= 2$) for untagged (tagged) category	
	$\Delta\phi(j, \ell)$	> 1.0	
	$\Delta\phi(j, E_T^{\text{miss}})$	> 1.0	
	$\Delta\phi(j, j)$	< 1.5	
	$\Delta\phi(\ell, E_T^{\text{miss}})$	< 1.5	
Topo veto	$\min(p_{T,\ell\nu}, p_{T,jj}) / m_{WW}$	$> 0.35(0.25)$ for DY/ggF (VBF) category	
	Number of additional b -tagged jets	0	≥ 1
Pass VBF selection		no (yes) for DY/ggF (VBF) category	

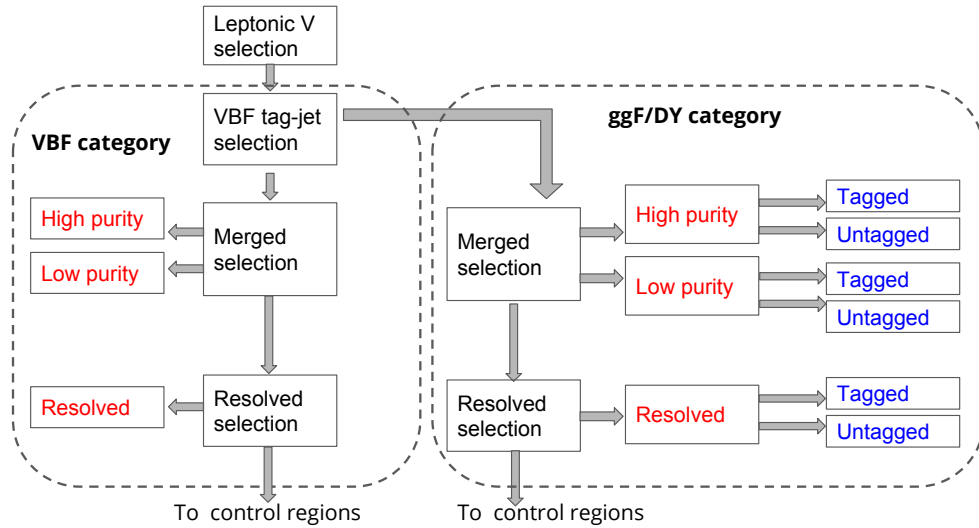


Figure 7.5: Event Categorization. Natasha write more.

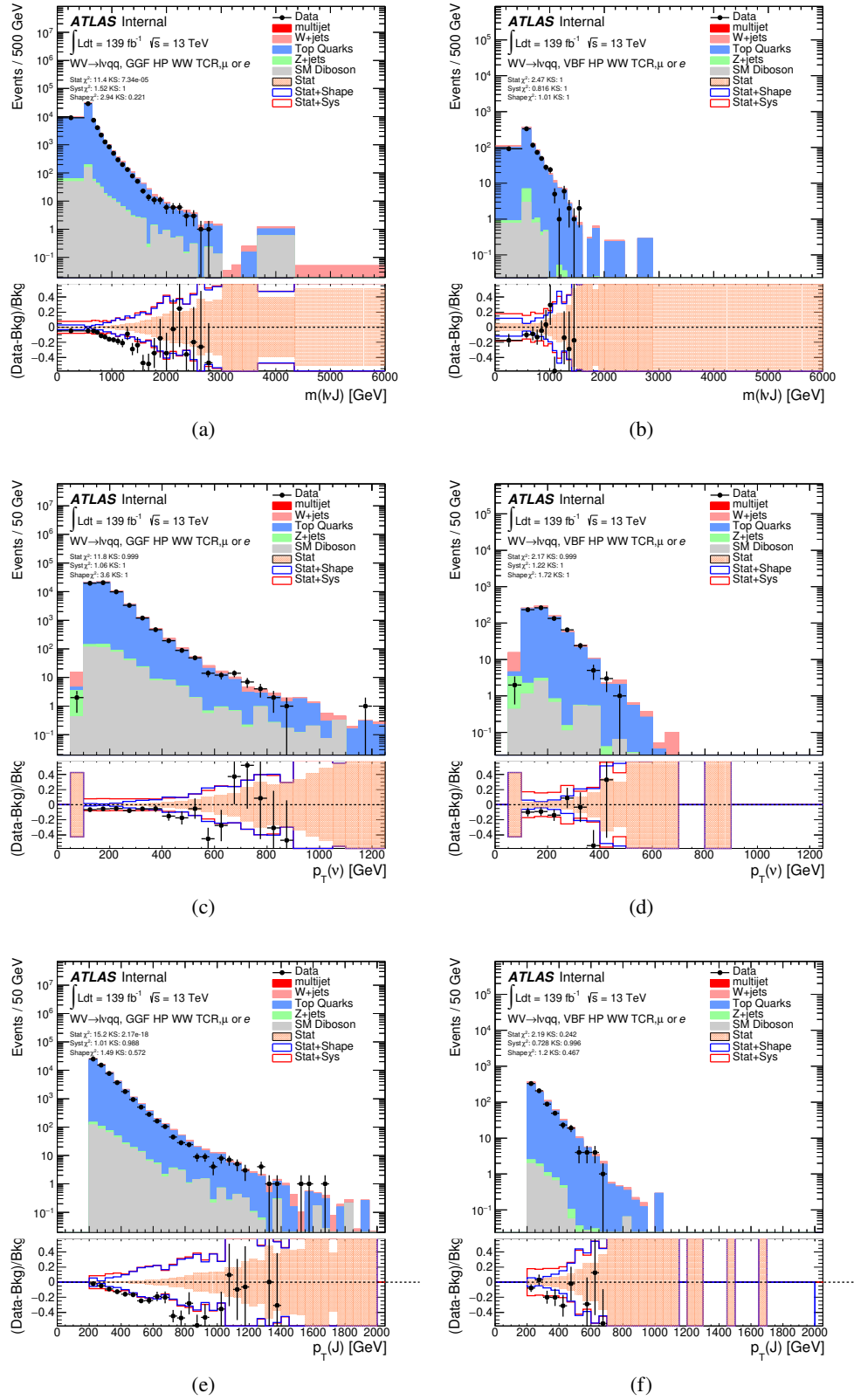


Figure 7.6: Data MC comparison for the merged WW HP TCR. The bottom panel shows the ratio of the difference between data and simulation to simulation. The red bands include the all systematic and statistical uncertainties on the background.

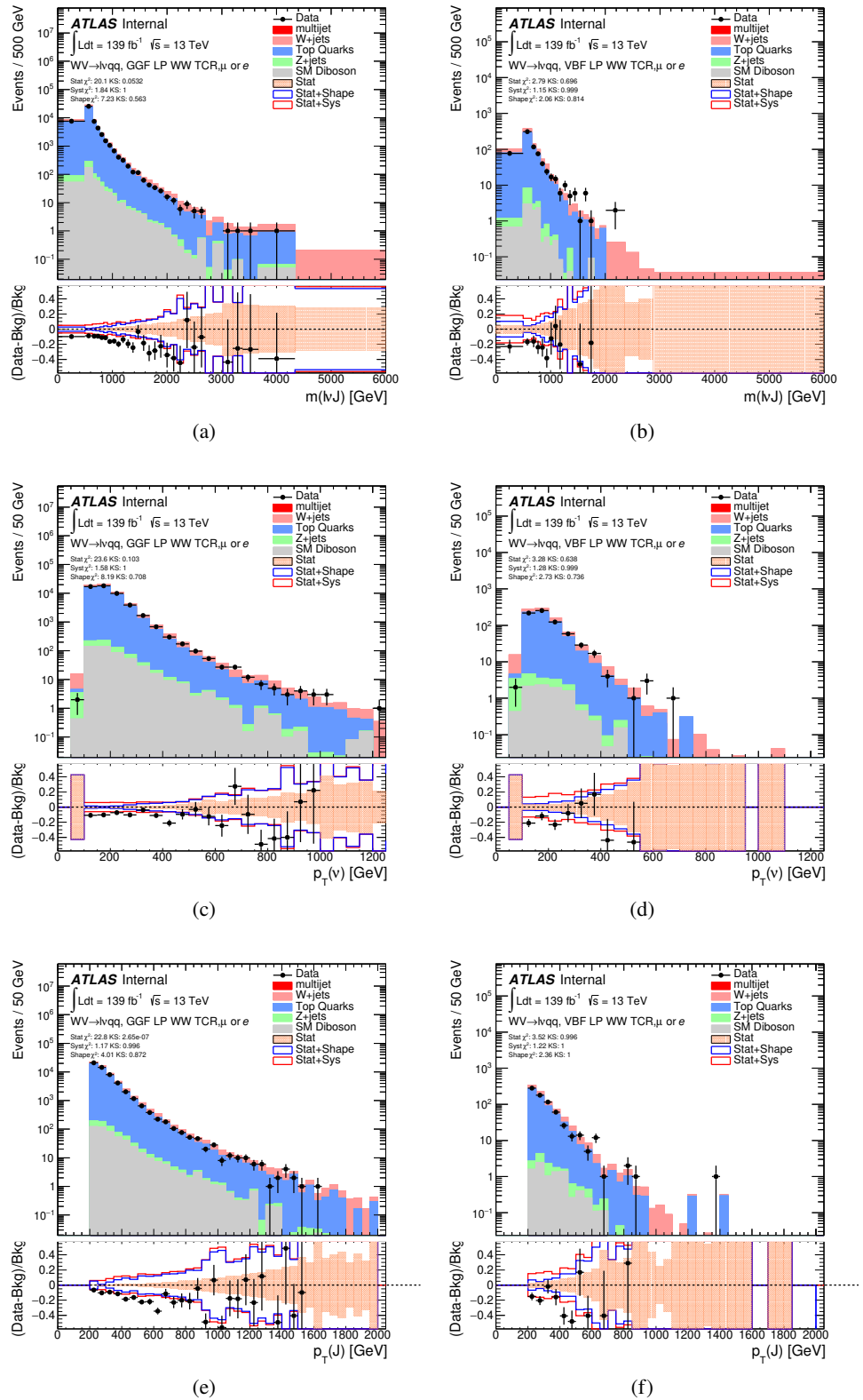


Figure 7.7: Data MC comparison for the merged WW LP TCR. The bottom panel shows the ratio of the difference between data and simulation to simulation. The red bands include the all systematic and statistical uncertainties on the background.⁸³

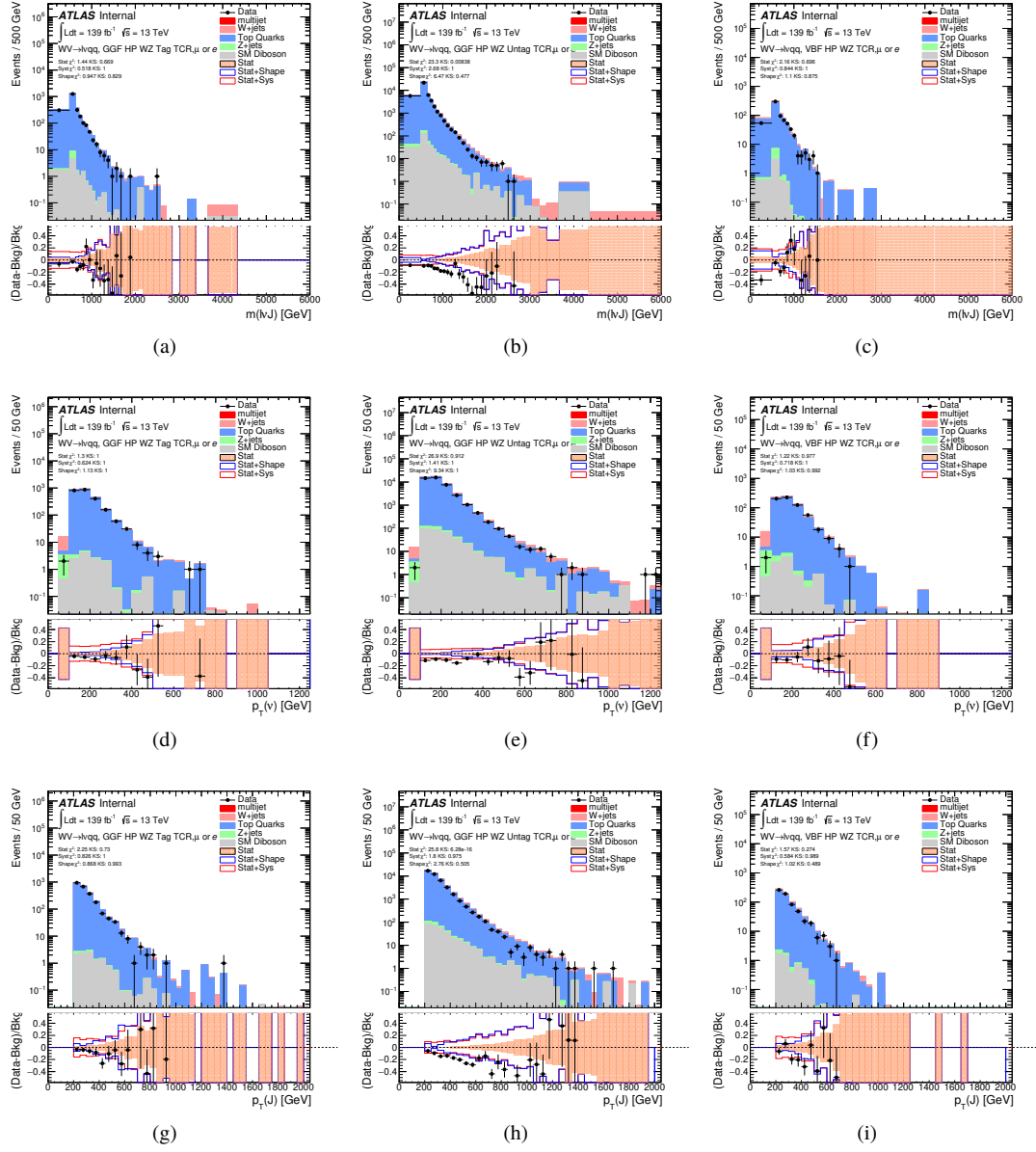


Figure 7.8: Data MC comparison for the merged WZ HP TCR. The bottom panel shows the ratio of the difference between data and simulation to simulation. The red bands include the all systematic and statistical uncertainties on the background.

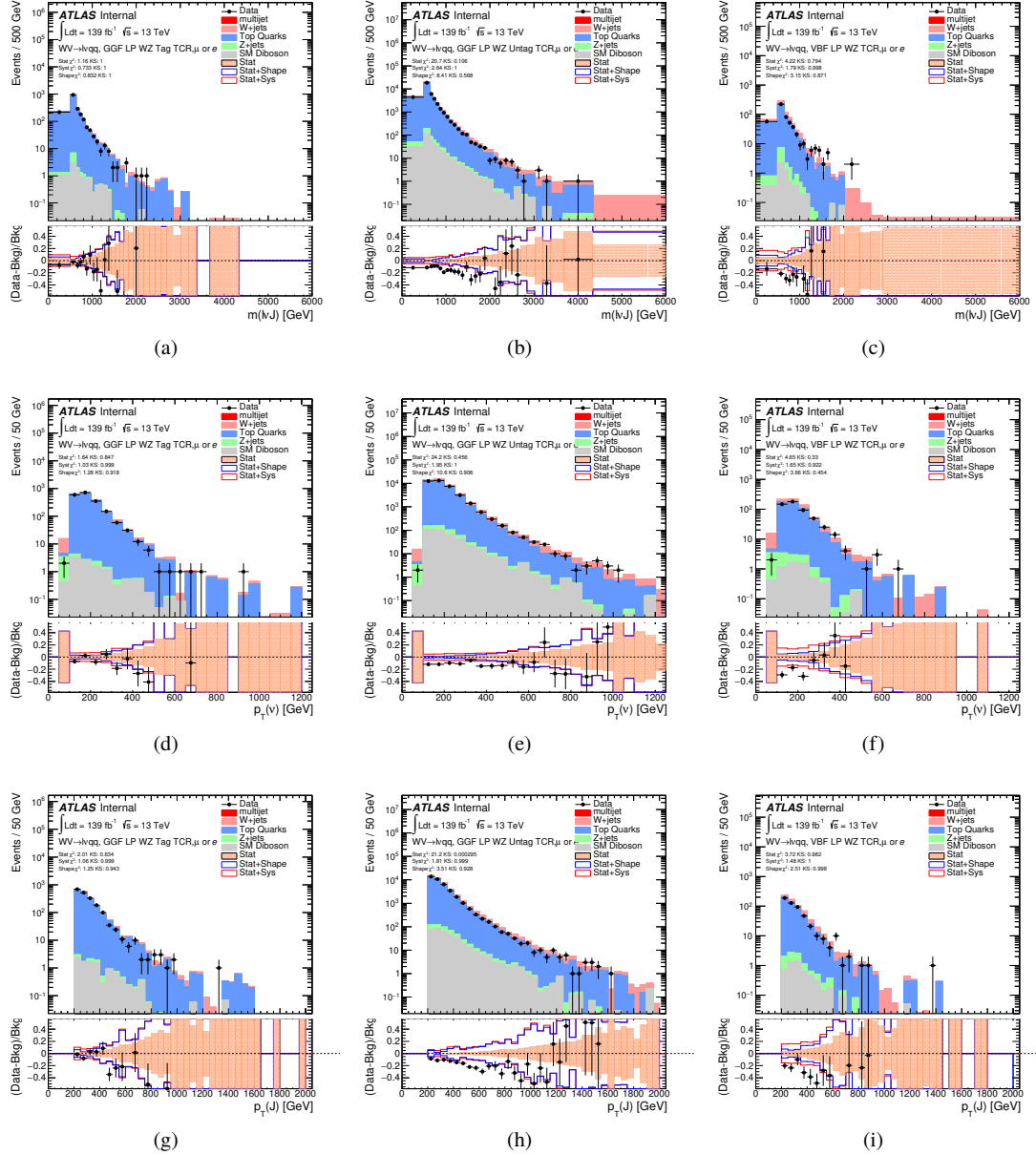


Figure 7.9: Data MC comparison for the merged WZ LP TCR. The bottom panel shows the ratio of the difference between data and simulation to simulation. The red bands include the all systematic and statistical uncertainties on the background.

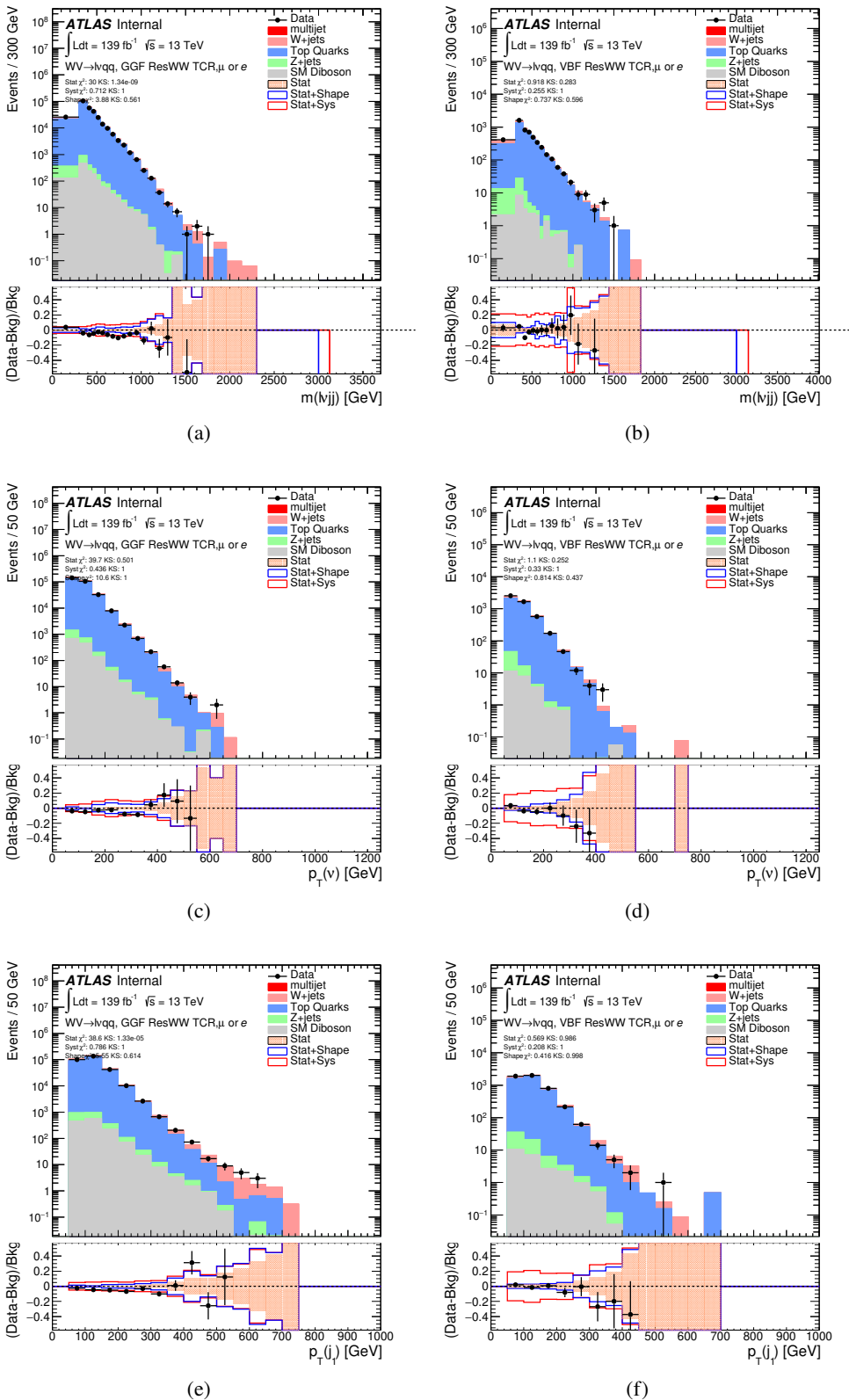


Figure 7.10: Data MC comparison for the resolved WW TCR. The bottom panel shows the ratio of the difference between data and simulation to simulation. The red bands include the all systematic and statistical uncertainties on the background.⁸⁶

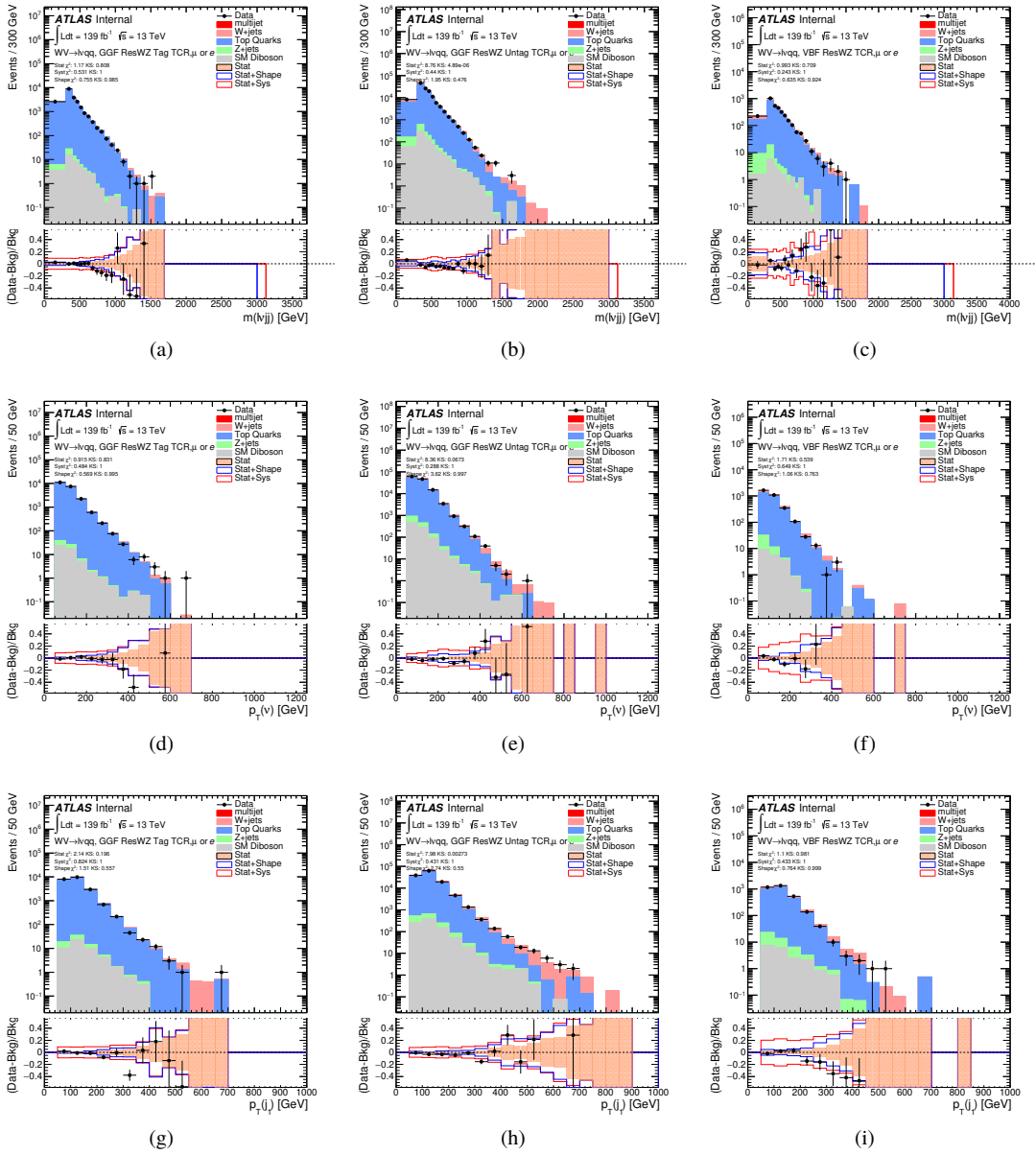


Figure 7.11: Data MC comparison for the resolved WZ TCR. The bottom panel shows the ratio of the difference between data and simulation to simulation. The red bands include the all systematic and statistical uncertainties on the background.

914 **7.5 Selection Acceptance times efficiency for Sig-**
 915 **nal Events**

916 The acceptance times efficiency for the signal region selection is defined as:

$$A \cdot \epsilon = \frac{N_{\text{events selected}}^{\text{truth}}}{N_{\text{events generated}}^{\text{truth}}} \cdot \frac{N_{\text{events selected}}^{\text{reco}}}{N_{\text{events selected}}^{\text{truth}}} = \frac{N_{\text{events selected}}^{\text{reco}}}{N_{\text{events generated}}^{\text{truth}}} \quad (7.3)$$

917 The distributions of $A \cdot \epsilon$ as a function of the resonance mass for the different spin
 918 models are shown in Figures 7.13 - ??.

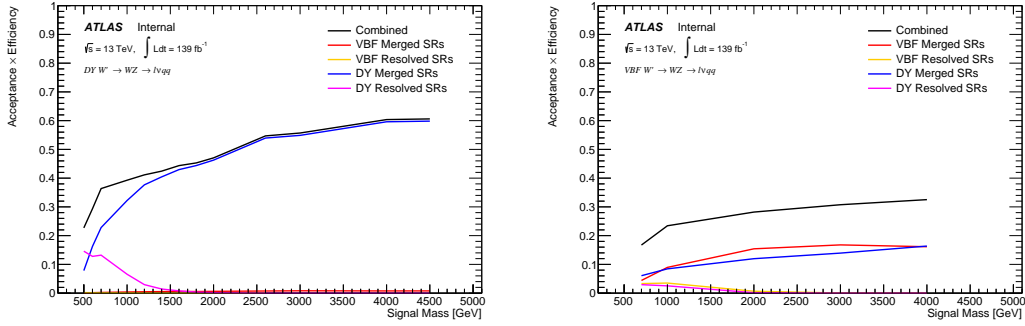


Figure 7.12: Selection acceptance times efficiency for the $W' \rightarrow WZ \rightarrow \ell\nu qq$ events from MC simulations as a function of the W' mass for (a) Drell-Yan and (b) VBF production, combining the merged HP and LP signal regions of the $WW \rightarrow \ell\nu J$ selection and the resolved regions of the $WW \rightarrow \ell\nu jj$ selection.

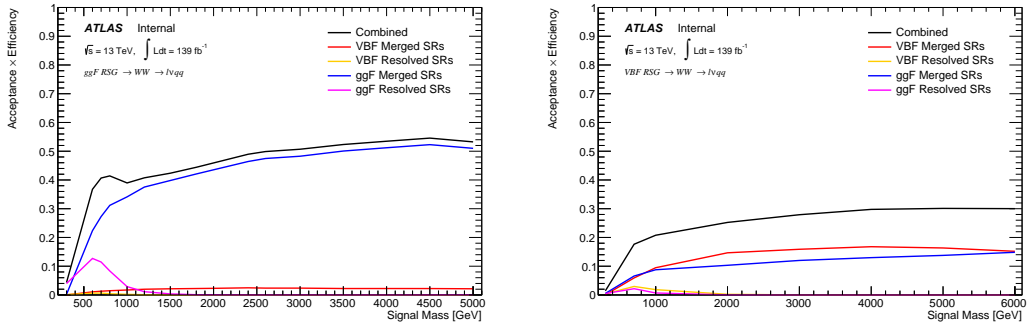


Figure 7.13: Selection acceptance times efficiency for the $G \rightarrow WW \rightarrow \ell\nu qq$ events from MC simulations as a function of the G mass for (a) Drell-Yan and (b) VBF production, combining the merged HP and LP signal regions of the $WW \rightarrow \ell\nu J$ selection and the resolved regions of the $WW \rightarrow \ell\nu jj$ selection.

919 7.6 Background Estimate

920 7.6.1 Control Regions

921 To more accurately model the two dominant backgrounds in this analysis,
 922 $W+jets$ and $t\bar{t}$, control regions are constructed for each. These control regions
 923 are dominated by these processes and used to extract normalization factors in
 924 the final likelihood fit that are then used in the signal region estimates. For the
 925 $t\bar{t}$ control region the event must contain at least one such b jet. The WCR is
 926 constructed using the $m_{jj/J}$ mass window sidebands. All other backgrounds are
 927 estimated using simulation, except fake lepton backgrounds, which are derived
 928 using a data-driven method.

929 7.6.2 Fake Lepton Backgrounds

930 Backgrounds in this analysis containing real leptons (e.g. $W/Z+jets$, diboson,
 931 $t\bar{t}$, single- t) are well-modeled with simulated samples and constrained with data
 932 from CRs. However, the fake lepton background (also referred to as the multijet
 933 background) is not well-modeled with simulation. For this reason, the multijet

background is extracted from data. Heavy flavor decay products, jets, and converted photons can be mistakenly reconstructed as electrons. Fake electrons often arise from jet fakes while non-prompt muons usually arise from heavy flavor decay. For this analysis, these fake electrons generally fail the electron ID criteria and fake muons fail the muon isolation requirement. Therefore, to derive the multijet template shape the SR and CR selections and inverted lepton requirements are used as seen in Table 7.4. NB: by inverting the lepton isolation/identification criteria the SRs and CRs are orthogonal.

The template shape of the MJ background is determined by using a multijet validation region (MJVR) that requires the inverted lepton isolation/identification requirement and the two signal jets to satisfy the m_{jj} requirement used in the $W+jets$ CRs. The E_T^{miss} distribution in MJCR is shown in Figure 7.14 for 2017 data. The template is then extracted by subtracting the data in the MJVR from the electroweak background processes. The resulting template and electroweak backgrounds are then fit to data. In this fit, the E_T^{miss} distribution compared to data to extract electroweak background, multijet electron and muon background normalizations. The fitted scale factors from this MJVR template are then applied in the MJCR template. The electron and muon background normalizations in the MJCR template are parameters in the final simultaneous fit. Technically, there should be a separate template for every CR and SR, but some MJ regions have insufficient statistics to do this. Additionally, the shapes for the MJ templates for VBF and ggF regions are found to be compatible within statistical uncertainty. Therefore, the sample MJ template used for VBF and ggF CR/SRs, but with different pre-MJ-fit scale factors.

This template method was validated using WCR and full Run 2 data. The results of the fit are shown in Table 7.5. The multijet contribution in the muon

960 channel for $p_T^W > 150$ GeV is consistent with zero, and therefore neglected in
 961 the final fit. Applying the extracted normalization factor to MJVR in WCRs for
 962 various kinematic variables such as E_T^{miss} , W transverse mass, lepton p_T , and the
 963 invariant mass as show in Figures 7.15 -7.24. These figures show good agreement
 964 between the data and background estimate.

Table 7.4: Definitions of “inverted” leptons used in multijet control region

	Criterion	signal lepton	inverted lepton
Electron	ID	TightLH	MediumLH !TightLH
	Calo Isolation	FixedCutHighPtCaloOnlyIso	FixedCutHighPtCaloOnlyIso
Muon	ID	WHSignalMuon	WHSignalMuon
	Track Isolation	FixedCutTightTrackOnlyIso	!FixedCutTightTrackOnlyIso $ptvarcone30/pt < 0.07^*$

*Only applied to events with $pTW < 150\text{GeV}$

965

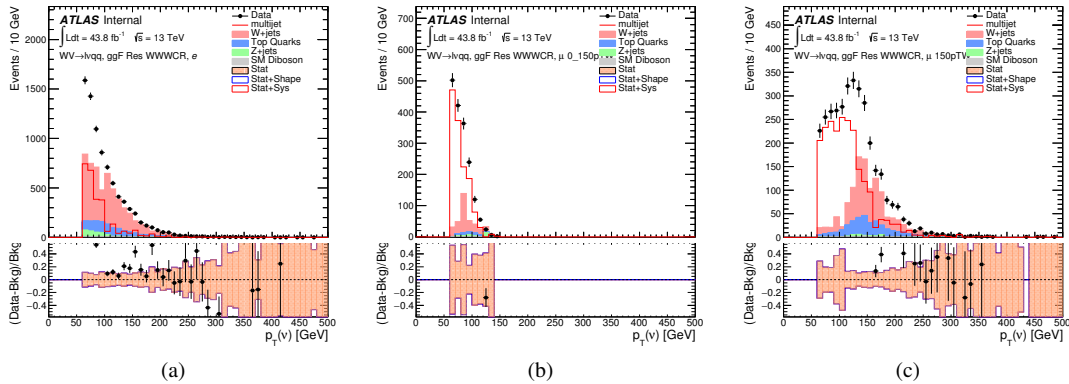


Figure 7.14: The E_T^{miss} distribution in MJCR for 2017 data in the electron channel(left), muon channel with W -boson $pT < 150$ GeV (center) and > 150 GeV (right). Multi-jet templates are calculated as remaining data components after excluding known MC

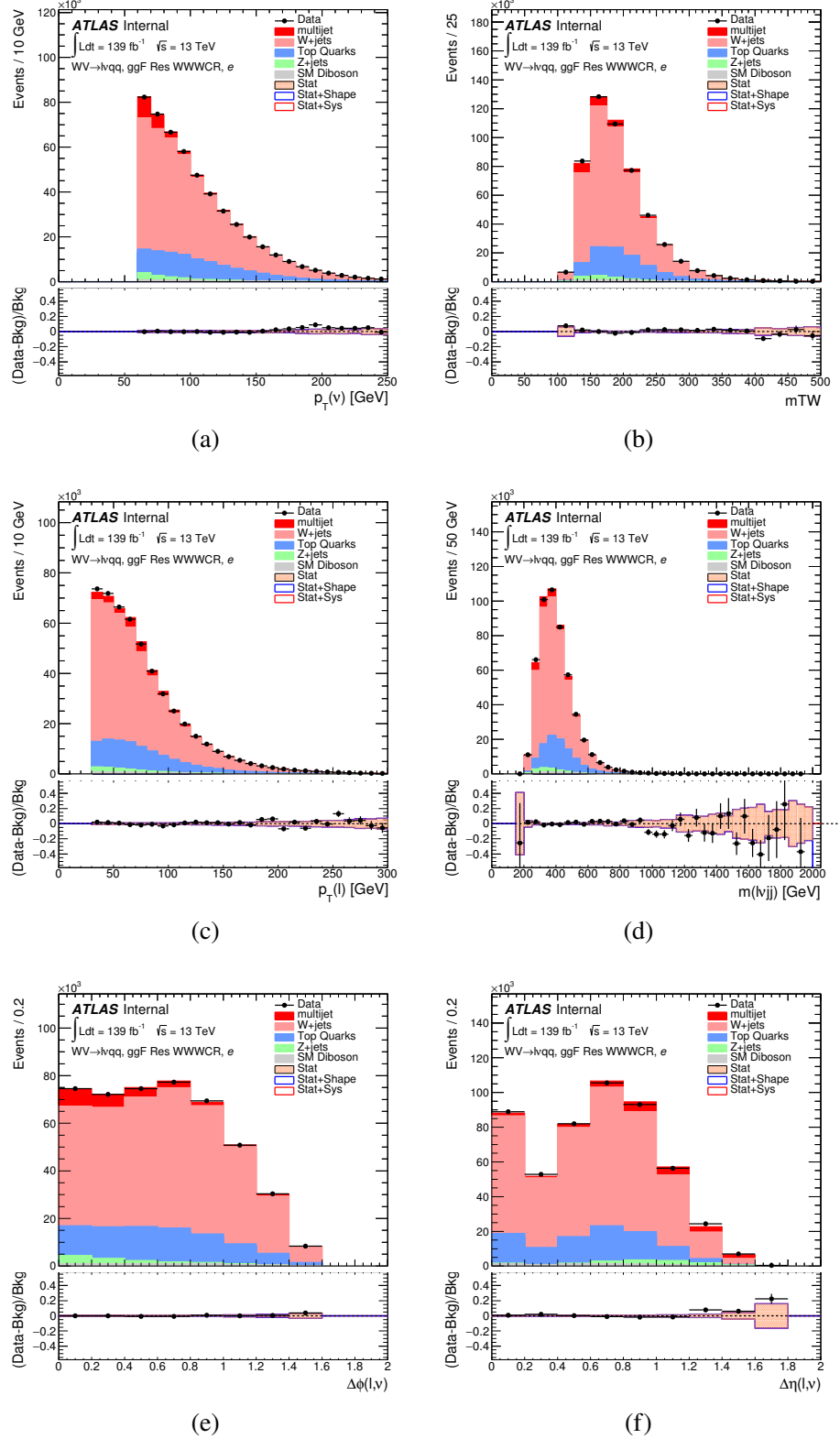


Figure 7.15: Postfit Data/MC comparison of distributions of E_T^{miss} , m_T^W , lepton and neutrino p_T , $m_{l\nu jj}$, lepton- ν angular distance in the WW electron channel. The MJ template is obtained from the pre-MJ-fit.

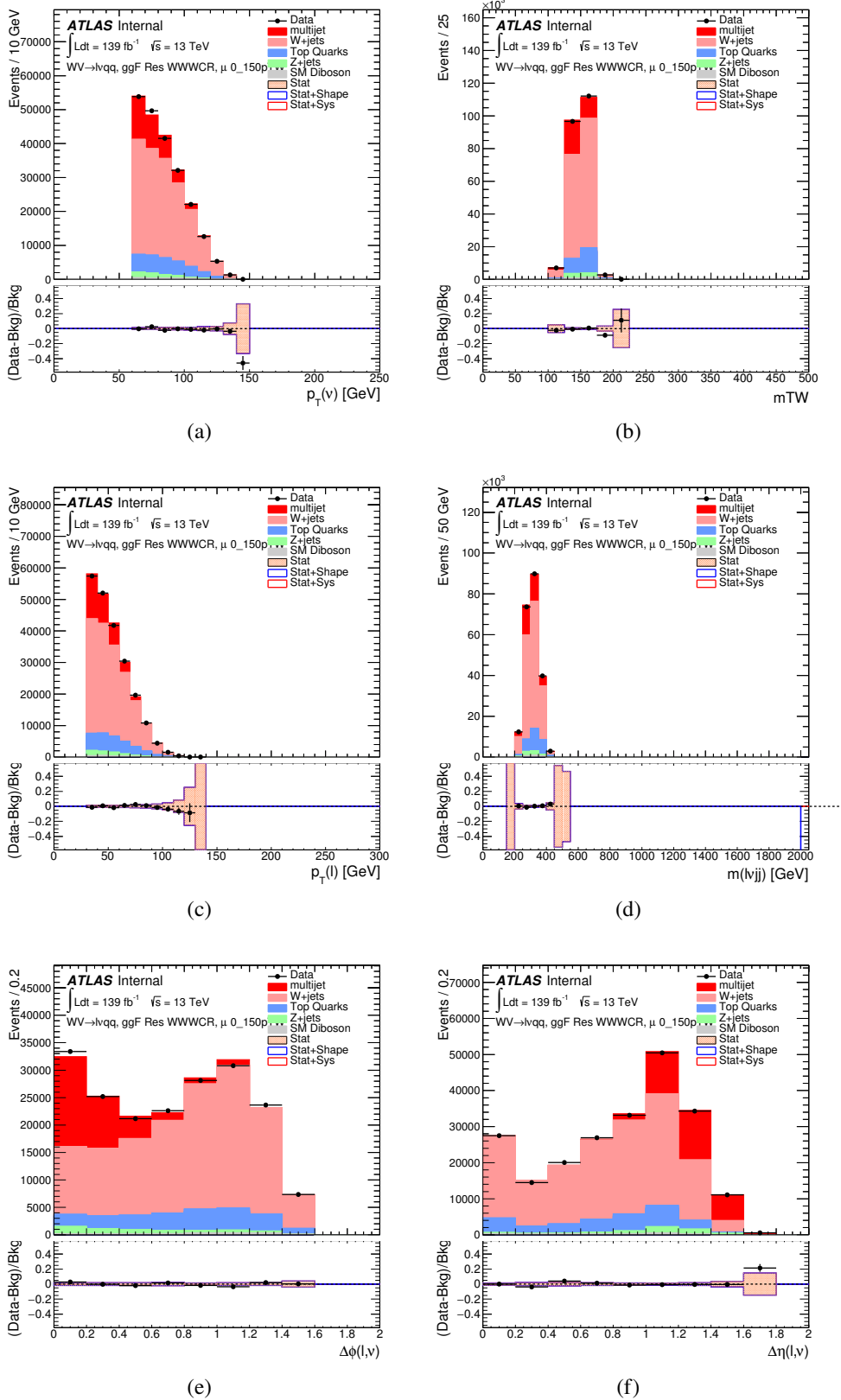


Figure 7.16: Postfit Data/MC comparison of distributions of E_T^{miss} , m_T^W , lepton and neutrino p_T , $m_{l\nu jj}$, lepton- ν angular distance in the WW muon channel. The MJ template is obtained from the pre-MJ-fit.

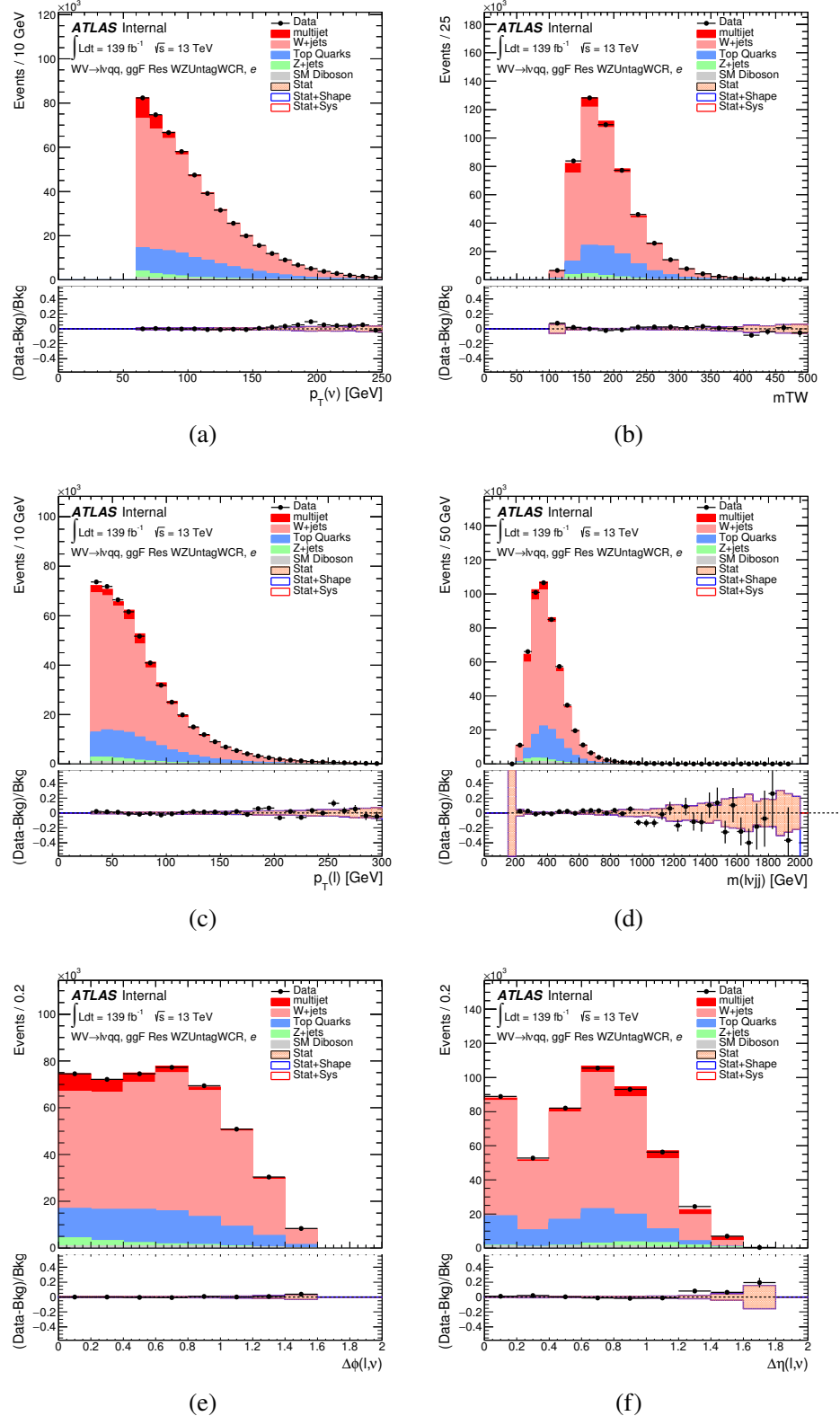


Figure 7.17: Postfit Data/MC comparison of distributions of E_T^{miss} , m_T^W , lepton and neutrino p_T , $m_{l\nu jj}$, lepton- ν angular distance in the WZ untag electron channel. The MJ template is obtained from the pre-MJ-fit.

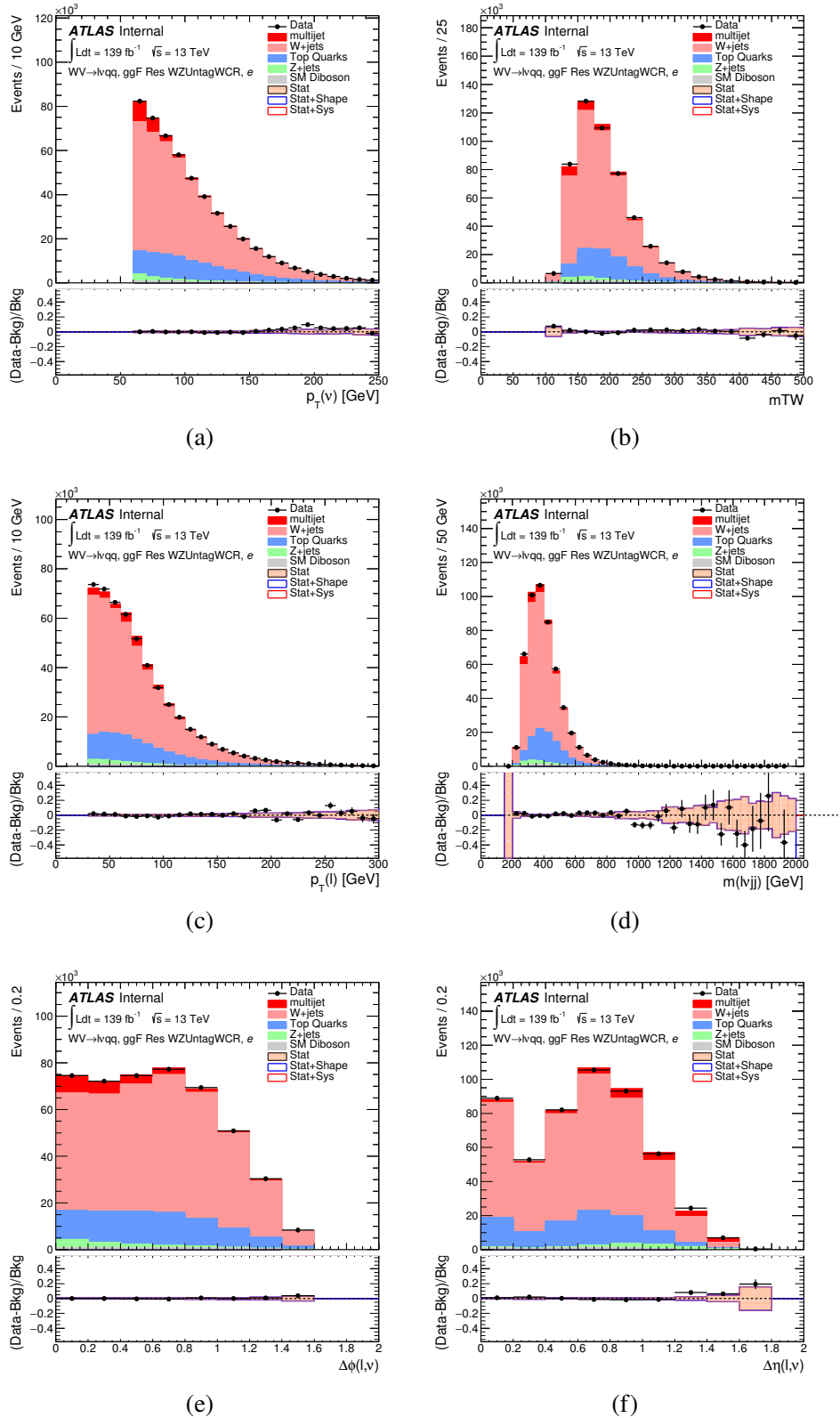


Figure 7.18: Postfit Data/MC comparison of distributions of E_T^{miss} , m_T^W , lepton and neutrino p_T , $m_{\ell\nu jj}$, lepton- ν angular distance in the WZ untag muon channel. The MJ template is obtained from the pre-MJ-fit.

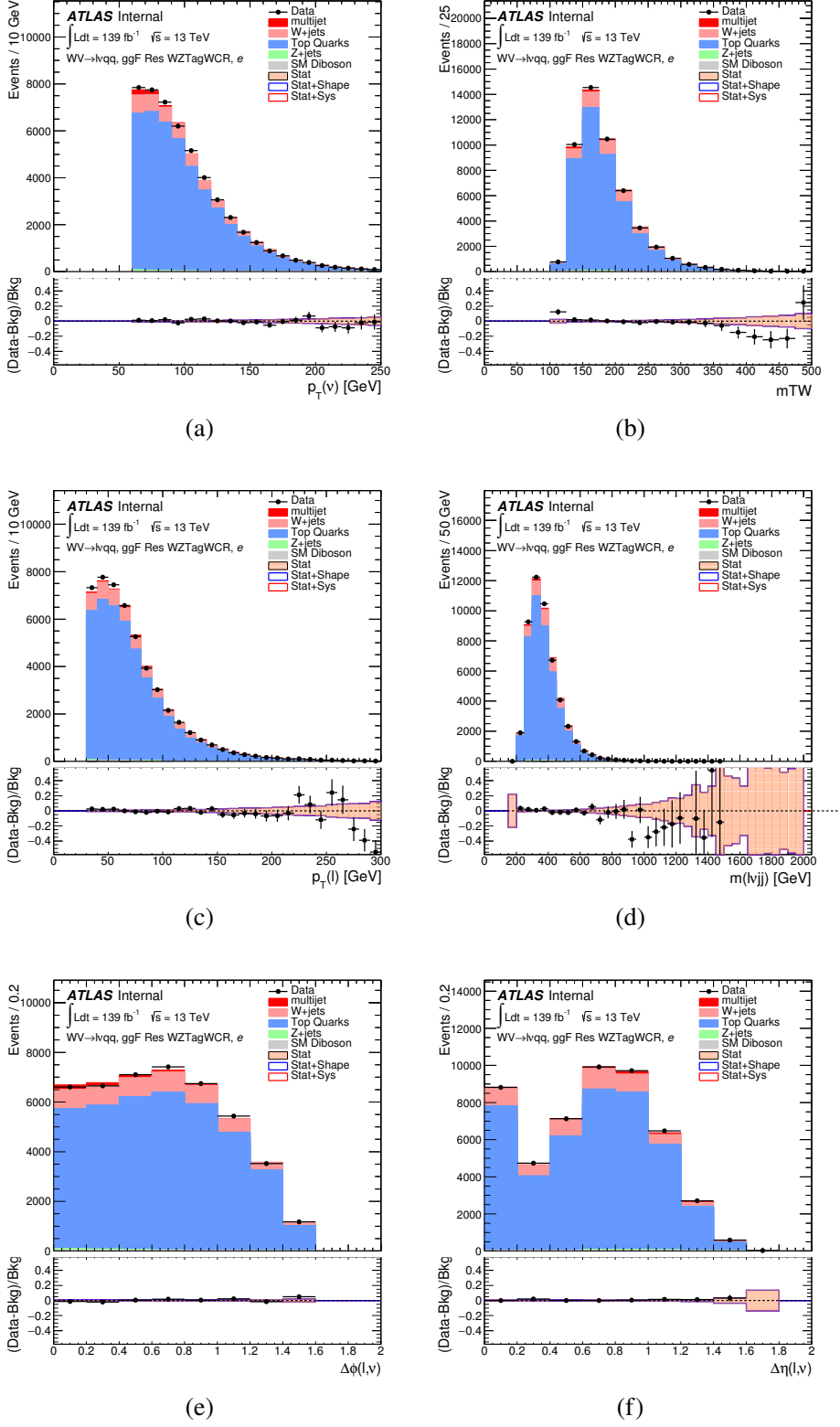


Figure 7.19: Postfit Data/MC comparison of distributions of E_T^{miss} , m_T^W , lepton and neutrino p_T , $m_{l\nu jj}$, lepton- ν angular distance in the WZ untag electron channel. The MJ template is obtained from the pre-MJ-fit.

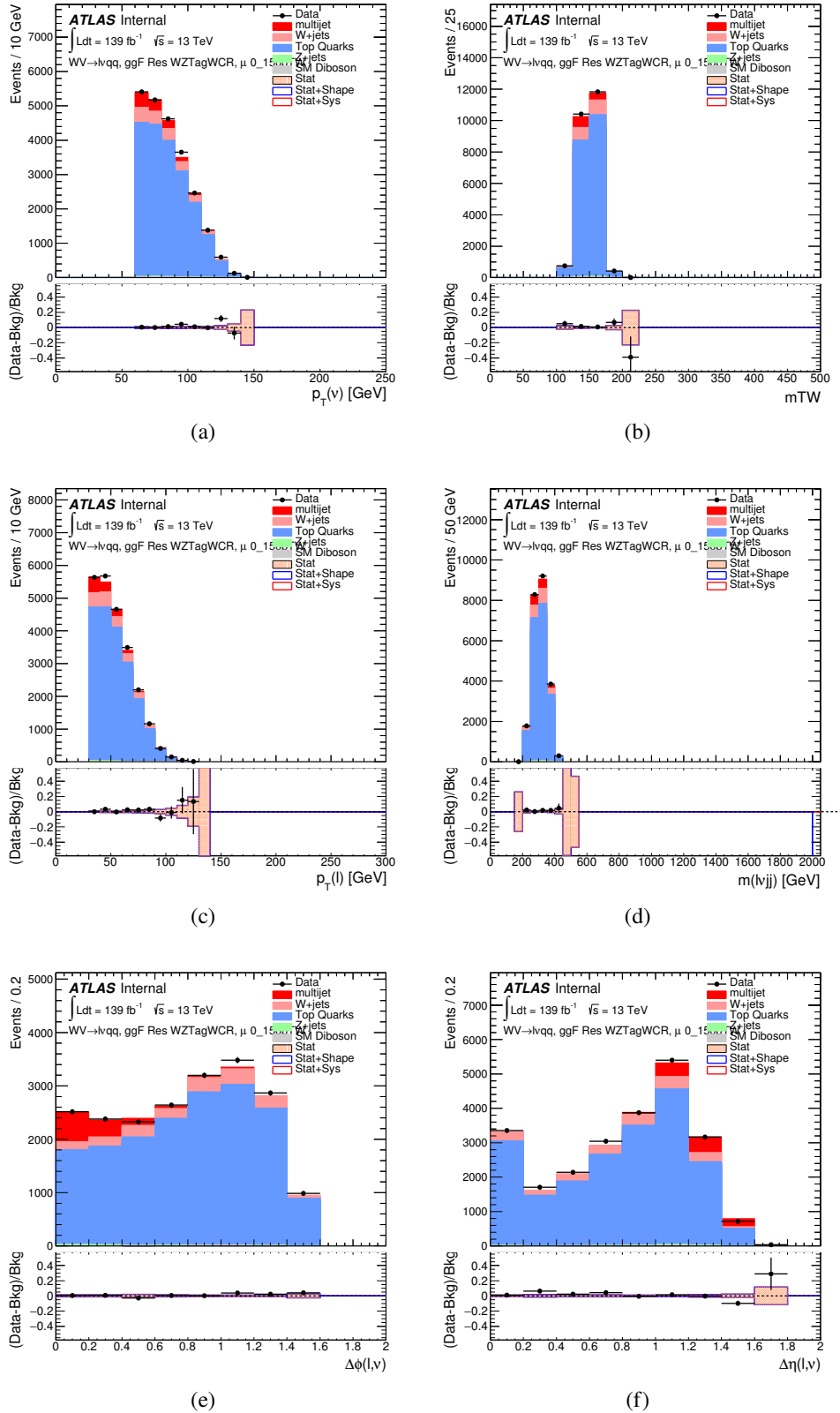


Figure 7.20: Postfit Data/MC comparison of distributions of E_T^{miss} , m_T^W , lepton and neutrino p_T , $m_{l\nu jj}$, lepton- ν angular distance in the WZ untag muon channel. The MJ template is obtained from the pre-MJ-fit.

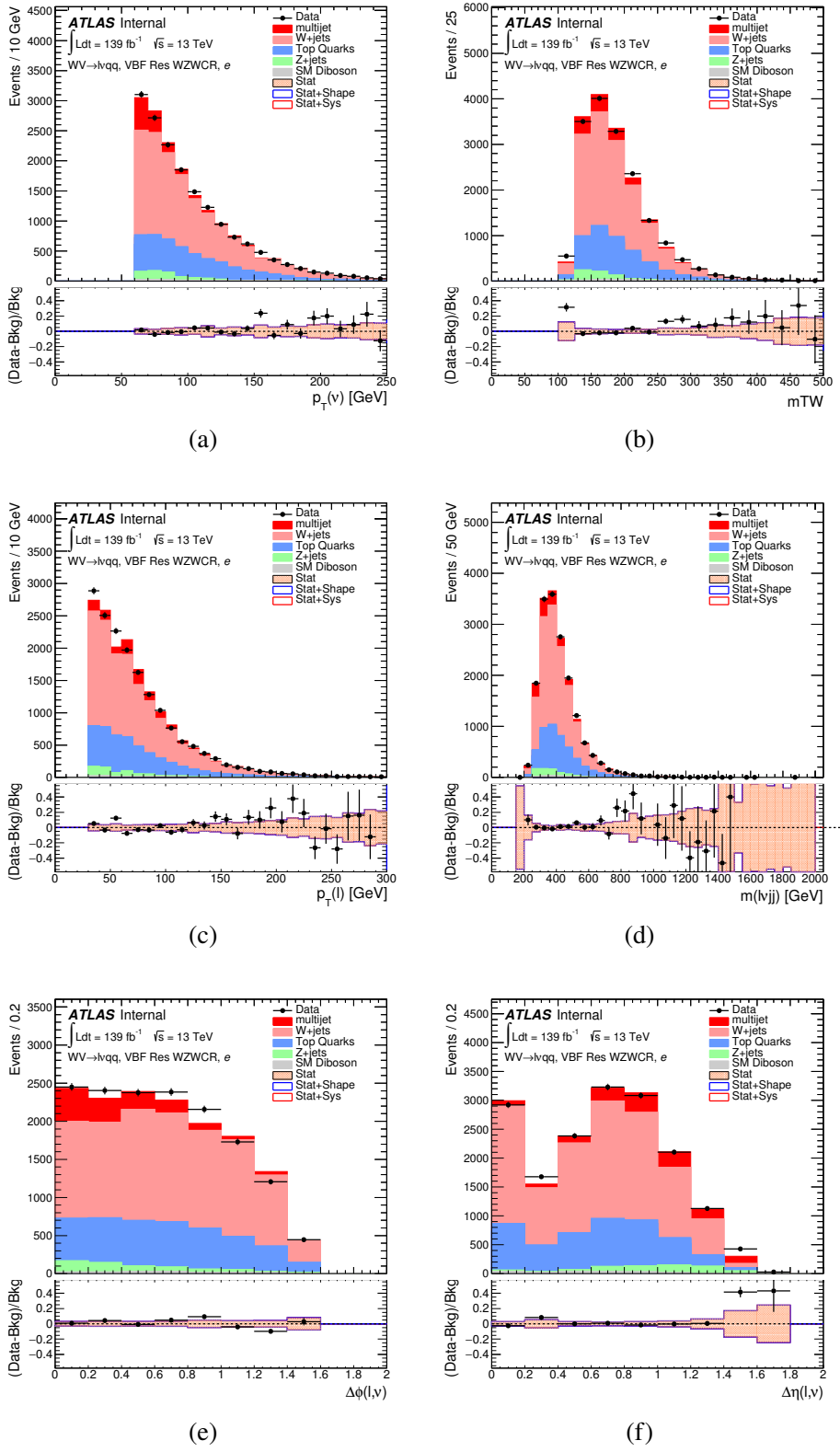


Figure 7.21: Postfit Data/MC comparison of distributions of E_T^{miss} , m_T^W , lepton and neutrino p_T , $m_{l\nu jj}$, lepton- ν angular distance in the VBF WW electron channel. The MJ template is obtained from the pre-MJ-fit.

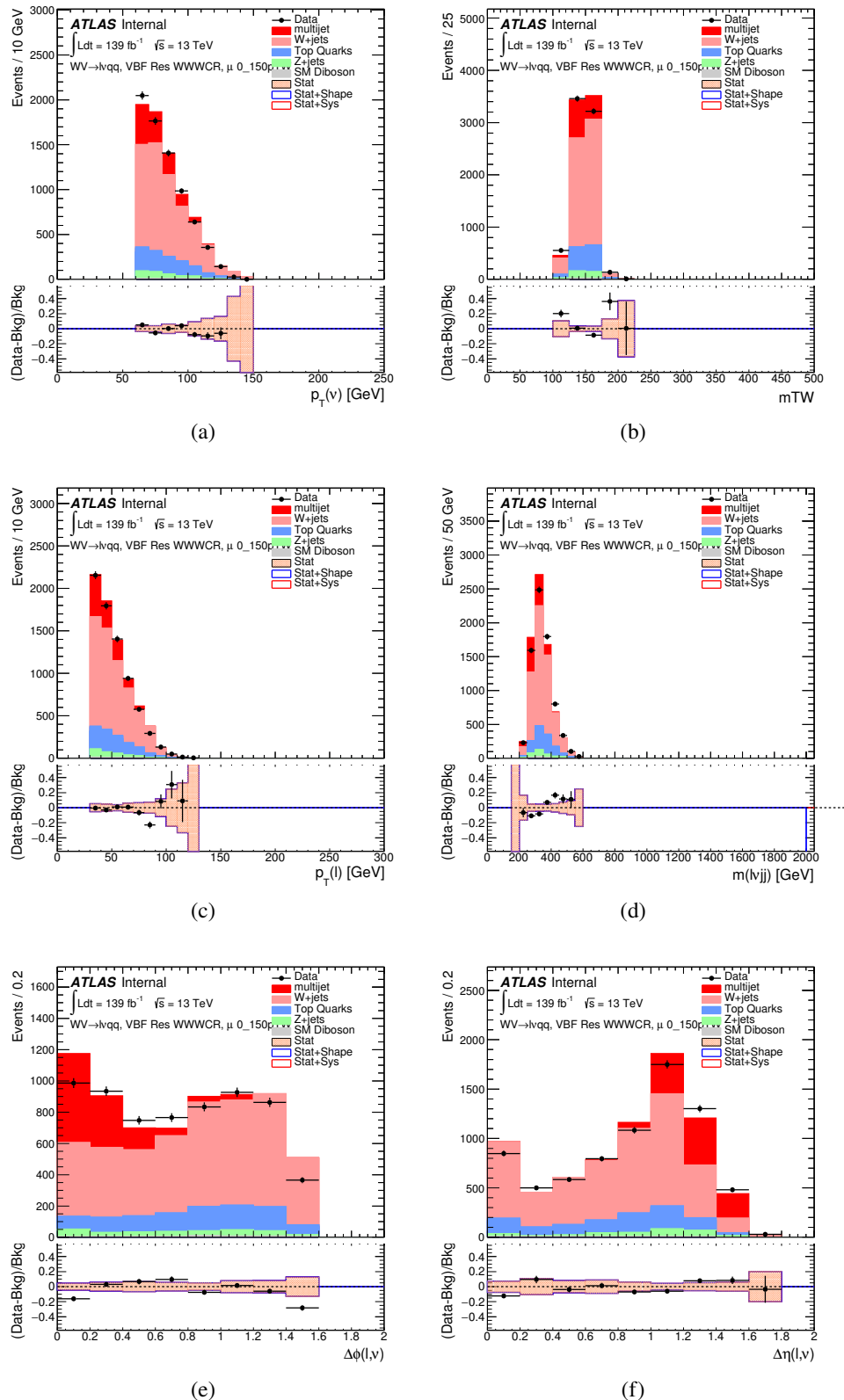


Figure 7.22: Postfit Data/MC comparison of distributions of E_T^{miss} , m_T^W , lepton and neutrino p_T , $m_{\ell\nu jj}$, lepton- ν angular distance in the VBF WW muon channel. The MJ template is obtained from the pre-MJ-fit.

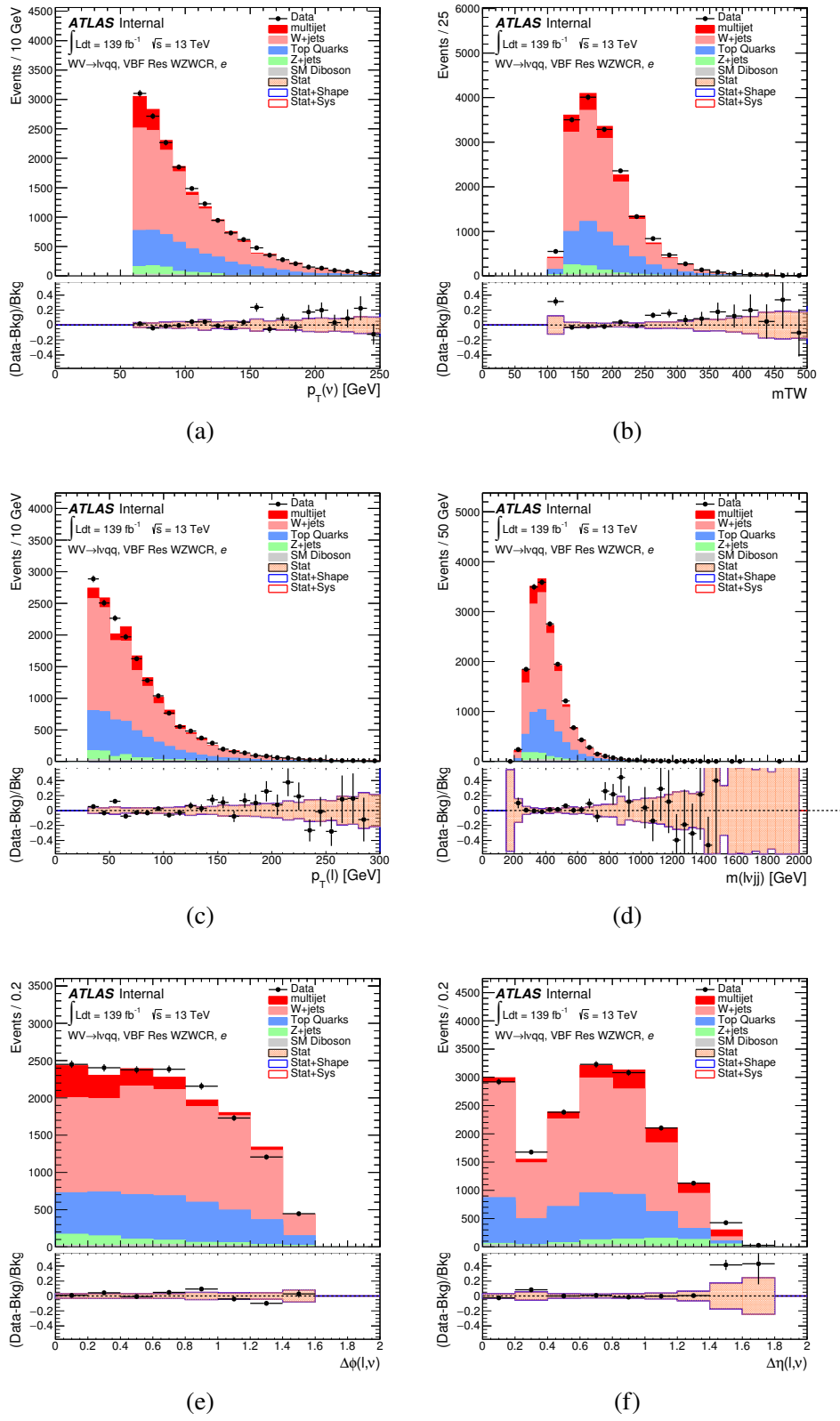


Figure 7.23: Postfit Data/MC comparison of distributions of E_T^{miss} , m_T^W , lepton and neutrino p_T , $m_{l\nu jj}$, lepton- ν angular distance in the VBF WZ electron channel. The MJ template is obtained from the pre-MJ-fit.

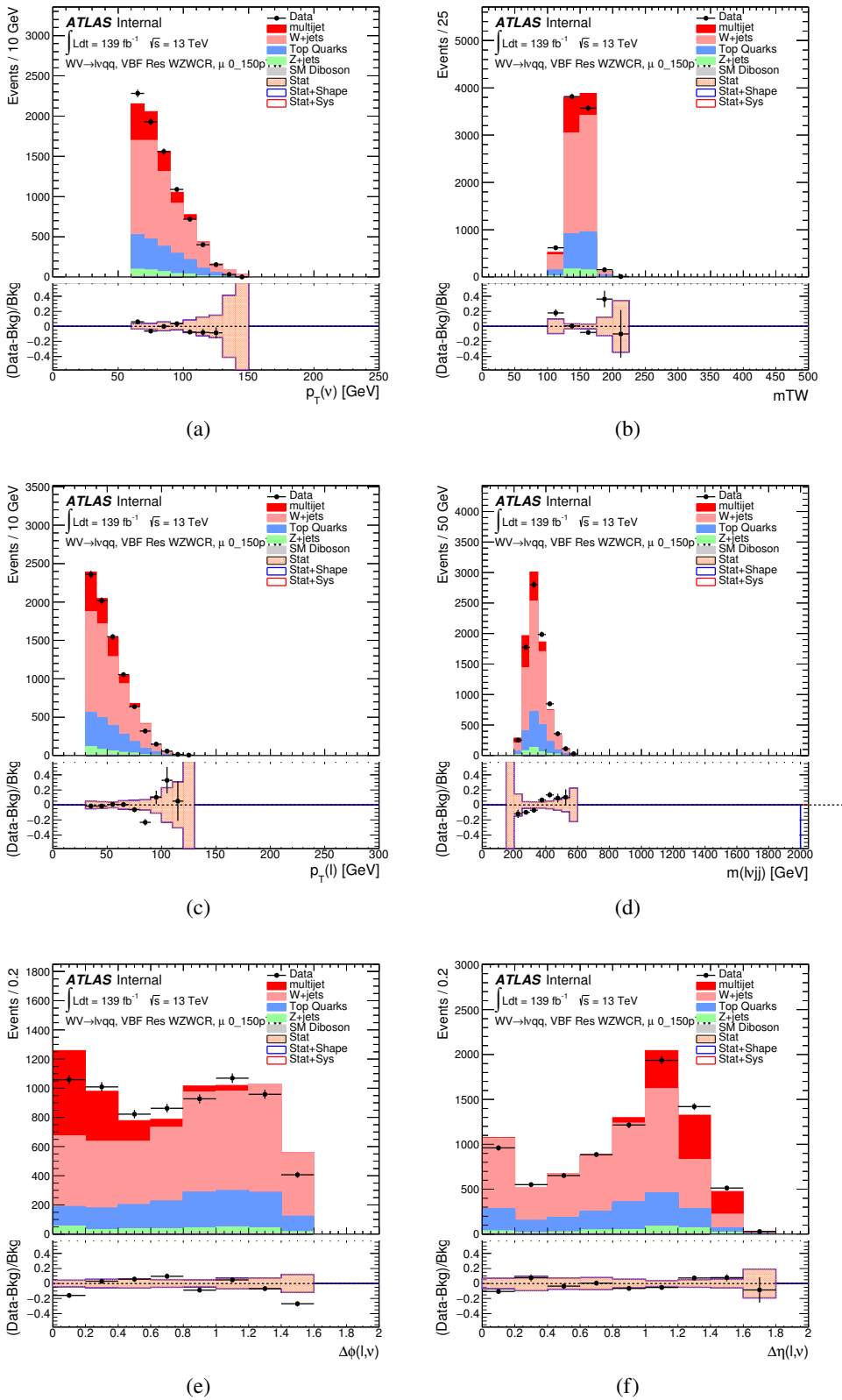


Figure 7.24: Postfit Data/MC comparison of distributions of E_T^{miss} , m_T^W , lepton and neutrino p_T , $m_{l\nu jj}$, lepton- ν angular distance in the VBF WZ muon channel. The MJ template is obtained from the pre-MJ-fit.

Full Run 2
ggF Res WWWCR

Sample	Yield	R.U.	SF
Top&W	645040 ± 1971.68	0.31%	0.998
Z&VV	24075.9		fixed
MJ_el	24156.3 ± 1224.62	5.06%	3.973
MJ_mu	35528.5 ± 923.94	2.60%	9.019

ggF Res WZ01bWCR

Sample	Yield	R.U.	SF
Top&W	644690 ± 1981.4	0.31%	0.997
Z&VV	24075.9		fixed
MJ_el	24366.5 ± 1232.69	5.05%	3.874
MJ_mu	35528.5 ± 921.27	2.58%	8.746

ggF Res WZ2bWCR

Sample	Yield	R.U.	SF
Top&W	71236.5 ± 688.74	0.97%	1.031
Z&VV	518.5		fixed
MJ_el	595.63 ± 449.34	75.44%	0.094
MJ_mu	1196.9 ± 222.13	18.56%	0.294

VBF Res WWWCR

Sample	Yield	R.U.	SF
Top&W	19032.3 ± 364.43	1.91%	0.928
Z&VV	1091.63		fixed
MJ_el	1425.73 ± 214.42	15.03%	0.235
MJ_mu	1281.36 ± 157.21	11.83%	0.314

VBF Res WZWCR

Sample	Yield	R.U.	SF
Top&W	21341.8 ± 392.21	1.84%	0.942
Z&VV	1111.75		fixed
MJ_el	1413.76 ± 230.36	16.29%	0.225
MJ_mu	1281.36 ± 157.21	12.27%	0.314

Table 7.5: Fit validation result in WCRs for 2015+16 data. The fit is done in various WCRs, in order to obtain the corresponding scale factors for MJ templates: ggF resolved WCR for the $WW \rightarrow lvqq$ selection, ggF resolved untagged WCR for the $WZ \rightarrow lvqq$ selection, ggF resolved tagged WCR for the $WZ \rightarrow lvqq$ selection, VBF resolved WCR for the $WW \rightarrow lvqq$ selection, and VBF resolved WCR for the $WZ \rightarrow lvqq$ selection. Post-fit event yields for electroweak processes and MJ contributions are shown. The SF column shows the corresponding normalization scale factors for electroweak processes from the fit. R.U. stands for relative uncertainty.

966 **Chapter 8**

967 **Systematic Uncertainties**

968 This section describes the sources of systematic uncertainties considered in
969 this analysis. These uncertainties are divided into three categories: experimental
970 uncertainties, background modeling uncertainties, and theoretical uncertainties on
971 signal processes. In the statistical analysis each systematic uncertainty is treated
972 as a nuisance parameter estimated on the m_{VV} distribution.

973 **8.1 Experimental Systematics**

974 The uncertainty on the integrated luminosity of the dataset used is 1.7% and
975 a systematic in the final fit. This uncertainty was calculated using $x - y$ beam
976 separation scans [ref P55].

977 An additional source of systematic uncertainty is assigned to the pileup mod-
978eling in MC samples. This ensures simulated detector response and particle re-
979construction conditions are as similar as possible. The distribution of the average
980number of interactions per bunch crossing applied to simulation is called the μ pro-
981file. The pileup modeling uncertainty is accounted for by re-weighting simulated
982events so the average number of interactions per bunch crossing varies within its

983 uncertainty due to systematics from vertex reconstruction [ref ATL-COM-SOFT-
984 2015-119]. The associated re-weighting factors are propagated through the entire
985 analysis chain to construct a systematic uncertainty on m_{VV} .

986 The single-lepton and E_T^{miss} triggers used are not fully efficient, so scale factors
987 are applied to simulation to more accurately model the data. These scale factors
988 are given by the ratio of the distribution of offline objects before trigger selection
989 and after trigger selection. The associated uncertainty on these scale factors are
990 used in the final fit.

991 Uncertainties on small-R jet energy scale and resolution are measured in-situ
992 by calculating the response between data and simulation. This analysis uses a
993 reduced set of JES and JER uncertainties (totaling 30 and 8 systematics, re-
994 spectively). These reduced sets of systematics are calculated using a principal
995 component analysis, yield largely uncorrelated independent systematics. These
996 uncertainties on JES and JER account for the dependence on p_T , η , μ , flavor re-
997 sponse and global sequential corrections. Systematic uncertainties associated with
998 b -tagging are also considered. These systematics are evaluated as uncertainties on
999 the scale factor which account for the difference in b -tagging efficiencies in data
1000 and MC, and the flavor dependence (between b, c, and light jets).

1001 The uncertainty on the p_T scale of the large-R jets is determined by comparing
1002 the jet's p_T^{calo} to p_T^{track} in di-jet simulation and data. In addition to this uncertain-
1003 ties from tracking, modeling (Pythia vs Herwig), and statistical constraints are
1004 also calculated. The large-R jet p_T resolution is given by smearing the jet p_T with
1005 a Gaussian with a 2% width.

1006 The W/Z -tagging efficiency cannot be evaluated using the Rtrk method as the
1007 TCC algorithm uses track measurements to reconstruct jet substructure variables.
1008 In order to avoid this potential bias, the W/Z -tagging is estimated in data using

1009 a control sample and corrected by comparing it with simulation. The efficiency
1010 to W/Z -induced signal is estimated by a $t\bar{t}$ control sample, while the efficiency
1011 to single- q/g background is estimated using a dijet sample. The effects of experi-
1012 mental and theoretical uncertainties on the efficiency scale factor are determined
1013 by taking the ratio of efficiencies in data and simulation. By taking this ratio the
1014 uncertainties not arising for jet mass and D_2 cancel.

1015 Lepton identification, reconstruction, isolation systematic uncertainties are de-
1016 termined by reconstructing the Z mass peak with a tag and probe method. The
1017 lepton energy and momentum scales are also measured with the Z mass peak.
1018 Additionally, the track-to-vertex association efficiency is used for muons.

1019 As E_T^{miss} is calculated using all the physics objects in the event, all those objects
1020 associated errors result in an uncertainty on E_T^{miss} . Additionally, the unassociated
1021 tracks used to construct E_T^{miss} contribute to the uncertainty on E_T^{miss} .

1022 8.2 Theory Systematics

1023 Theoretical uncertainties for signal and background processes arise from un-
1024 certainties in the parameters used in Monte Carlo simulation. In particular for
1025 the $t\bar{t}$, $W/Z+jets$, diboson backgrounds and signal samples, the QCD scale, PDF,
1026 generator and hadronization uncertainties were evaluated. To assess the QCD
1027 scale uncertainty the renormalization and factorization scales were scaled up and
1028 down by a factor of two at the event generation stage of sample production. Un-
1029 certainties due to the choice of the parton distribution functions were evaluated by
1030 re-weighting samples from the nominal PDF to a set of error PDFs which account
1031 for the uncertainty of the fits used to produce the PDF set. In addition to this,
1032 samples are re-weighted to different PDF sets to account for the arbitrariness of
1033 the PDF choice. The difference between the m_{WV} distributions using different

1034 event generators is assessed by comparing samples generated with different gen-
1035 erators. Similarly, the uncertainty in hadronization models is accounted for by
1036 comparing samples created using different hadronization models (e.g. $t\bar{t}$ Powheg
1037 is compared to AMC@NLO, $W + jets$ compares Sherpa and MadGraph+Pythia
1038 samples). Figures 8.2 - 8.8 show the impact of these uncertainties on the $t\bar{t}$ and
1039 $W/Z + jets$ backgrounds. Additionally, contributions to the diboson background
1040 for the VBF analysis were found to be small and were accounted for by including
1041 a 5(10)% systematic in the diboson normalization in the final fit.

1042 The normalization of the $t\bar{t}$ and $W+jets$ processes impact the multijet tem-
1043 plate shape. The impact of these normalizations was assessed by including a
1044 shape systematic on the multijet background from varying the $t\bar{t}$ and $W+jets$
1045 normalization factors.

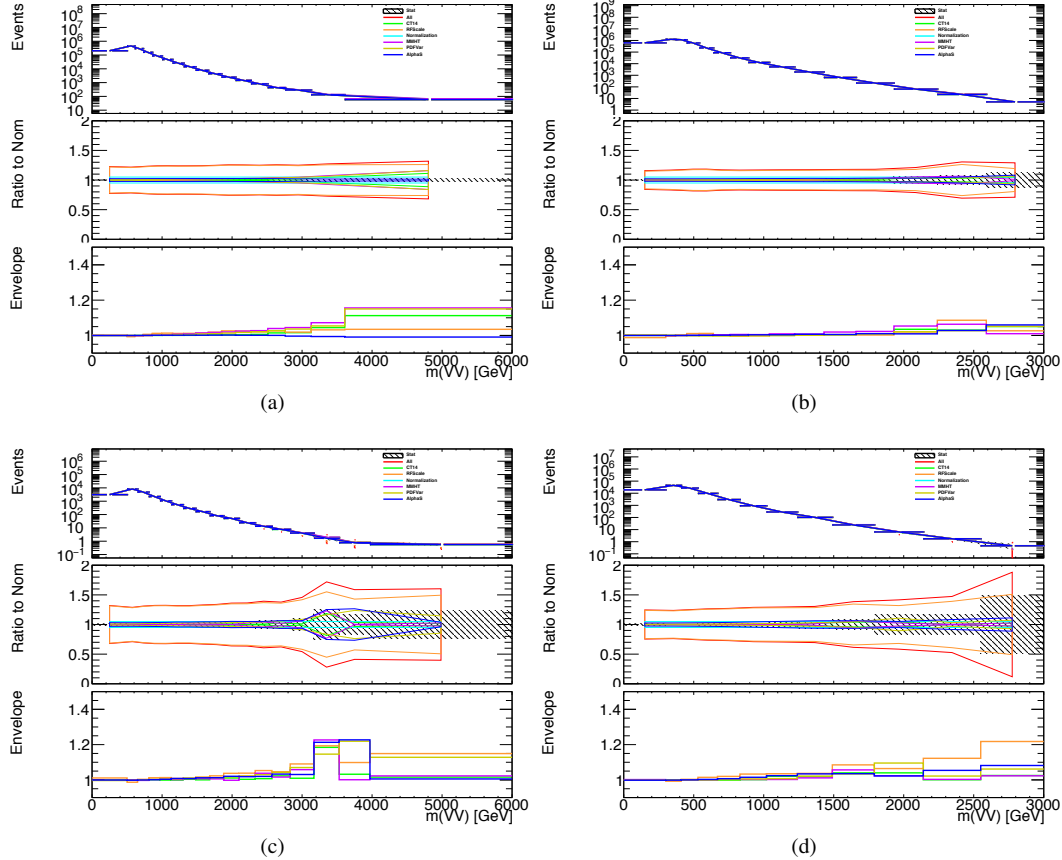


Figure 8.1: The $W/Z + \text{jet}$ systematics for the a) Merged ggF, b) Resolved ggF, c) Merged VBF, and d) Resolved VBF regions. The top subplot shows the nominal and variation distributions/bands, the middle shows the ratio of the two, and the final shows just the shape of the envelope (the final uncertainty).

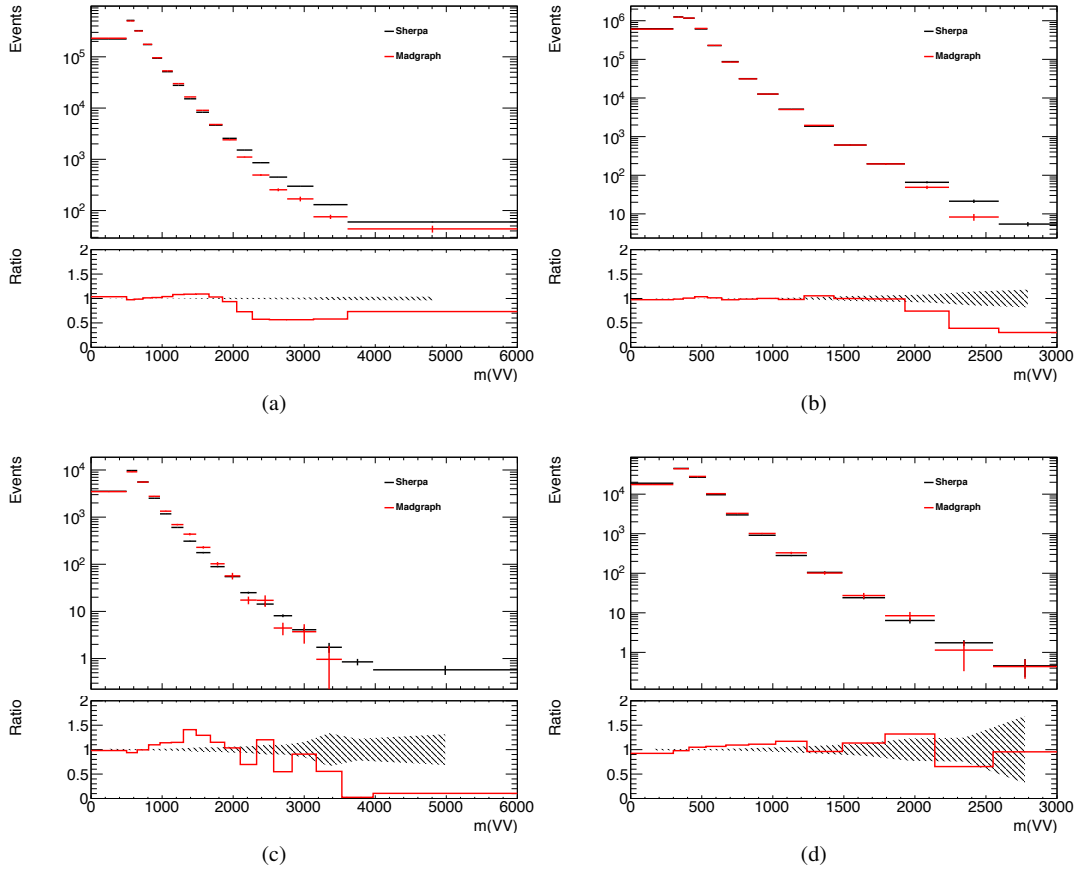


Figure 8.2: The two-point generator comparison between Sherpa and MadGraph for the $W/Z + \text{jet}$ samples in the a) Merged ggF, b) Resolved ggF, c) Merged VBF, and d) Resolved VBF regions. The normalization of the Madgraph sample is set to the Sherpa value to consider only shape effects. The bottom inset shows the ratio of the two.

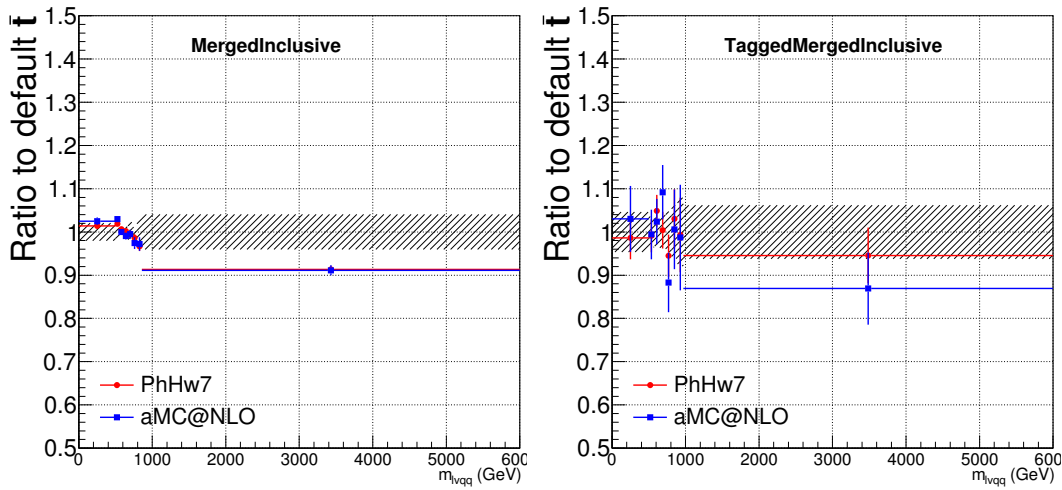


Figure 8.3: Ratio between the variations of generator (red) and hadronization (blue) variations for the Merged regime for $t\bar{t}$ sample.

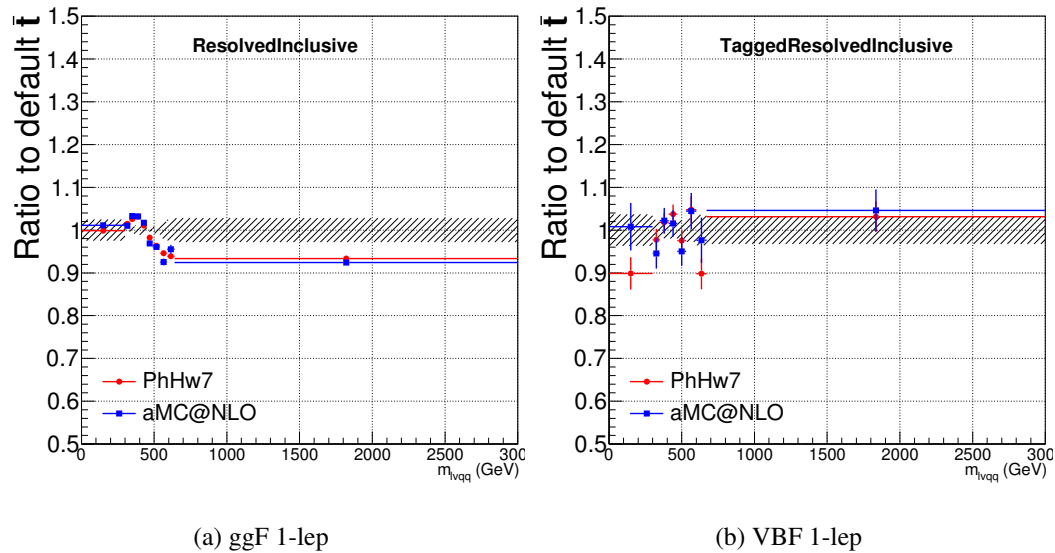


Figure 8.4: Ratio between the variations of generator (red) and hadronization (blue) variations for the Resolved regime for $t\bar{t}$ sample.

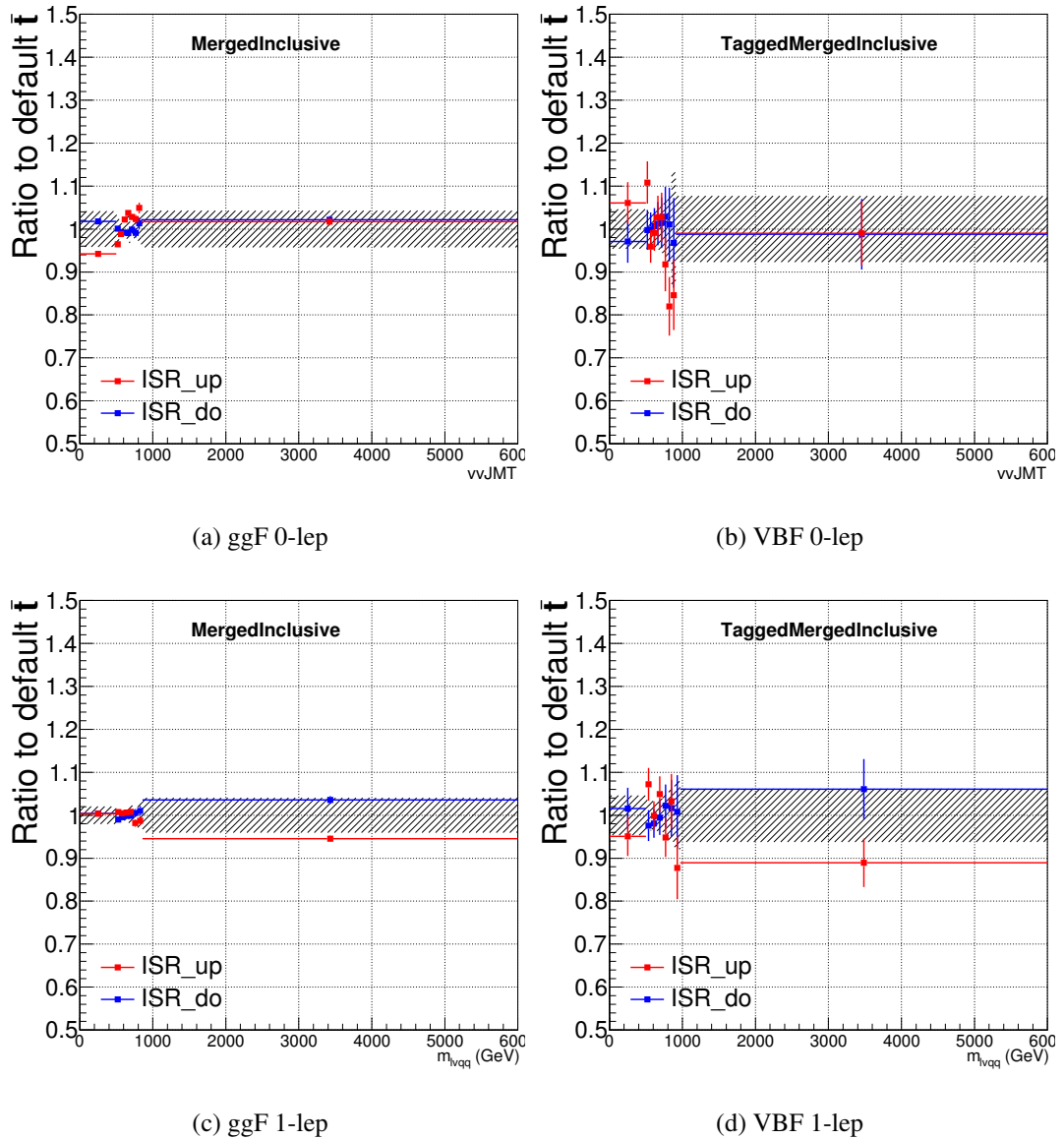


Figure 8.5: Ratio between the variations of ISR up (red) and down (blue) variations for the Merged regime for $t\bar{t}$ sample.

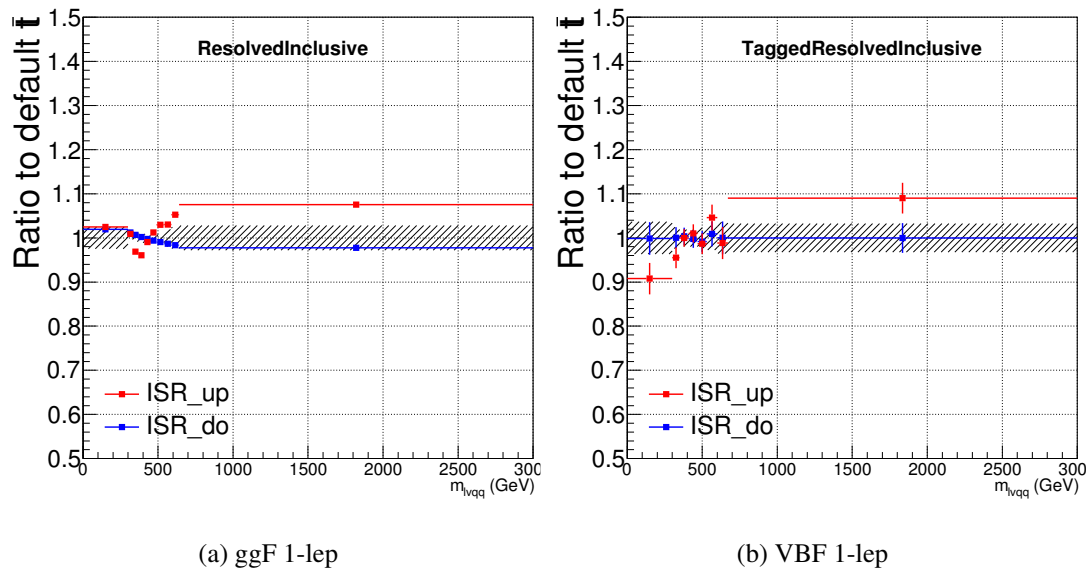


Figure 8.6: Ratio between the variations of ISR up (red) and down (blue) variations for the Resolved regime for $t\bar{t}$ sample.

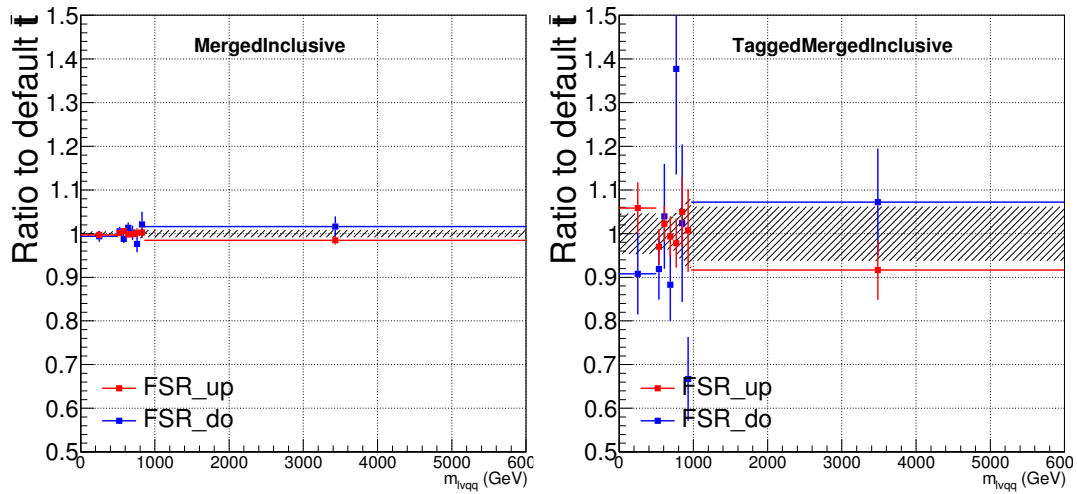


Figure 8.7: Ratio between the variations of FSR up (red) and down (blue) variations for the Merged regime for $t\bar{t}$ sample.

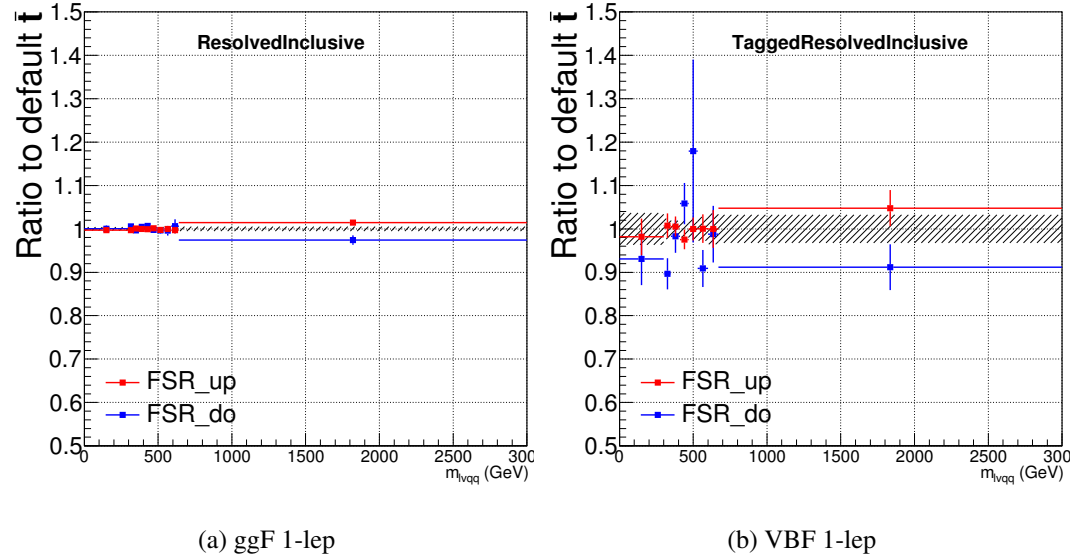


Figure 8.8: Ratio between the variations of FSR up (red) and down (blue) variations for the Resolved regime for $t\bar{t}$ sample.

1046 **Chapter 9**

1047 **Statistical Analysis**

1048 To determine the compatibility of the data collected with the proposed reso-
1049 nances a statistical procedure based on a likelihood function is used. A discovery
1050 test is used to measure the compatibility of the observed data with the back-
1051 ground only hypothesis. If the observed data is sufficiently incompatible with the
1052 background only hypothesis, this could indicate a discovery. In the absence of
1053 discovery, upper limits on the signal strength parameter, μ , are assessed using the
1054 CLs method.

1055 **9.1 Likelihood Function Definition**

1056 The likelihood function is product of Poisson probabilities for all analysis bins
1057 and systematic constraints:

$$\mathcal{L}(\mu, \boldsymbol{\theta}) = \prod_c \prod_i \frac{(\mu s_{ci}(\boldsymbol{\theta}) + b_{ci}(\boldsymbol{\theta}))^{n_{ci}}}{n_{ci}!} e^{-(\mu s_{ci}(\boldsymbol{\theta}) + b_{ci}(\boldsymbol{\theta}))} \prod_k (\theta'_k | \theta_k) \quad (9.1)$$

1058 Here c are the analysis channels considered and i runs over all the $m_{\ell\nu qq}$ bins
1059 used in the fit. The signal strength parameter, μ , multiplies the expected signal

1060 yield in each analysis bin, s_{ci} . The background content for channel c and bin i is
1061 given by b_{ci} . The dependence of signal and background predictions on system-
1062 atic uncertainties is described by the aforementioned set of nuisance parameters
1063 $\boldsymbol{\theta}$, which are parameterized by Gaussian or log-normal priors denoted here as
1064 θ_k . Statistical uncertainties of the simulated bin contents are also included as
1065 systematic uncertainties. Most systematics are correlated among all the analysis
1066 regions and considered to be independent from each other. The validity of this
1067 assumption is checked by evaluating the covariance of nuisance parameters.

1068 9.2 Fit Configuration

1069 The binning of $m_{\ell\nu qq}$ in signal regions for likelihood fit is determined by the
1070 statistical uncertainty of signal mass width. For each signal mass point, the signal
1071 mass resolution is given by the fitted Gaussian width of the $m_{\ell\nu qq}$. The fitted
1072 signal widths are then fit to a line to give a parameterized signal mass width,
1073 as shown in Figures 9.1 and 9.2. Bin widths are set first to this parameterized
1074 signal mass resolution. Then if the statistical uncertainty of the data or simulated
1075 background is more than 50%, bins are merged until the statistical uncertainty is
1076 less than 50%. All control regions contain only a single bin.

1077 For this analysis, each signal model is fit in the Merged and Resolved chan-
1078 nels for the relevant signal production mode simultaneously. The $W + \text{jets}$ and $t\bar{t}$
1079 normalizations are given by the best fit values in the overall fit and these fitted
1080 normalizations are then applied to those backgrounds in the SRs.

1081 Systematics may be affected by low statistics, leading to unsmooth m_{VV} dis-
1082 tributions with unphysically large fluctuations. This can lead to artificial pulls
1083 and constraints in the fit. To remove such issues a multi-step smoothing pro-
1084 cedure is applied to all systematic variation distributions in all regions. First,

1085 distributions are rebinned until the statistical error per bin is at least 5%. Next
1086 all local extrema are identified. The bins around smallest extrema are iteratively
1087 merged until only four local extrema remain. Then distributions are rebinned so
1088 that statistical uncertainties in each bin are < 5%.

1089 For some systematics, up and down variations may be in the same direction
1090 with respect to the nominal distributions. This causes the variations to not cover
1091 the nominal choice, and the interpretation of the confidence interval is skewed as
1092 the nominal distribution should be bracketed by the up and down variations. This
1093 asymmetry may also lead to unconstrained systematics in the fit. To handle such
1094 asymmetric systematics, if the up and down variation for a given systematic are in
1095 the same direction for at least three m_{VV} bins the variation is averaged for those
1096 bins. The averaging procedure replaces bin-by-bin the up and down variation bins
1097 by $b_{\pm}^{new} = b_{nom} \pm \frac{|b_+ - b_-|}{2}$, where b_{nom} is the nominal bin content and b_{\pm} are the
1098 original up and down variation bin content. The same procedure is also applied to
1099 any variations where the integral of the difference between the up/down variation
1100 and the nominal distribution is twice that of the other down/up variation, further
1101 ensuring variations are symmetric around the nominal distribution.

1102 Finally, systematics that have a negligible effect on the m_{VV} distribution are
1103 not considered in the fit. Shape systematics where no bin in the variational dis-
1104 tribution deviates more than 1% from the nominal distribution (after normalizing
1105 all histograms to the nominal) are not included in the fit. Also, statistical bin
1106 uncertainties < 1% are ignored.

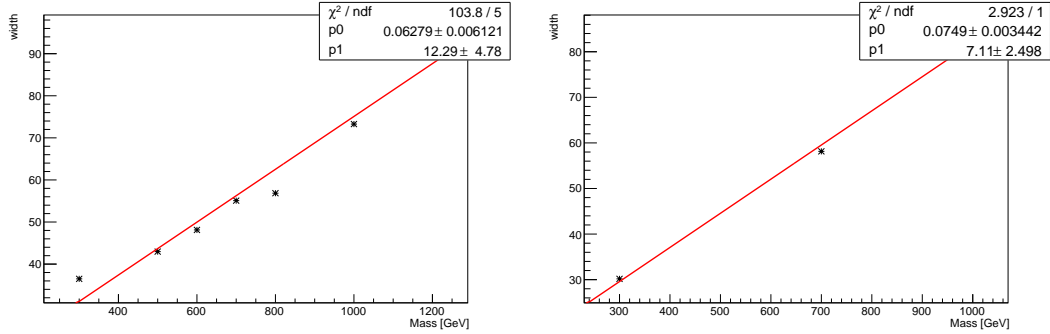


Figure 9.1: The HVT signal mass resolution as a function of mass fit with a straight line in the Resolved ggF region (left) and VBF (right) region.

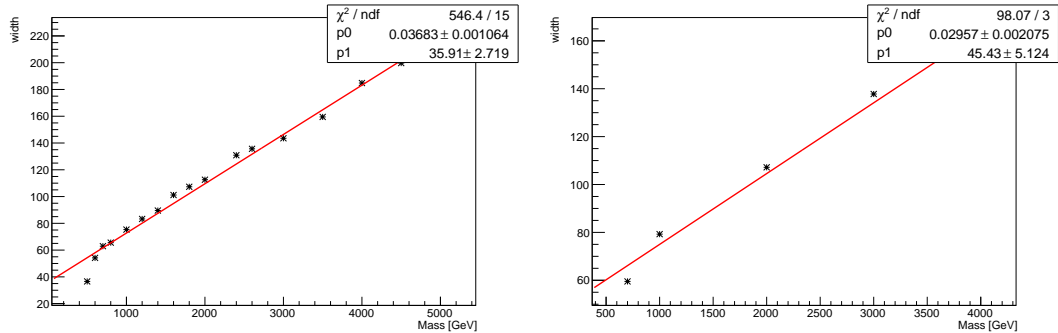


Figure 9.2: The HVT signal mass resolution as a function of mass fit with a straight line in the Merged ggF region (left) and VBF (right) region.

1107 9.3 Best Fit μ

1108 The best fit signal strength parameter is denoted by $\hat{\mu}$ and calculated by
 1109 maximizing the likelihood function with respect to all systematics and μ . The
 1110 corresponding set of systematics that maximize the likelihood are given by $\hat{\mu}$.
 1111 The first term in the likelihood is maximized when the expected number of signal
 1112 and background events is equal to the number of events in data ($n_{ci} = \mu s_{ci} +$
 1113 b_{ci}). Thus, by maximizing the likelihood, the fit determines values of μ and θ
 1114 that give the best agreement between expected and measured event yields. The

1115 second term in the likelihood is a penalty term which decreases the likelihood
1116 when systematics are shifted from their nominal values. This prevents the fit
1117 from profiling systematics in unphysical ways to maximize the likelihood. The
1118 uncertainty on μ is calculated by varying μ up and down until the natural log of
1119 the likelihood function shifts by one-half.

1120 9.4 Discovery Test

1121 To determine if the observed dataset is consistent with tested signal model a
1122 likelihood ratio is constructed:

$$\lambda(\mu) = \frac{\mathcal{L}(\mu, \hat{\theta}_\mu)}{\mathcal{L}(\hat{\mu}, \hat{\theta})} \quad (9.2)$$

1123 The denominator in this equation is the maximized value of \mathcal{L} over all system-
1124 atics and μ . The numerator is the maximized likelihood over all systematics for
1125 a given μ value, where the maximized systematics are given by $\hat{\mu}_\mu$. To test for
1126 the existence of signal the observed dataset the null hypothesis (H_0) is defined as
1127 the background only hypothesis and the alternate hypothesis includes signal and
1128 background (H_1). This test quantifies the compatibility of observed data with
1129 H_0 by calculating a p-value representing the probability of observing data as dis-
1130 crepant or more than the observed data under the H_0 . The test statistic used to
1131 calculate this p-value is given by (r_0):

$$r_0 = \begin{cases} -2 \ln \lambda(0), \hat{\mu} > 0 \\ +2 \ln \lambda(0), \hat{\mu} < 0 \end{cases} \quad (9.3)$$

1132 The expected distribution of the the test statistic under H_0 ($f(r_0|0)$) is used to
1133 calculate the p-value:

$$p_0 = \int_{r_0, obs}^{\infty} f(r_0 | 0) dr_0 \quad (9.4)$$

1134 Small p-values indicate the observed data is poorly described by H_0 . This
 1135 equivalent Z-score of a given p-value is usually used to further quantify the agree-
 1136 ment between the observed data and H_0 . The Z-score is given by the number of
 1137 standard deviations away from the mean of a Gaussian distribution, the integral
 1138 of the upper tail of the distribution would equal the p-value. Mathematically:

$$Z = \Phi^{-1}(1 - p_0) \quad (9.5)$$

1139 where Φ is the Gaussian cumulative distribution function. The statistical
 1140 significance of these tests are expressed as the Z -score. In particle physics, 3σ is
 1141 considered evidence for new phenomena and 5σ is the threshold for discovery.

1142 9.5 Exclusion Limits

1143 In the absence of discovery, upper limits on the signal strength, μ are set using
 1144 the CLs method [cite P60]. The test statistic for this test, q_μ , is constructed as:

$$\tilde{\lambda}_\mu = \begin{cases} \frac{\mathcal{L}(\mu, \hat{\theta}_\mu)}{\mathcal{L}(\hat{\mu}, \hat{\theta})}, \hat{\mu} > 0 \\ \frac{\mathcal{L}(\mu, \hat{\theta}_\mu)}{\mathcal{L}(0, \hat{\theta}_0)}, \hat{\mu} < 0 \end{cases} \quad (9.6)$$

$$\tilde{q}_\mu = \begin{cases} -2 \ln \tilde{\lambda}(\mu), \hat{\mu} < \mu \\ +2 \ln \tilde{\lambda}(\mu), \hat{\mu} > \mu \end{cases} \quad (9.7)$$

1145 As defined, larger values of q_μ correspond to increasing incompatibility between
 1146 the observed data and the background + signal hypothesis. The observed value
 1147 of the test statistic, $q_{\mu, obs}$, is then compared to its expected distribution, f , to

1148 calculate p-values to assess the likelihood of the background+signal hypothesis.

1149 Using these distributions, CL_s values are computed as:

$$1150 \quad CL_{s+b} = \int_{q_{\mu,obs}}^{\infty} f(q_{\mu}|\mu) dq_{\mu} \quad (9.8)$$

$$1151 \quad CL_b = \int_{q_0^{obs}}^{\infty} f(q_{\mu}|\mu = 0) dq_{\mu} \quad (9.9)$$

$$1152 \quad CL_s = \frac{CL_{s+b}}{CL_b} \quad (9.10)$$

1153 CL_{s+b} is the p-value for the signal + background hypothesis and CL_b is the
1154 p-value for the background only hypothesis. The CL_s value is interpreted as
1155 the probability to observe the background + signal hypothesis normalized to the
1156 probability of background-only hypothesis. Normalizing by CL_b prevents setting
1157 artificially strong exclusion limits due to downward fluctuations in data.

1158 For a given signal hypothesis, μ values are scanned simultaneously over all
1159 m_{WV} bins to find the μ value that yields $CL_s=0.05$, meaning the likelihood of
1160 finding data more incompatible with the signal+background hypothesis (relative
1161 to the background only hypothesis) is 5%. The 95% upper limit on the cross
1162 section is then calculated as the product of the μ value found, branching ratio,
1163 and theory cross section.

Part IV

1163

Results

1164

1165 **Chapter 10**

1166 **Statistical Interpretation**

1167 **10.1 Discovery Tests**

1168 To test for the existence of signal in the observed dataset, the discovery tests
1169 discussed earlier are used to calculate p-values as a function of resonance mass.
1170 The results of these tests are shown in Figures 10.1 - 10.5. Across the different
1171 DY signals the largest excesses are $\sim 2.2\sigma$ at 600 GeV and 1.8σ at 2 TeV. The
1172 largest excesses for VBF signals are $< 2.5\sigma$ at for 1 TeV resonances. As these
1173 deviations do not constitute discoveries, upper limits on μ are calculated.

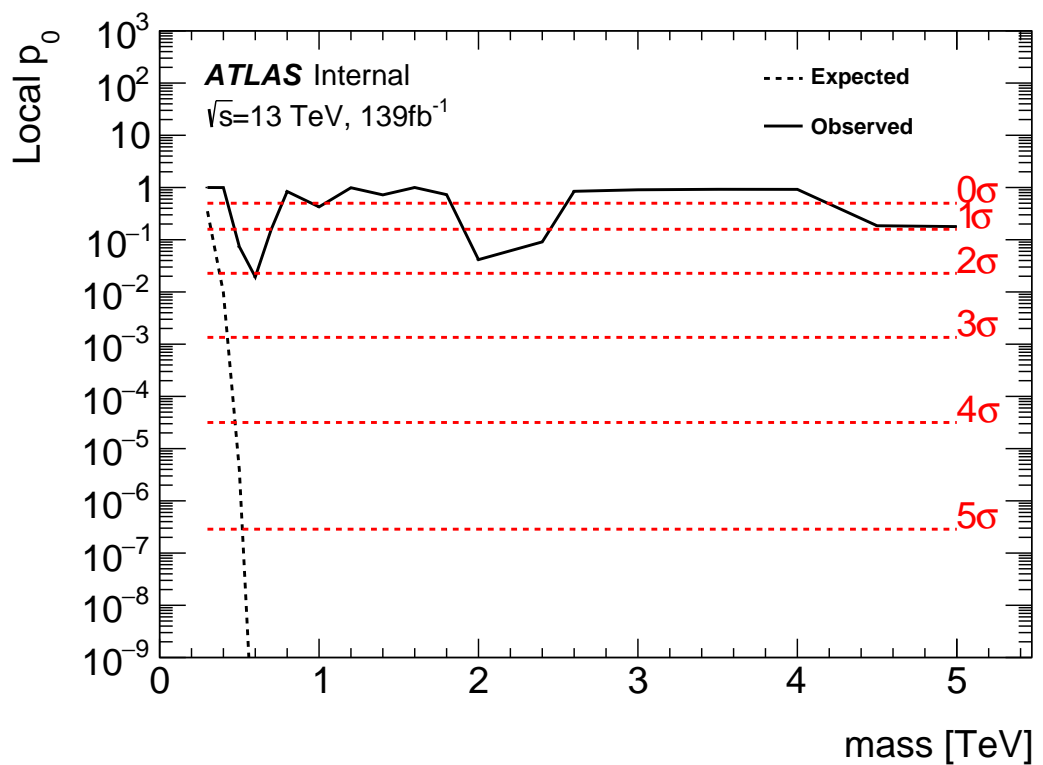


Figure 10.1: These plots show the measured p_0 value as a function of resonance mass for HVT Z' DY production.

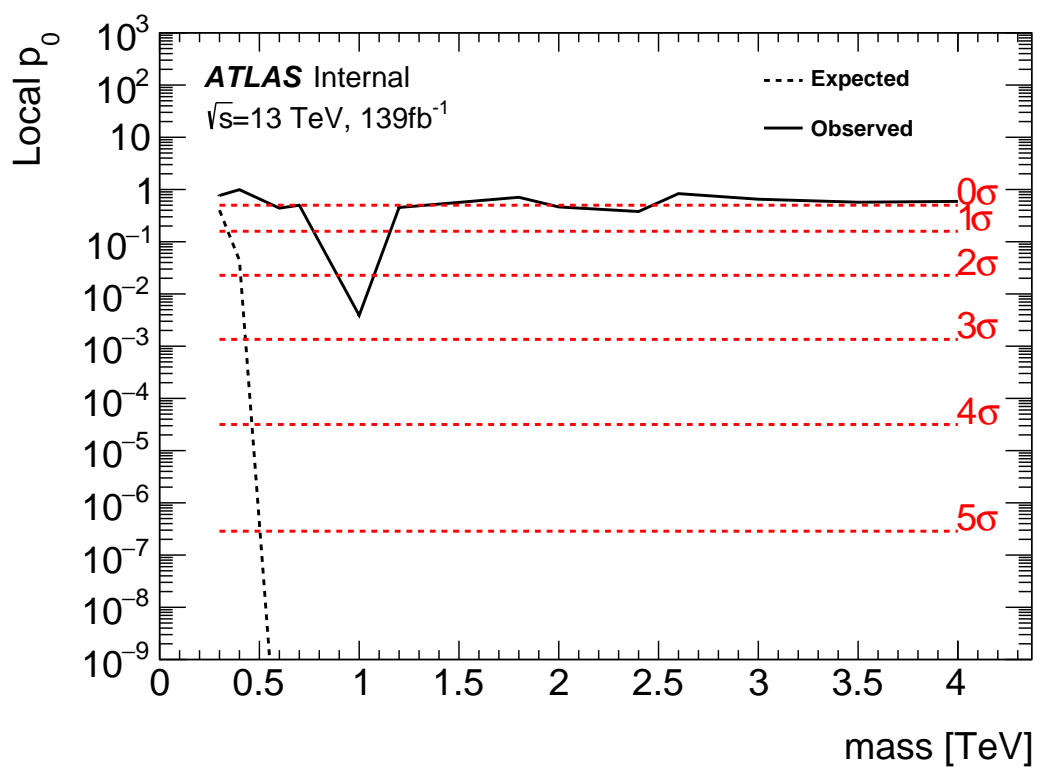


Figure 10.2: These plots show the measured p_0 value as a function of resonance mass for HVT Z' VBF production.

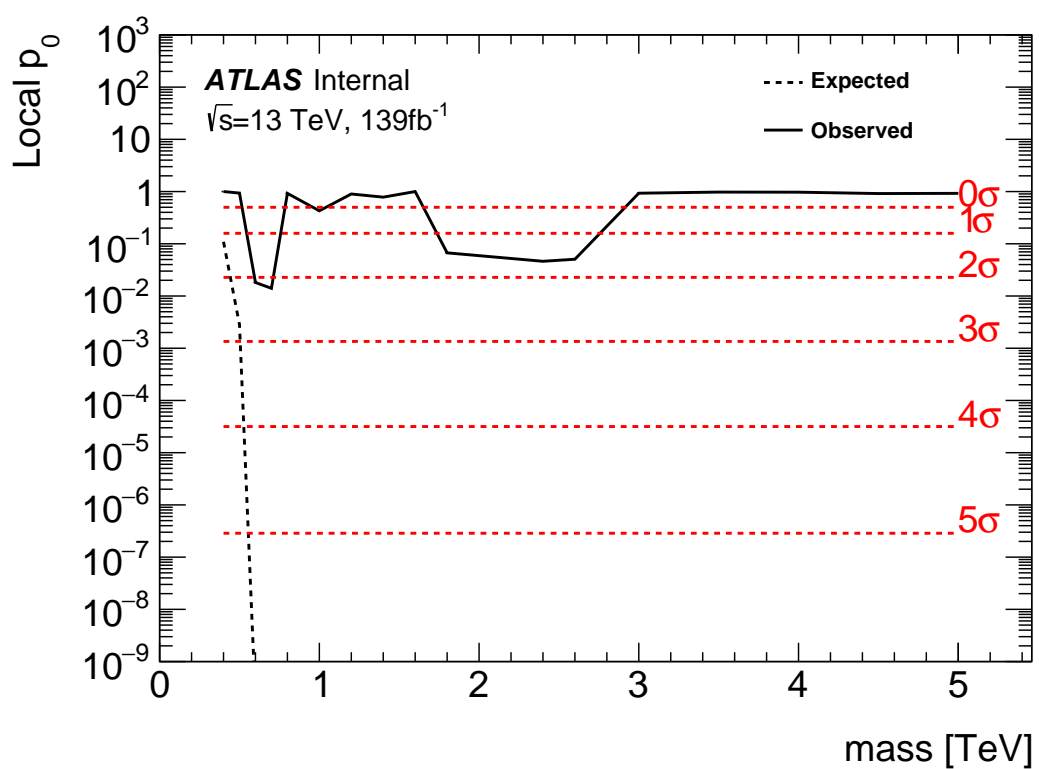


Figure 10.3: These plots show the measured p_0 value as a function of resonance mass for HVT W' DY production.

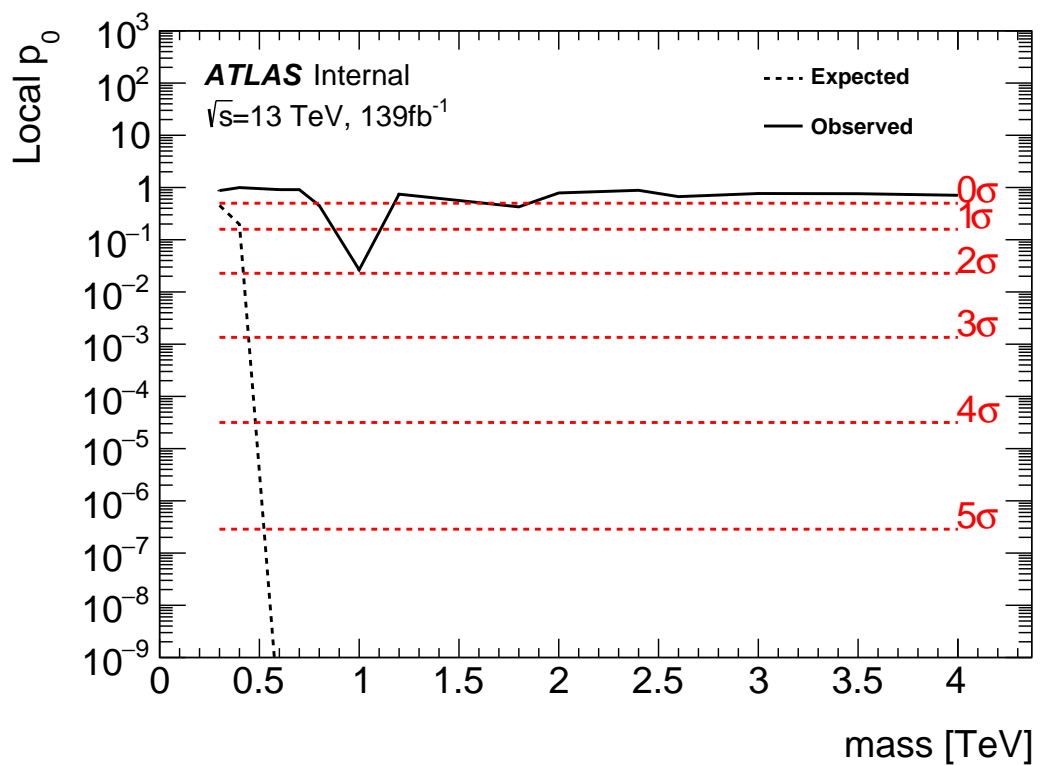


Figure 10.4: These plots show the measured p_0 value as a function of resonance mass for HVT W' VBF production.

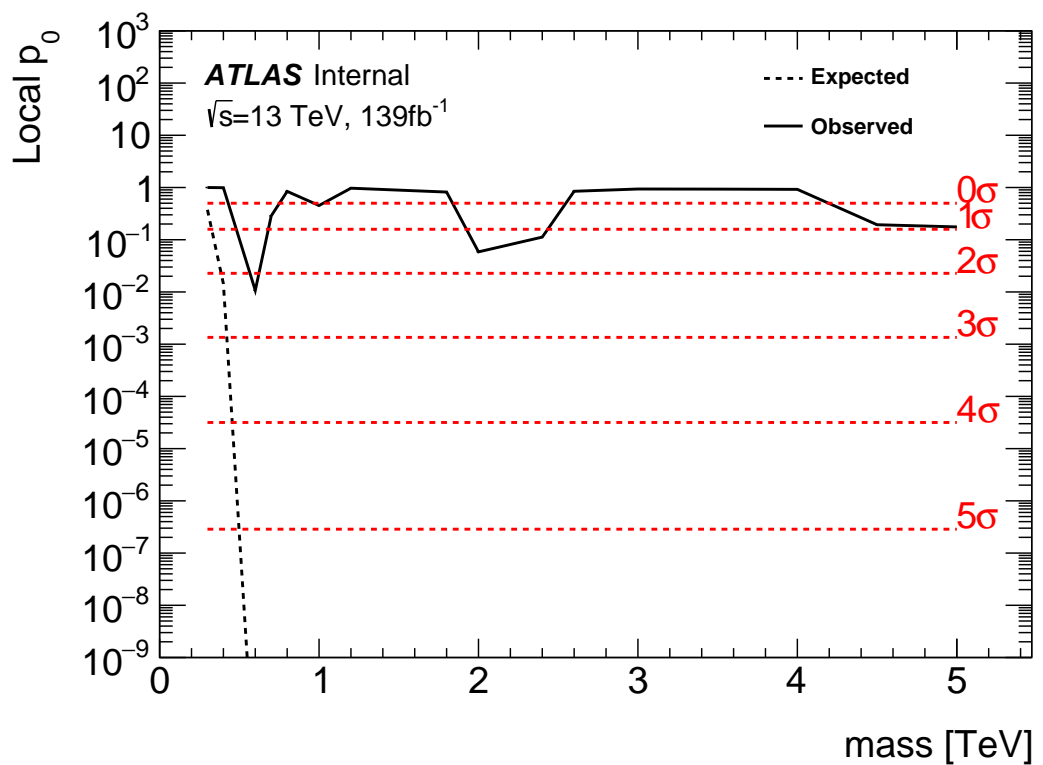
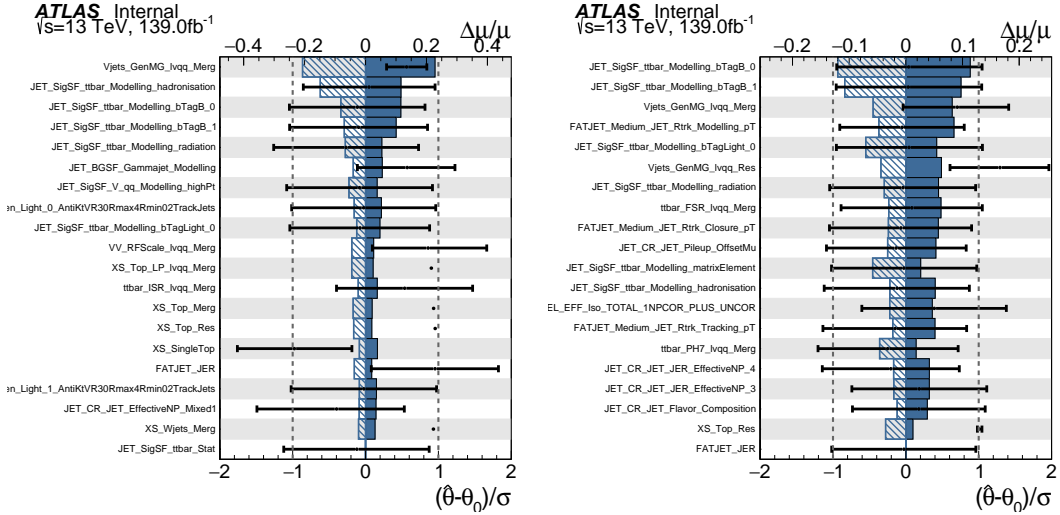


Figure 10.5: These plots show the measured p_0 value as a function of resonance mass for the RS Graviton DY production.

1174 10.2 Systematic Profiling and Correlations

1175 The ranked systematics and their fitted values are shown for the different anal-
 1176 ysis regions in Figure 10.6 - 10.8. Note that background normalizations for $W+jets$
 1177 and $t\bar{t}$ are left free to float in the fit. This means the nominal normalization val-
 1178 ues are at one and the uncertainties are not plotted in the ranked plots. Overall,
 1179 systematics are not pulled outside their uncertainties, especially for highly ranked
 1180 nuisance parameters.

1181 The correlation between systematics are shown in Figures ???. Correlations
 1182 between background normalization are expected. The remaining systematic cor-
 1183 relations are not very strong or unexpected.



1183 **Figure 10.6:** Ranked systematics and their fitted values for WW DY (right) and VBF (left) selections.

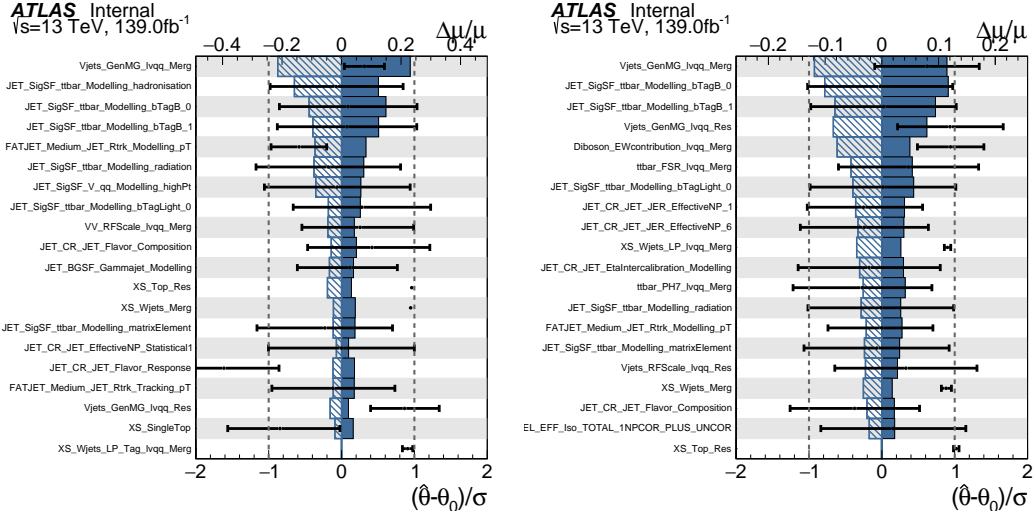


Figure 10.7: Ranked systematics and their fitted values for WZ DY (right) and VBF (left) selections.

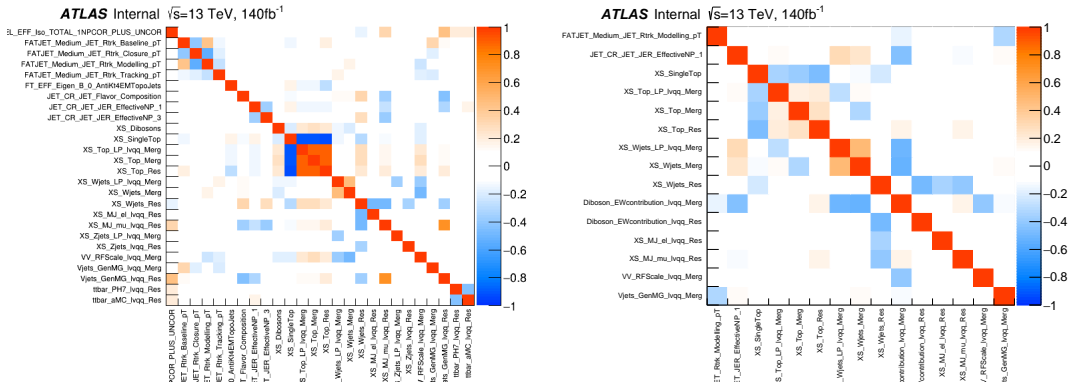


Figure 10.8: Correlations between systematics for WW DY (right) and VBF (left) selections.

1184 10.3 Expected and Measured Yields

1185 The yield tables for the four analysis regions are shown in Tables ?? - ?? . The
 1186 fitted background normalizations are shown in Tables ??-?? . The control region
 1187 $m_{\ell\nu qq}$ distributions are shown in Figures 10.9 - 10.12. The signal region $m_{\ell\nu qq}$
 1188 distributions are shown in Figures 10.13 - ?? .

	HP WCR	LP WCR	Resolved WCR
Electron Multi-jet	-	-	16507.83 ± 2314.87
Muon Multi-jet	-	-	19977.12 ± 2816.06
Diboson	1833.41 ± 177.78	3323.93 ± 320.92	9147.67 ± 961.63
Single-top	2160.62 ± 402.34	3551.09 ± 660.00	20058.36 ± 3817.26
$t\bar{t}$	15518.86 ± 338.22	24069.54 ± 453.15	138866.23 ± 1989.71
$W+jets$	40141.57 ± 357.79	88113.06 ± 487.87	673200.38 ± 4120.53
$Z+jets$	778.83 ± 78.93	1765.54 ± 179.10	16570.50 ± 1672.71
Total	60433.29 ± 664.92	120823.16 ± 1006.99	894328.12 ± 7247.12
Data	60264.00	120852.00	895362.00
	HP TCR	LP TCR	Resolved TCR
Electron Multi-jet	-	-	-
Muon Multi-jet	-	-	-
Diboson	421.11 ± 37.98	550.44 ± 53.10	996.87 ± 119.63
Single-top	4691.44 ± 846.11	3466.26 ± 631.03	16848.71 ± 3258.26
$t\bar{t}$	38945.18 ± 848.77	33836.95 ± 637.04	224226.14 ± 3212.76
$W+jets$	2258.34 ± 20.13	6564.78 ± 36.35	23466.41 ± 143.63
$Z+jets$	66.35 ± 6.72	213.26 ± 21.63	846.66 ± 85.47
Total	46382.43 ± 1199.25	44631.70 ± 899.23	266384.78 ± 4580.43
Data	46354.00	44629.00	266443.00
	WW SR	LP SR	Resolved 1-lepton SR
Electron Multi-jet	-	-	10788.40 ± 1512.85
Muon Multi-jet	-	-	15759.50 ± 2221.53
Diboson	4990.30 ± 376.50	3901.07 ± 313.22	16971.29 ± 1523.77
Single-top	3117.71 ± 565.07	2176.46 ± 400.52	20422.85 ± 3731.94
$t\bar{t}$	13785.77 ± 302.14	11005.12 ± 207.41	126965.25 ± 1819.66
$W+jets$	24718.56 ± 223.72	60080.66 ± 333.12	444133.56 ± 2719.02
$Z+jets$	478.18 ± 48.46	1226.69 ± 124.44	11686.32 ± 1179.69
Total	47090.52 ± 777.65	78389.98 ± 654.22	646727.19 ± 5963.98
Data	47330.00	78380.00	645610.00

Table 10.1: Expected and Measured for DY WW $W+jets$, $t\bar{t}$ control regions and signal regions.

	HP Untagged WCR	LP Untagged WCR	Resolved Untagged WCR
Electron Multi-jet	-	-	15080.03 ± 2277.99
Muon Multi-jet	-	-	27347.10 ± 2950.07
Diboson	1508.48 ± 154.20	2758.24 ± 284.50	9038.55 ± 728.69
Single-top	1756.59 ± 306.69	2913.18 ± 515.93	20511.74 ± 3523.47
$t\bar{t}$	13134.00 ± 238.30	21815.37 ± 334.98	140157.77 ± 2636.96
$W+jets$	40654.84 ± 333.65	87657.76 ± 501.96	665909.12 ± 4420.62
$Z+jets$	768.72 ± 77.97	1759.87 ± 178.96	16512.46 ± 1673.23
Total	57822.63 ± 540.40	116904.42 ± 862.16	894556.75 ± 7492.20
Data	57699.00	117306.00	895362.00
	HP Tagged WCR	LP Tagged WCR	Resolved Tagged WCR
Electron Multi-jet	-	-	384.58 ± 57.11
Muon Multi-jet	-	-	602.93 ± 190.12
Diboson	30.22 ± 4.69	48.95 ± 7.16	264.64 ± 28.24
Single-top	308.44 ± 56.19	371.59 ± 69.43	5752.39 ± 1029.97
$t\bar{t}$	1683.82 ± 48.73	2041.48 ± 70.00	58431.49 ± 614.30
$W+jets$	583.55 ± 75.37	1109.45 ± 85.78	11891.68 ± 903.01
$Z+jets$	13.19 ± 1.34	23.06 ± 2.34	324.74 ± 32.85
Total	2619.22 ± 106.00	3594.53 ± 130.90	77652.45 ± 1514.89
Data	2565.00	3546.00	77973.00
	HP Untagged TCR	LP Untagged TCR	Resolved Untagged TCR
Electron Multi-jet	-	-	-
Muon Multi-jet	-	-	-
Diboson	289.45 ± 28.45	346.78 ± 35.85	650.85 ± 65.56
Single-top	3107.99 ± 538.03	2250.64 ± 385.41	9606.87 ± 1698.22
$t\bar{t}$	30992.40 ± 562.33	26954.21 ± 413.89	91893.59 ± 1728.91
$W+jets$	2236.29 ± 18.35	4874.03 ± 27.91	16122.97 ± 107.03
$Z+jets$	71.54 ± 7.26	155.50 ± 15.81	577.71 ± 58.54
Total	36697.66 ± 779.03	34581.16 ± 567.59	118851.98 ± 2427.40
Data	36677.00	34573.00	118928.00
	HP Tagged TCR	LP Tagged TCR	Resolved Tagged TCR
Electron Multi-jet	-	-	-
Muon Multi-jet	-	-	-
Diboson	9.72 ± 1.13	8.75 ± 1.16	34.06 ± 4.98
Single-top	105.87 ± 20.65	119.66 ± 22.68	656.89 ± 132.96
$t\bar{t}$	1904.75 ± 50.61	1483.86 ± 47.05	17965.33 ± 188.87
$W+jets$	32.36 ± 4.28	85.74 ± 6.96	489.01 ± 37.13
$Z+jets$	1.27 ± 0.13	1.93 ± 0.20	19.14 ± 1.94
Total	2053.98 ± 54.84	1699.93 ± 52.70	19164.43 ± 234.01
Data	2047.00	1708.00	19143.00

Table 10.2: Expected and Measured for DY WZ $W+jets$, $t\bar{t}$ tag and untag control regions.

	HP Untagged SR	LP Untagged SR	Resolved Untagged SR
Electron Multi-jet	-	-	7782.17 ± 1175.56
Muon Multi-jet	-	-	17004.81 ± 1834.40
Diboson	3041.17 ± 273.77	2266.35 ± 212.79	14724.12 ± 1224.31
Single-top	2123.28 ± 373.83	1379.35 ± 240.92	18336.88 ± 3082.47
$t\bar{t}$	11678.86 ± 213.63	8906.34 ± 136.88	112669.24 ± 2122.46
$W+jets$	22741.32 ± 191.47	41726.76 ± 240.56	342934.00 ± 2280.21
$Z+jets$	442.03 ± 44.84	849.79 ± 86.42	9271.83 ± 939.52
Total	40026.65 ± 546.81	55128.59 ± 432.90	522723.03 ± 5131.71
Data	40193.00	54735.00	521813.00
	HP Tagged SR	LP Tagged SR	Resolved Tagged SR
Electron Multi-jet	-	-	199.22 ± 29.58
Muon Multi-jet	-	-	393.43 ± 124.06
Diboson	102.58 ± 11.59	65.44 ± 8.05	624.07 ± 58.10
Single-top	178.21 ± 33.62	155.53 ± 28.95	3470.39 ± 617.48
$t\bar{t}$	1017.93 ± 31.95	706.76 ± 26.20	38189.30 ± 401.91
$W+jets$	325.58 ± 41.62	575.36 ± 43.29	6161.96 ± 467.71
$Z+jets$	7.81 ± 0.80	11.62 ± 1.19	183.36 ± 18.55
Total	1632.11 ± 63.39	1514.70 ± 58.86	49221.74 ± 884.06
Data	1699.00	1559.00	48919.00

Table 10.3: Expected and Measured for DY WZ $W+jets$, $t\bar{t}$ tag and untag signal regions.

	HP WCR	LP WCR	Resolved WCR
Electron Multi-jet	-	-	898.48 ± 137.82
Muon Multi-jet	-	-	601.46 ± 182.74
Diboson	107.45 ± 45.20	166.87 ± 68.11	292.10 ± 235.29
Single-top	78.19 ± 18.22	132.71 ± 31.93	879.82 ± 216.89
$t\bar{t}$	400.71 ± 28.35	569.70 ± 48.88	5067.51 ± 155.69
$W+jets$	864.49 ± 63.44	1940.80 ± 89.41	18563.70 ± 408.99
$Z+jets$	19.51 ± 2.00	46.63 ± 4.77	795.20 ± 80.89
Total	1470.35 ± 84.89	2856.71 ± 126.74	27098.28 ± 594.01
Data	1495.00	2898.00	27120.00
	HP TCR	LP TCR	Resolved TCR
Electron Multi-jet	-	-	-
Muon Multi-jet	-	-	-
Diboson	14.95 ± 6.61	27.57 ± 14.12	24.33 ± 20.32
Single-top	68.31 ± 16.17	58.93 ± 13.56	278.60 ± 73.04
$t\bar{t}$	496.60 ± 31.72	401.23 ± 32.13	3834.49 ± 104.60
$W+jets$	50.68 ± 4.19	144.02 ± 7.86	450.01 ± 11.87
$Z+jets$	1.32 ± 0.14	5.35 ± 0.55	29.96 ± 3.07
Total	631.87 ± 36.45	637.10 ± 38.44	4617.39 ± 129.77
Data	636.00	634.00	4615.00
	HP SR	LP SR	Resolved SR
Electron Multi-jet	-	-	596.34 ± 91.52
Muon Multi-jet	-	-	481.01 ± 144.48
Diboson	148.84 ± 48.64	181.42 ± 67.30	395.52 ± 318.06
Single-top	79.49 ± 19.80	56.82 ± 14.89	782.07 ± 190.79
$t\bar{t}$	338.42 ± 24.14	236.80 ± 20.88	4261.70 ± 138.98
$W+jets$	501.13 ± 39.36	1347.76 ± 64.50	11445.73 ± 291.49
$Z+jets$	9.25 ± 0.95	28.77 ± 2.95	567.66 ± 57.94
Total	1077.13 ± 69.93	1851.57 ± 96.73	18530.03 ± 523.88
Data	1096.00	1846.00	18530.00

Table 10.4: Expected and Measured for VBF WW $W+jets$, $t\bar{t}$ control regions and signal regions.

	HP WCR	LP WCR	Resolved WCR
Electron Multi-jet	-	-	870.00 ± 132.75
Muon Multi-jet	-	-	618.45 ± 196.90
Diboson	92.92 ± 41.77	145.90 ± 64.26	228.62 ± 114.62
Single-top	71.13 ± 16.29	118.82 ± 27.98	1209.87 ± 281.64
$t\bar{t}$	427.80 ± 29.72	509.19 ± 46.57	6860.87 ± 254.83
$W+jets$	871.68 ± 64.22	2020.67 ± 93.54	19088.50 ± 442.10
$Z+jets$	19.58 ± 2.01	47.39 ± 4.85	800.19 ± 82.02
Total	1483.11 ± 83.79	2841.97 ± 125.92	29676.50 ± 644.96
Data	1495.00	2898.00	29755.00
	HP TCR	LP TCR	Resolved TCR
Electron Multi-jet	-	-	-
Muon Multi-jet	-	-	-
Diboson	10.12 ± 4.51	12.73 ± 6.55	14.23 ± 7.49
Single-top	51.57 ± 12.31	35.07 ± 8.17	169.21 ± 44.54
$t\bar{t}$	470.06 ± 28.97	298.99 ± 25.28	2414.75 ± 75.42
$W+jets$	49.64 ± 4.17	109.69 ± 6.16	378.22 ± 12.05
$Z+jets$	1.28 ± 0.13	4.81 ± 0.50	17.62 ± 1.83
Total	582.67 ± 32.07	461.30 ± 28.05	2994.03 ± 88.75
Data	584.00	459.00	3001.00
	HP SR	LP SR	Resolved SR
Electron Multi-jet	-	-	444.65 ± 67.99
Muon Multi-jet	-	-	397.29 ± 125.59
Diboson	109.66 ± 44.13	112.28 ± 46.45	265.75 ± 139.43
Single-top	63.16 ± 15.20	48.02 ± 11.56	872.16 ± 205.00
$t\bar{t}$	348.95 ± 24.34	190.68 ± 17.75	5134.25 ± 193.57
$W+jets$	467.21 ± 37.12	973.73 ± 47.91	10226.83 ± 254.67
$Z+jets$	8.15 ± 0.84	23.62 ± 2.43	558.48 ± 57.25
Total	997.13 ± 64.42	1348.33 ± 70.06	17899.41 ± 432.98
Data	1018.00	1313.00	17826.00

Table 10.5: Expected and Measured for VBF WZ $W+jets$, $t\bar{t}$ control regions and signal regions.

Background	Fitted Normalization
XS_Top_LP_lvqq_Merg_binned	$0.905^{+0.0166}_{-0.0166}$
XS_Top_Merg	$0.936^{+0.0199}_{-0.0199}$
XS_Top_Res	$0.957^{+0.0134}_{-0.0134}$
XS_Wjets_LP_lvqq_Merg_binned	$0.884^{+0.00489}_{-0.00489}$
XS_Wjets_Merg	$0.931^{+0.00831}_{-0.00831}$
XS_Wjets_Res	$1.03^{+0.00628}_{-0.00628}$

Table 10.6: Fitted background normalizations for $t\bar{t}$ and $W+jets$ backgrounds for the DY WW analysis region.

Background	Fitted Normalization
XS_Top_LP_Tag_lvqq_Merg_binned	$0.973^{+0.0333}_{-0.0333}$
XS_Top_LP_lvqq_Merg_binned	$0.894^{+0.0135}_{-0.0135}$
XS_Top_Merg	$0.893^{+0.016}_{-0.016}$
XS_Top_Res	$0.965^{+0.0179}_{-0.0179}$
XS_Top_Tag_lvqq_Merg_binned	$0.954^{+0.0276}_{-0.0276}$
XS_Top_Tag_lvqq_Res_binned	$0.999^{+0.0105}_{-0.0105}$
XS_Wjets_LP_Tag_lvqq_Merg_binned	$0.912^{+0.0703}_{-0.0703}$
XS_Wjets_LP_lvqq_Merg_binned	$0.876^{+0.00502}_{-0.00502}$
XS_Wjets_Merg	$0.948^{+0.00779}_{-0.00779}$
XS_Wjets_Res	$1.01^{+0.00673}_{-0.00673}$
XS_Wjets_Tag_lvqq_Merg_binned	$0.906^{+0.117}_{-0.117}$
XS_Wjets_Tag_lvqq_Res_binned	$1.2^{+0.0904}_{-0.0904}$

Table 10.7: Fitted background normalizations for $t\bar{t}$ and $W+jets$ backgrounds for the DY WZ analysis region.

Background	Fitted Normalization
XS_Top_LP_lvqq_Merg_binned	$0.79^{+0.0673}_{-0.0673}$
XS_Top_Merg	$0.888^{+0.061}_{-0.061}$
XS_Top_Res	$1.01^{+0.0311}_{-0.0311}$
XS_Wjets_LP_lvqq_Merg_binned	$0.88^{+0.0423}_{-0.0423}$
XS_Wjets_Merg	$0.881^{+0.0677}_{-0.0677}$
XS_Wjets_Res	$0.932^{+0.0202}_{-0.0202}$

Table 10.8: Fitted background normalizations for $t\bar{t}$ and $W+jets$ backgrounds for the VBF WW analysis region.

Background	Fitted Normalization
XS_Top_LP_lvqq_Merg_binned	$0.708^{+0.064}_{-0.064}$
XS_Top_Merg	$0.958^{+0.0644}_{-0.0644}$
XS_Top_Res	$1.02^{+0.038}_{-0.038}$
XS_Wjets_LP_lvqq_Merg_binned	$0.9^{+0.0438}_{-0.0438}$
XS_Wjets_Merg	$0.883^{+0.0685}_{-0.0685}$
XS_Wjets_Res	$0.945^{+0.0219}_{-0.0219}$

Table 10.9: Fitted background normalizations for $t\bar{t}$ and $W+jets$ backgrounds for the VBF WZ analysis region.

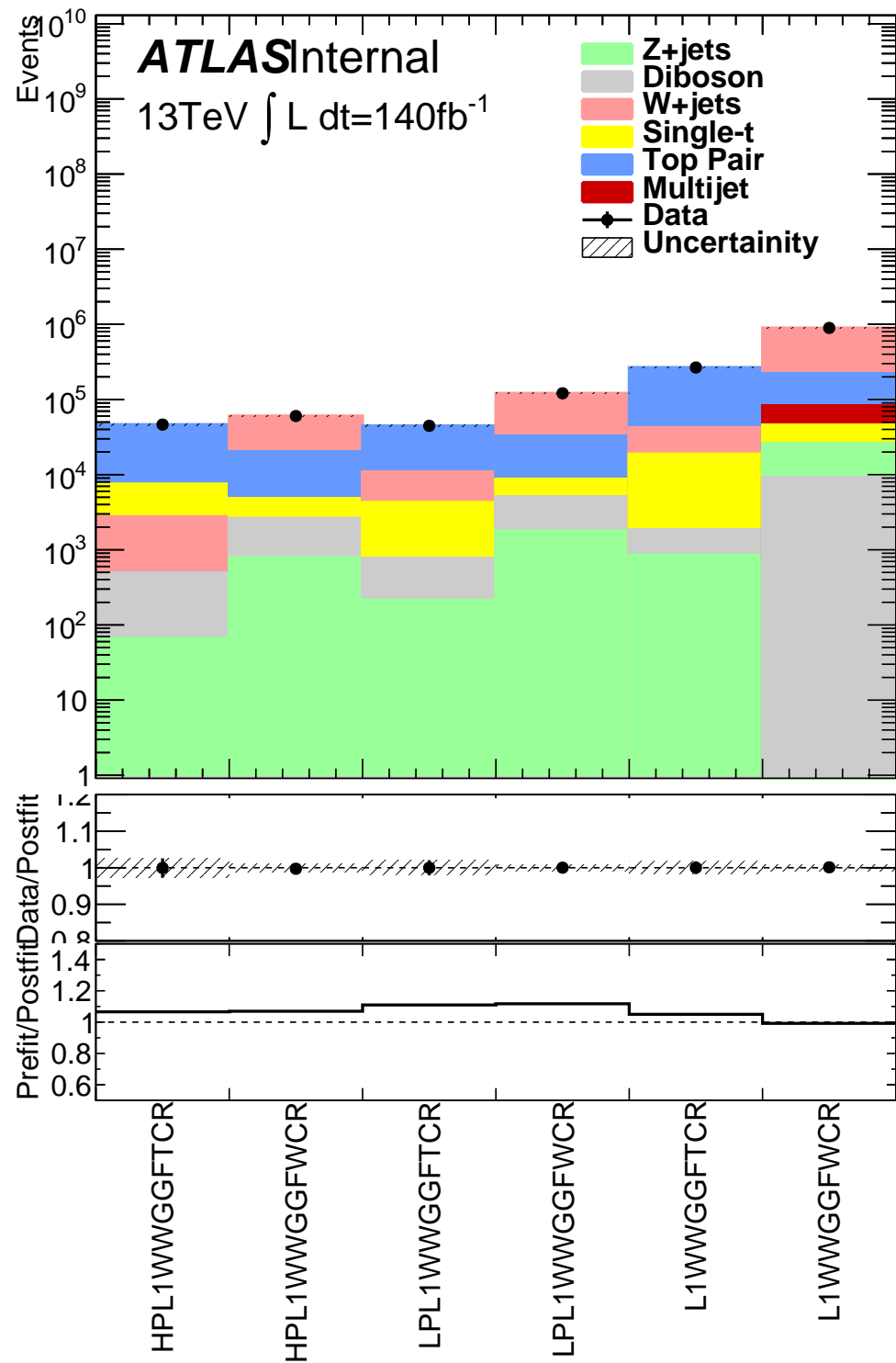


Figure 10.9: This figure shows the distribution of $m_{\ell\nu qq}$ in the DY WW control regions.

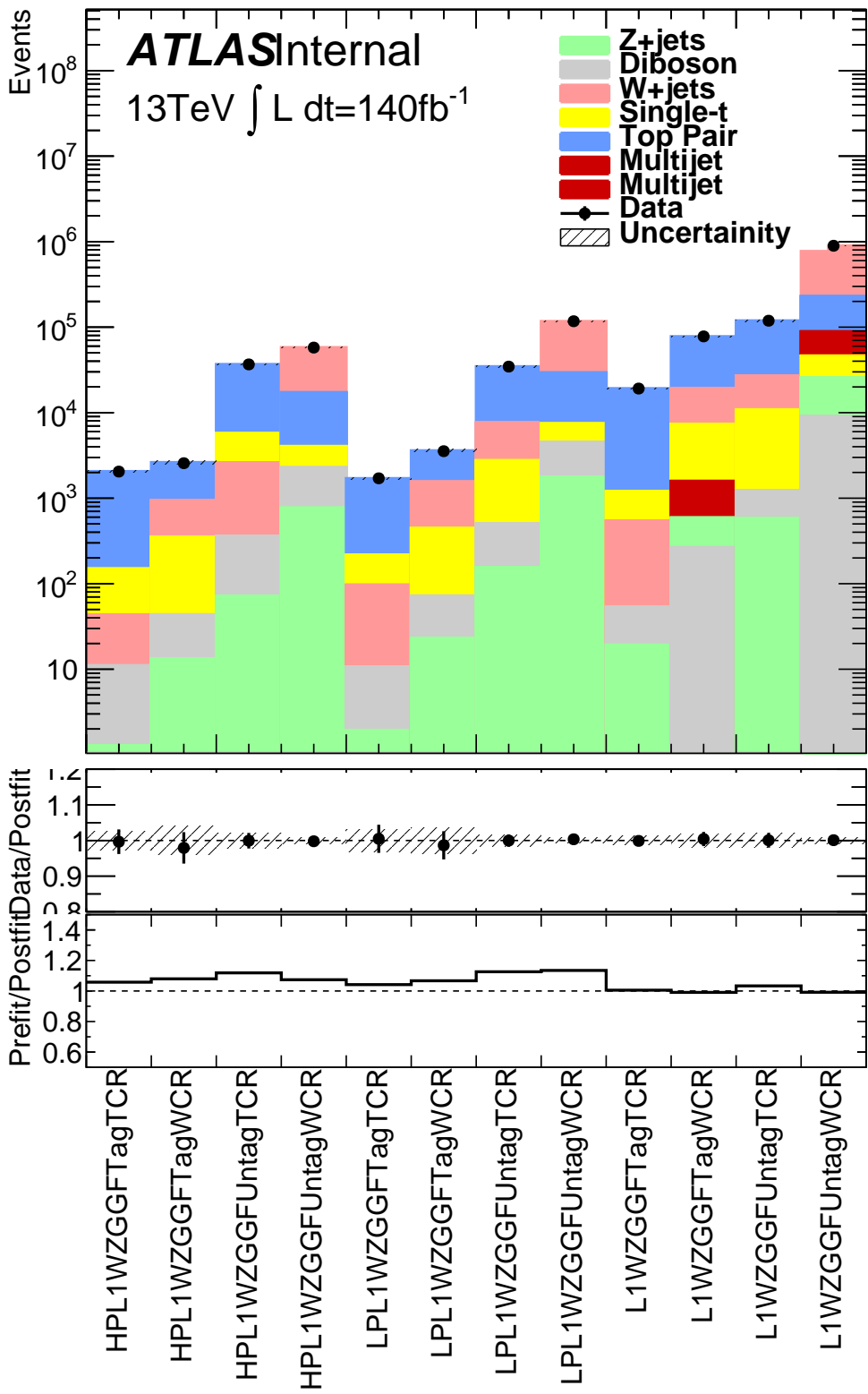


Figure 10.10: This figure shows the distribution of $m_{\ell\nu qq}$ in the DY WZ control regions.

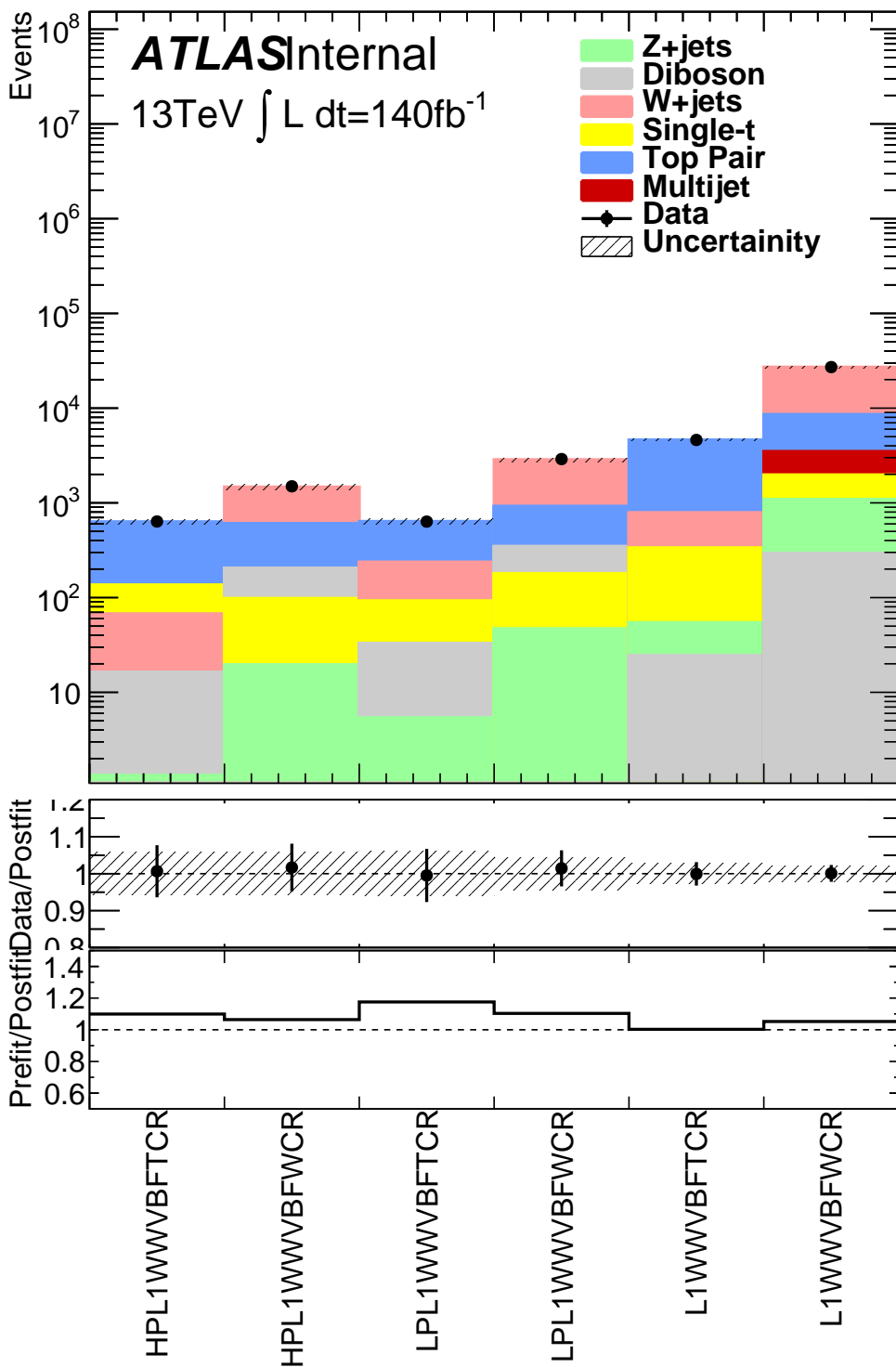


Figure 10.11: This figure shows the distribution of $m_{\ell\nu qq}$ in the VBF WW control regions.

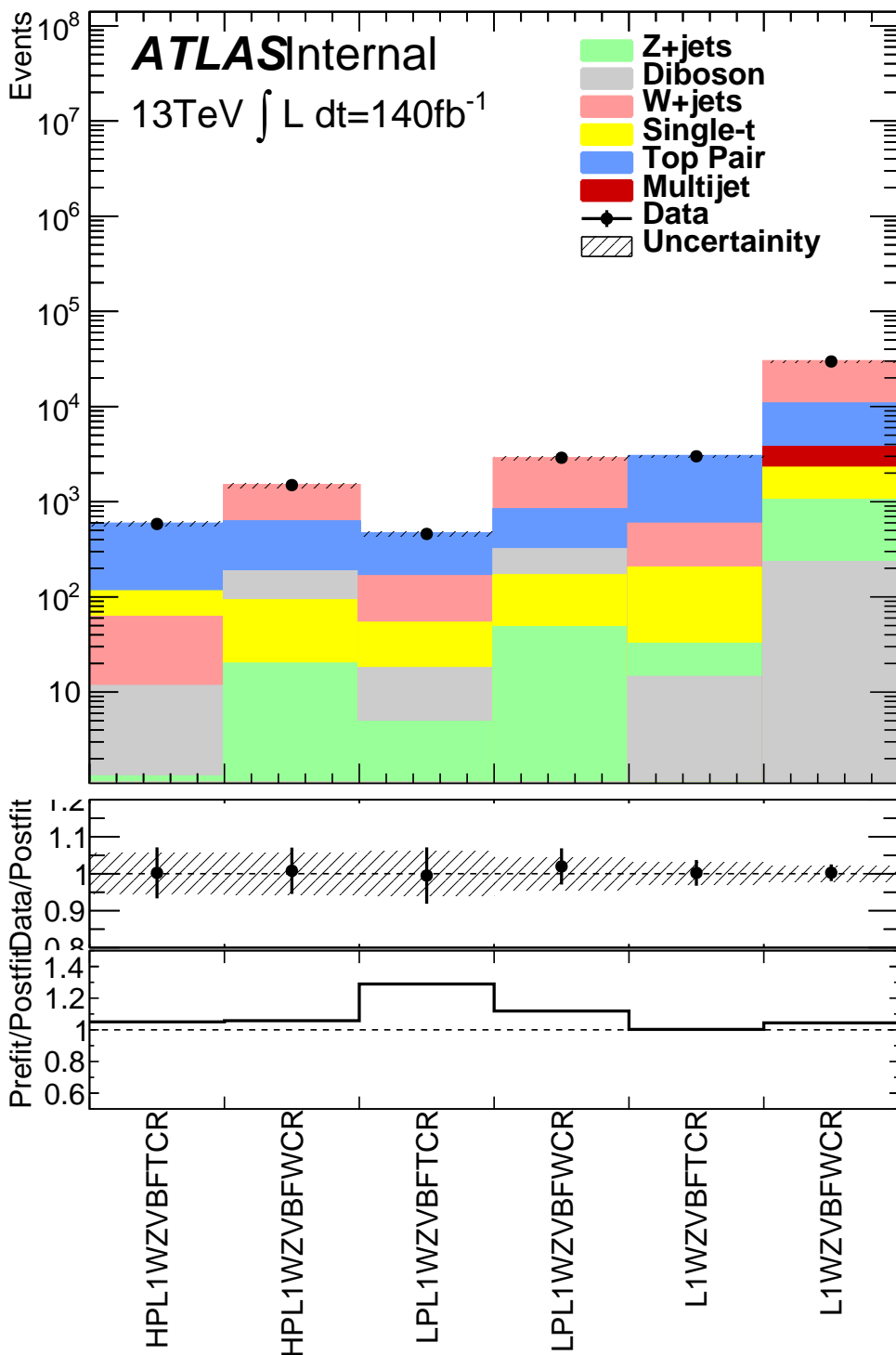


Figure 10.12: This figure shows the distribution of $m_{\ell\nu qq}$ in the VBF WZ control regions.

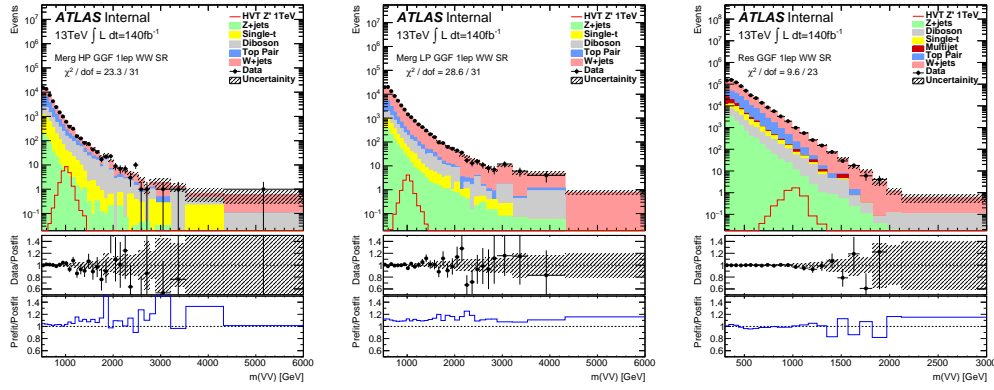


Figure 10.13: This figure shows the distribution of $m_{\ell\nu qq}$ in the GGF WW signal regions.

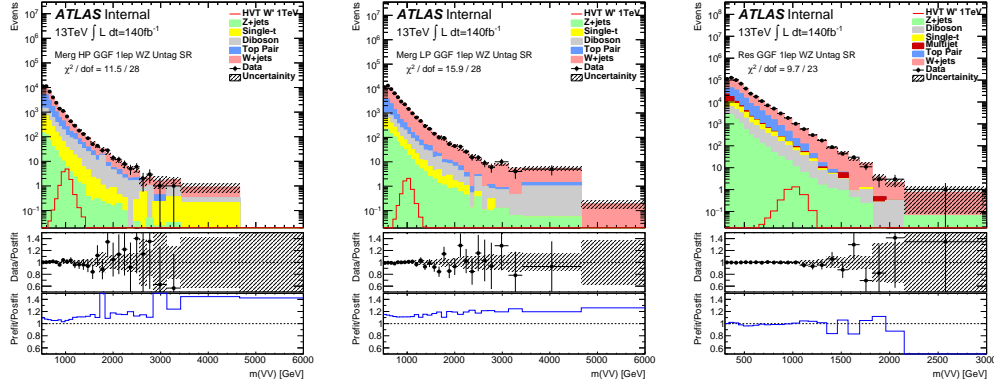


Figure 10.14: This figure shows the distribution of $m_{\ell\nu qq}$ in the GGF WZ Untag signal regions.

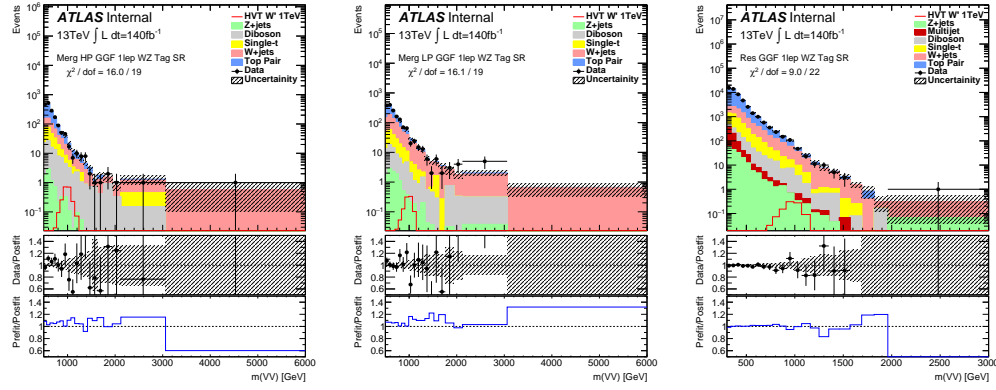


Figure 10.15: This figure shows the distribution of $m_{\ell\nu qq}$ in the GGF WZ Tag signal regions.

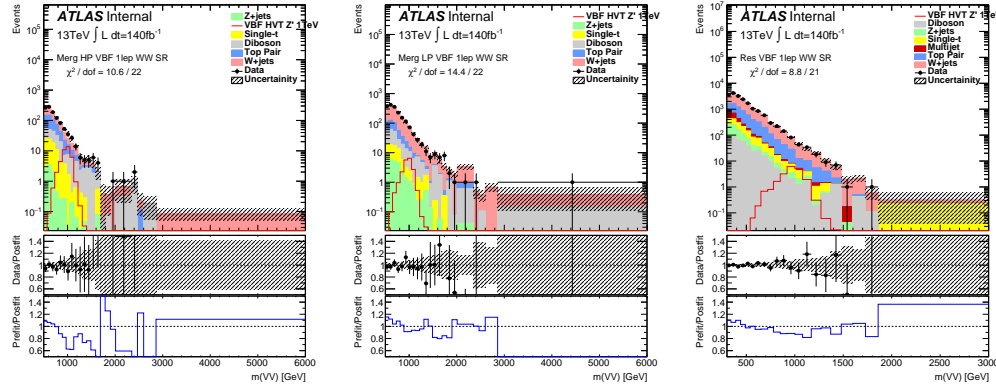


Figure 10.16: This figure shows the distribution of $m_{\ell\nu qq}$ in the VBF WZ Tag signal regions.

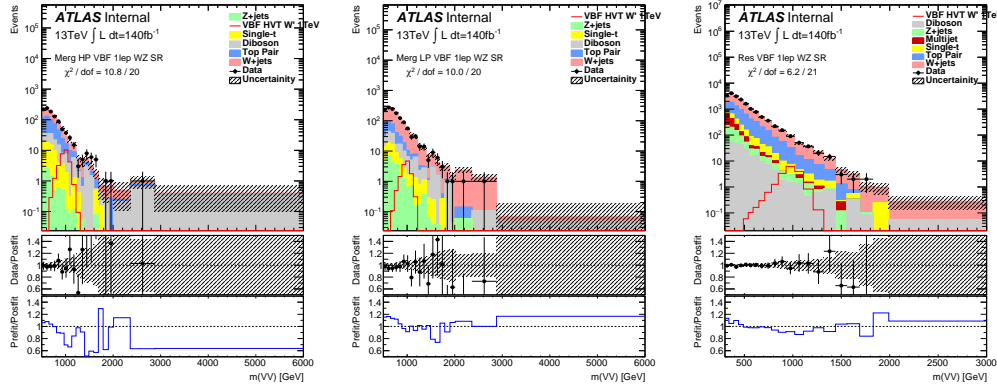


Figure 10.17: This figure shows the distribution of $m_{\ell\nu qq}$ in the VBF WZ Tag signal regions.

1189 10.4 Limits

1190 Using the exclusion limits tests discussed previously, exclusion limits are set
 1191 on μ and consequently cross-sections for different signal models. Exclusion limits
 1192 for the models considered are shown in Figure 10.18 - 10.20. These limits exclude
 1193 HVT Model A $W' < \text{blah}$ and $Z' < \text{blah}$ and Model B $W' < \text{blah}$ and $Z' < \text{blah}$.
 1194 Randall Sundrum Gravitons are excluded for masses below blah.

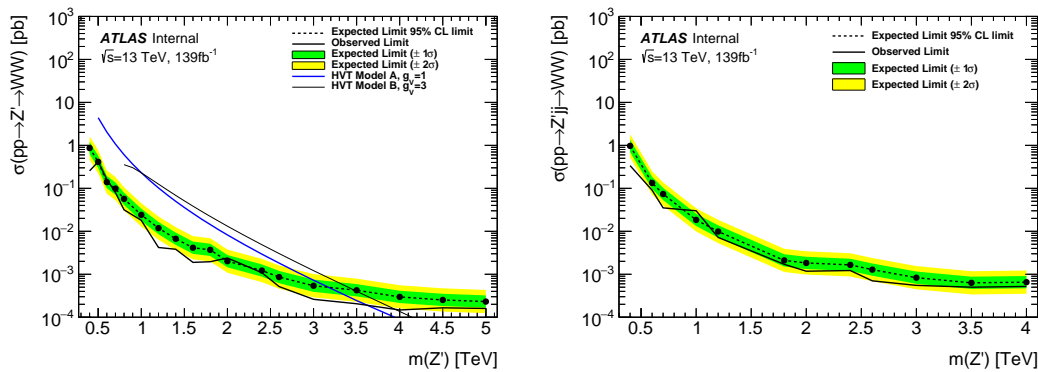


Figure 10.18: This figure shows theory, expected and observed limits for HVT W' DY (left) and VBF (right) production.

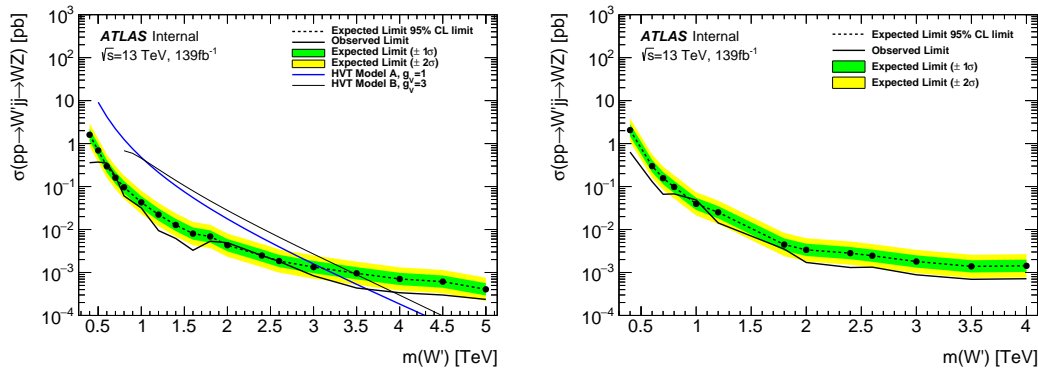


Figure 10.19: This figure shows theory, expected and observed limits for HVT Z' DY (left) and VBF (right) production.

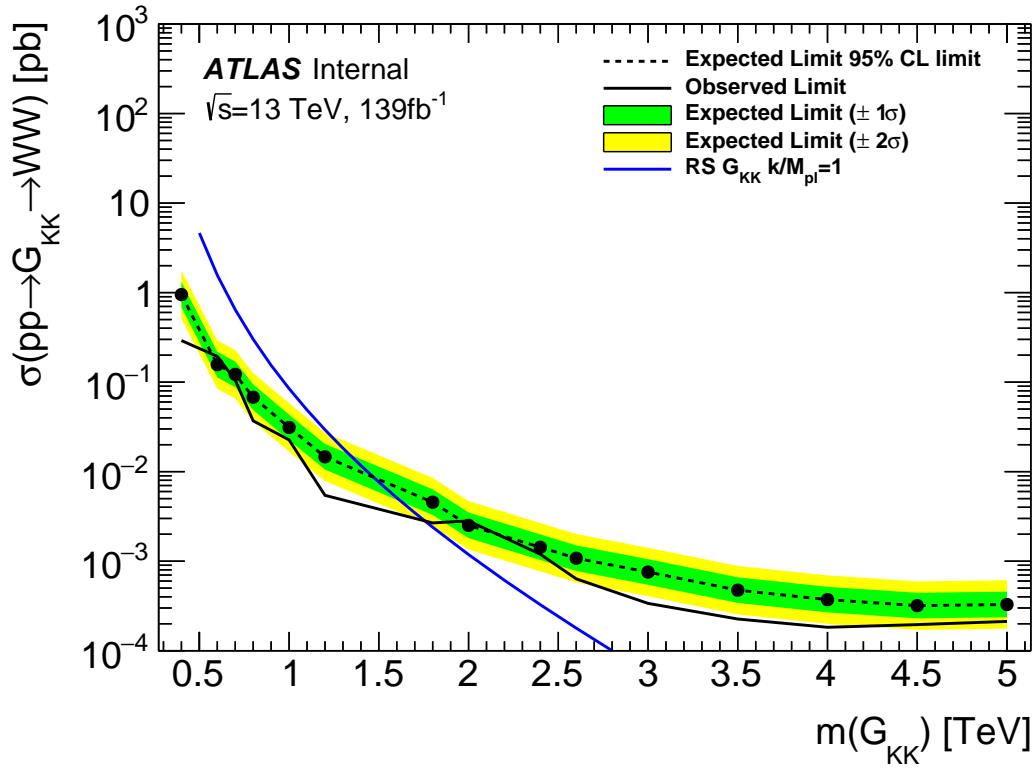


Figure 10.20: This figure shows theory, expected and observed limits for RS Gravitons via DY production.

Part V

1195

Quark and Gluon Tagging

1196

₁₁₉₇ **Chapter 11**

₁₁₉₈ **Prospects**

₁₁₉₉ For the resolved analysis, signal jets are quark enriched and background jets are
₁₂₀₀ gluon dominated. By classifying jets in the event as quark or gluon initiated, less
₁₂₀₁ background would contaminate the signal region. Figure 11.1 shows the PDGID
₁₂₀₂ for the truth parton matched to the jet (meaning the highest energy parton in
₁₂₀₃ the jet catchment area) in events passing the resolved signal region selections.
₁₂₀₄ PDGID = -1 corresponds to pileup jets, $0 < \text{PDGID} < 6$ correspond to quarks
₁₂₀₅ and $\text{PDGID} = 21$ corresponds to gluons. From this Figure, it is evident that a
₁₂₀₆ notable fraction of the background that contaminates the signal region contains
₁₂₀₇ gluon jets, especially for the sub-leading jet.

₁₂₀₈ As gluons jets have more constituents and therefore more tracks (n_{trk}), the
₁₂₀₉ background jets have more tracks than the signal jets. This is shown in Fig-
₁₂₁₀ ure 11.2. Therefore, by cutting on the number of tracks in a jet, quark and gluon
₁₂₁₁ jets may be distinguished (i.e. jets with less than a given number of tracks are
₁₂₁₂ classified as a quark, otherwise the jet is classified as a gluon.) Moreover, as the
₁₂₁₃ momentum of the jet increases the number of tracks also increases logarithmically
₁₂₁₄ [Cite nachman thesis Natasha]. Therefore by applying a cut on the number of
₁₂₁₅ tracks that scales with the $\ln(p_T)$ is more powerful than a threshold cut on the

1216 number of tracks. Figure 11.3-Figure 11.6 show normalized heat maps of $\ln(p_T)$
1217 vs the number of reconstructed tracks for the background and a 300 GeV Z' signal.
1218 In these plots it is evident that the number of tracks in the background jets grows
1219 more quickly with $\ln(p_T)$ than for the signal jets. This is expected given that the
1220 signal is quark dominated and the background is gluon dominated.

1221 In Figure 11.8 is the ROC Curve for quark gluon tagging with cut on the
1222 number of tracks in a jet that depends on $\ln(p_T)$. The sum of the backgrounds in
1223 the signal region were used for this curve. Here the quark tagging efficiency is the
1224 ratio of quarks tagged as quarks to the total number of quarks in the signal region.
1225 The gluon rejection is calculated as the reciprocal of the gluon tagging efficiency.
1226 Choosing a 90% efficient working point with a rejection of 1.4 corresponds to a
1227 slope of 4 and intercept of -5. Tagging both jets in this analysis would yield an
1228 efficiency of $90\%^{n_{jets}}$. Focusing on the background in Figure 11.9, this cut helps
1229 minimize gluon contamination in the signal region. Also, from these heat maps it
1230 is obvious that the number of tracks in gluon jets grows more quickly than those
1231 in quark jets.

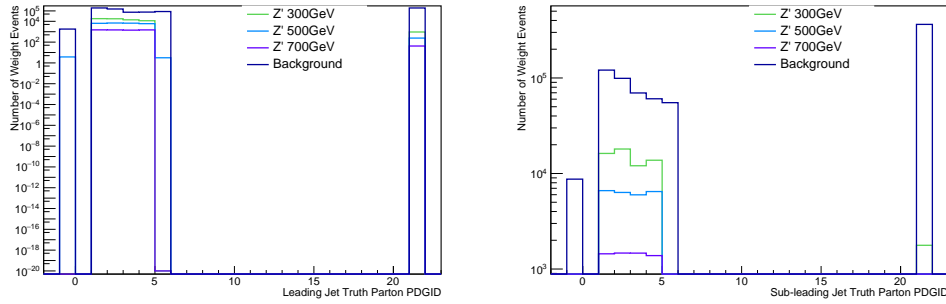


Figure 11.1: PDGID of the truth-level parton matched to the small-R jets passing the Resolved GGF WW Signal Region selections for the (a) Leading (b) Sub-Leading jets . These distributions are shown for 300, 500, and 700GeV Z' signals and the background.

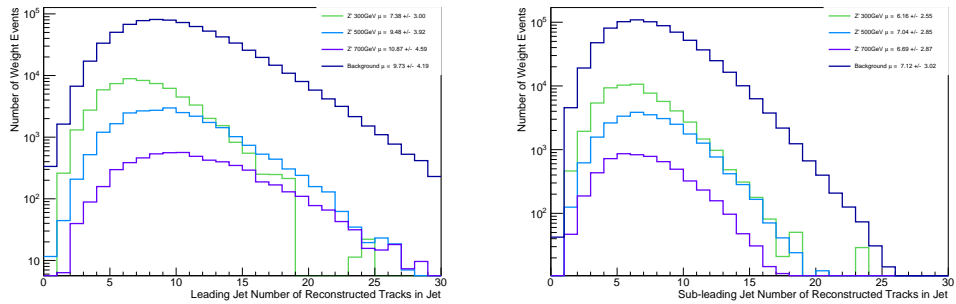


Figure 11.2: The number of tracks in small-R jets in events passing the Resolved GGF WW Signal Region selections for the (a) Leading (b) Sub-Leading jets. These distributions are shown for 300, 500, and 700GeV Z' signals and the background.

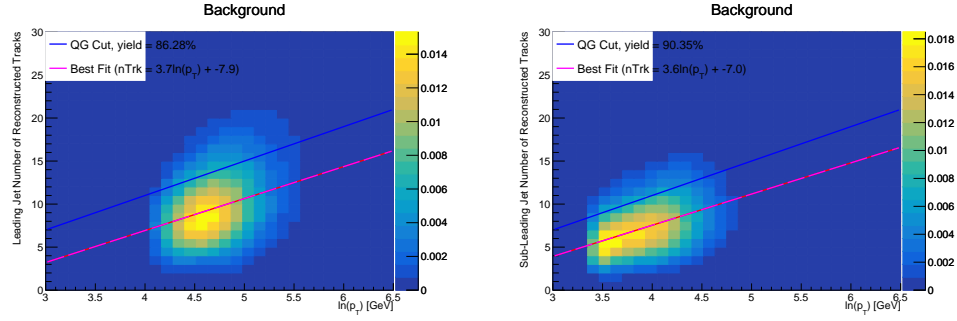


Figure 11.3: The number of tracks in background small-R jets in events passing the Resolved GGF WW Signal region selection vs. $\ln(p_T)$ for (a)Leading (b) Sub-Leading jets. The best fit line for the distribution is also shown, as well as the percentage of jets that pass a cut of number of tracks $< 4 \times \ln(p_T) - 5$. Note the number of total entries in these plots has been normalized to one.

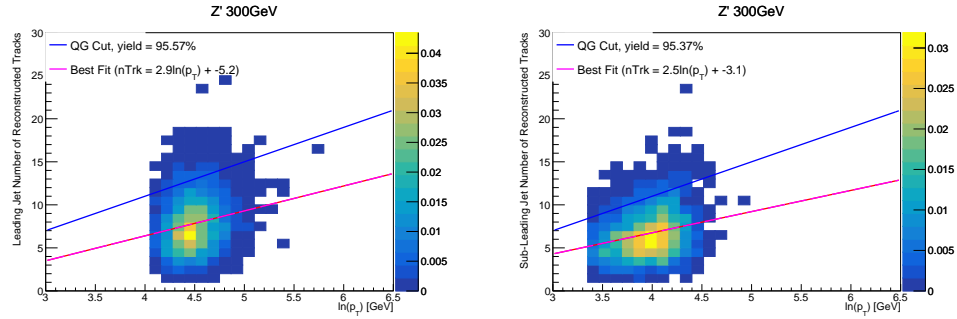


Figure 11.4: The number of tracks in small-R jets in 300GeV Z' events passing the Resolved GGF WW Signal region selection vs. $\ln(p_T)$ for (a)Leading (b) Sub-Leading jets. The best fit line for the distribution is also shown, as well as the percentage of jets that pass a cut of number of tracks $< 4 \times \ln(p_T) - 5$. Note the number of total entries in these plots has been normalized to one.

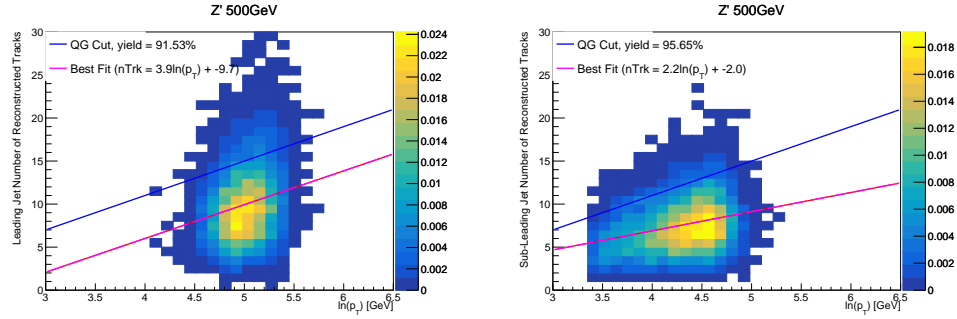


Figure 11.5: The number of tracks in small-R jets in 500GeV Z' events passing the Resolved GGF WW Signal region selection vs. $\ln(p_T)$ for (a)Leading (b) Sub-Leading jets. The best fit line for the distribution is also shown, as well as the percentage of jets that pass a cut of number of tracks $< 4 \times \ln(p_T) - 5$. Note the number of total entries in these plots has been normalized to one.

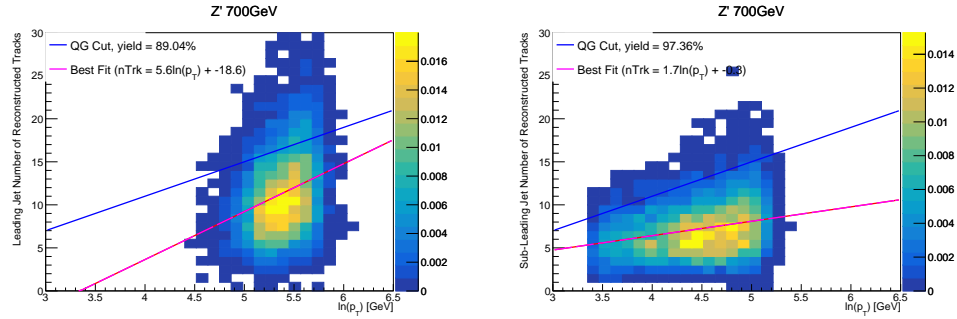


Figure 11.6: The number of tracks in small-R jets in 700GeV Z' events passing the Resolved GGF WW Signal region selection vs. $\ln(p_T)$ for (a)Leading (b) Sub-Leading jets. The best fit line for the distribution is also shown, as well as the percentage of jets that pass a cut of number of tracks $< 4 \times \ln(p_T) - 5$. Note the number of total entries in these plots has been normalized to one.

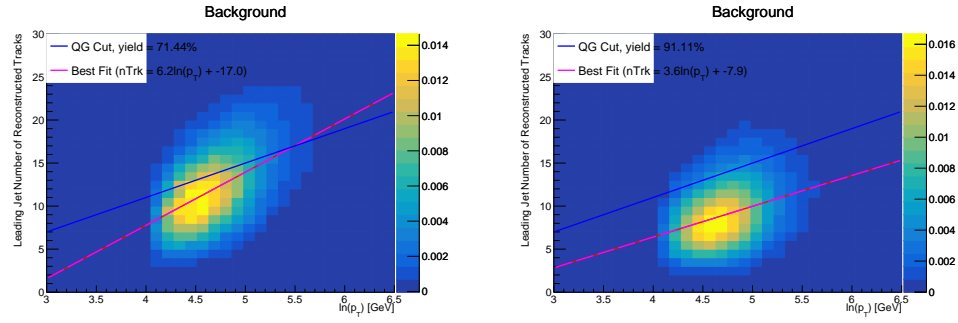


Figure 11.7: The number of tracks in leading small-R jets in background events passing the Resolved GGF WW Signal region selection vs. $\ln(p_T)$ for (a)Gluons (b) Quarks jets. The best fit line for the distribution is also shown, as well as the percentage of jets that pass a cut of number of tracks $< 4 \times \ln(p_T) - 5$.Note the number of total entries in these plots has been normalized to one.

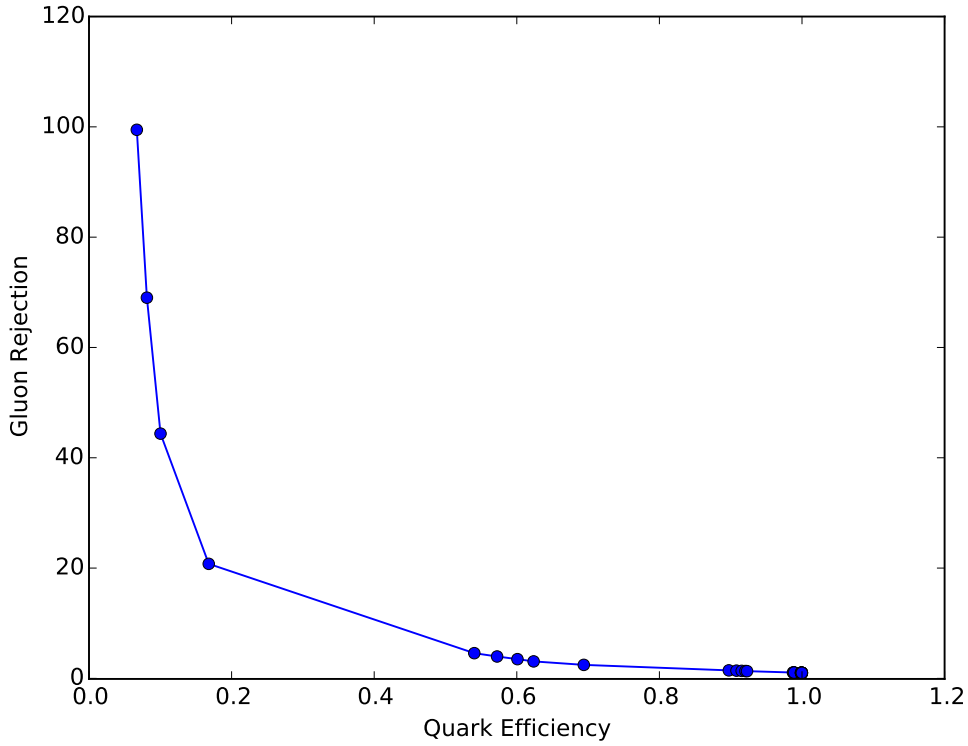


Figure 11.8: ROC Curve for Quark and Gluon Tagging with a cut on the number of tracks that depends on the $\ln(p_T)$.

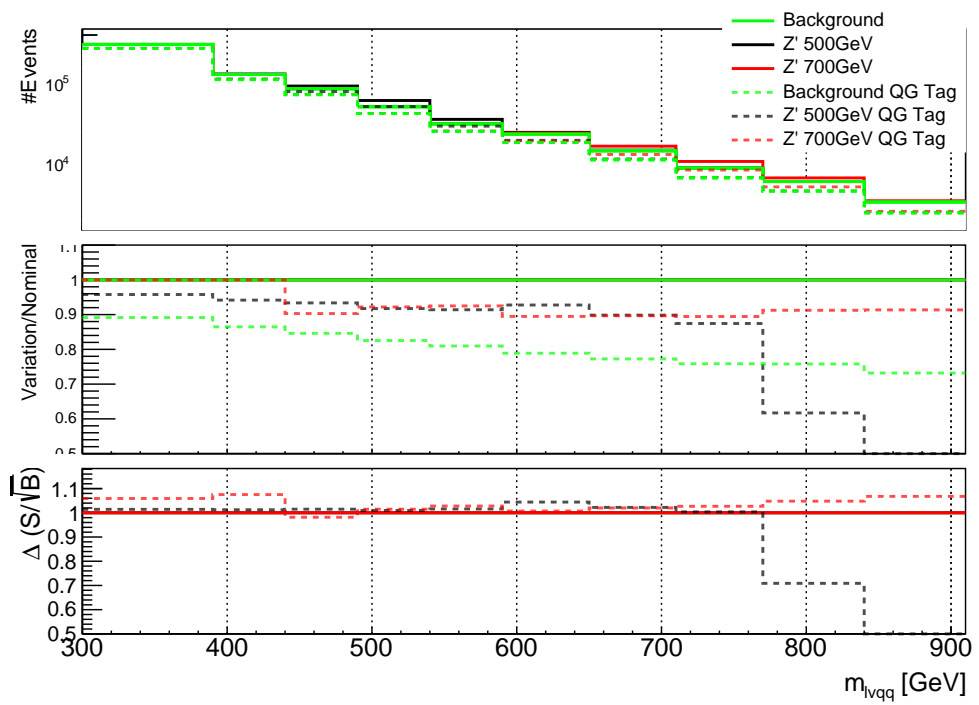


Figure 11.9: The top panel shows the distribution of m_{lvqq} with and without quark gluon tagging. The middle panel shows the ratio of the signals and backgrounds with and without quark gluon tagging. The bottom panel shows the change in S/\sqrt{B} with quark gluon tagging.

1232 Chapter 12

1233 n_{trk} Calibration

1234 As tagger based on nTrk cuts on the number of tracks in jets, a quantity that
1235 is not known with infinite precision, means that relevant systematic uncertainties
1236 must be evaluated. The sources of uncertainty in n_{trk} may be split into modeling
1237 and experimental uncertainties.

1238 Modeling uncertainties are obtained by assessing PDF and ME uncertainties
1239 on the number of charged particles in particle-level jets in dijet events. The
1240 number of charged particles as a function of jet p_T is calculated using an Iterative
1241 Bayesian (IB) technique [cite paper].

1242 This measurement ([7]) uses the ATLAS 2012 pp collision dataset, correspond-
1243 ing to $20.3/\text{fb}$ at center-of-mass energy $\sqrt{s} = 8\text{TeV}$. The number of charged con-
1244 stituents depends on fragmentation modeling and matrix elements, which do not
1245 depend on s . For this reason, it is safe to use these uncertainties for $\text{sqrt}(s)=13\text{TeV}$.
1246 Monte Carlo (MC) samples are used to determine the response matrix. The MC
1247 sample is a dijet sample generated with Pythia 8.175 using CT10 PDF and AU2
1248 tune. The anti- k_T algorithm is used to cluster jets with a radius parameter R
1249 $= 0.4$. Jets are required to have $|\eta| < 2.1$. Tracks in jets are required to have
1250 $p_T > 500\text{MeV}$, $|\eta| < 2.5$, track-fit $\chi^2 < 3.0$ and originate from the primary ver-

tex. Matching tracks to jets is accomplished using ghost-association [cite]. In this technique, jets are re-clustered with the track collection augmented with "ghost" versions of tracks. These "ghosts" tracks have the same direction as their parent track, but infinitesimal track p_T . This insures meta-jet properties (e.g. η , p_T , etc) are unchanged. A track is matched to a jet if it's ghost version remains in the jet after re-clustering. Further details of the data, object, and event selection may be found in [cite 35].

To select dijet topologies events are required to have at least two jets with $p_T > 50GeV$ that are relatively well-balanced ($p_T^{lead}/p_T^{sub-lead} < 1.5$).

In the IB technique, the prior distribution and number of iterations are the inputs [cite Bayesian paper]. The IB response matrix connects number of charged particles to the number of tracks in jets determined using the simulated samples. This response matrix is used to unfold data to extract the n_c . Before applying the response matrix a fake factor is applied. This accounts for jets that pass detector level selections, but not particle level selections. Following this, the IB method iteratively applies the response matrix using the nominal Pythia 8.175 sample as a prior. The number of IB iterations is chosen to minimize unfolding bias and statistical fluctuations. For this measurement four iterations was found to be optimal by minimizing the unfolding bias from pseudodata simulated with Herwig++ with a prior from Pythia 8 AU2. Finally, the inefficiency factor is applied to account for events passing particle level selection but not detector level, yielding the unfolded nCharged distribution.

This process is prone to three main sources of bias: response matrix, correction factor, and unfolding procedure uncertainties. The response matrix is sensitive to experimental uncertainties impacting jet track reconstruction and calorimeter jet p_T . Correction factors are also sensitive to experimental uncertainties (e.g. JES)

1277 as such uncertainties modify detector level acceptance. Sensitivity to particle
 1278 level acceptance is calculated by comparing Pythia and Herwig. Finally, the bias
 1279 from the IB prior choice is determined by reweighting the particle-level spectrum,
 1280 so the simulated detector level spectrum more closely matches the uncorrected
 1281 data. Unfolding this modified detector-level simulation and comparing it to the re-
 1282 weighted particle-level spectrum indicates bias from the prior distribution choice.
 1283

1283 A summary of all the systematic uncertainties associated with this unfolding
 1284 may be found in [ref paper]. Total uncertainties are < 7% for the number of
 1285 charged particles in jets. The unfolded distribution of the nCharged in jets from
 1286 data are further analyzed to extract the quark and gluon nCharged distributions.
 1287 In dijet events, the jet with a larger η is more energetic and therefore more likely
 1288 to be a quark. This is due to the quarks in protons generally having a larger
 1289 fraction of the total momentum of the proton constituents. The more central jet
 1290 is more likely to be a gluon-initiated jet. This correlation between jet η and flavor
 1291 may then be used to extract nCharged in p_T bins using:
 1292

$$\langle n_c^f \rangle = f_q^f \langle n_c^q \rangle + f_g^f \langle n_c^g \rangle \quad (12.1)$$

$$\langle n_c^c \rangle = f_q^c \langle n_c^q \rangle + f_g^c \langle n_c^g \rangle \quad (12.2)$$

1293 In this equation the f and c subscripts denote the more forward and central
 1294 jets, respectively. The q and g subscripts denote quark and gluon. The fraction
 1295 of more forward jets that are say gluons is denoted by f_g^f . The other relevant jet
 1296 fractions are denoted with the same naming scheme. Finally, $\langle n_c \rangle$ is the average
 1297 number of charged particles in a jet in a given p_T bin. To show that Eq. (??) may
 1298 be used to extract quark and gluon n_c distributions the extracted distributions
 1299 are compared to n_c distributions determined using the jet flavor in simulation.
 1300 Figure [add figure natasha] shows that the extracted and true distributions differ

1301 by < 1% over the p_T range probed for this study. Moreover, this implies that n_c
1302 depends only on the flavor of the initiating parton and jet p_T .

1303 These extracted distributions are prone to PDF and ME biases. The bias from
1304 the choice of the CT10 PDF for the Pythia sample is accounted for by comparing
1305 quark/gluon fractions for the nominal CT10 sample with its eigenvector variations.
1306 Comparing the quark/gluon fractions from Pythia 8 and Herwig++ quantify the
1307 uncertainty from the ME calculation. These uncertainties are added in quadra-
1308 ture with the unfolding uncertainty to give the total modelling uncertainty on
1309 the extracted n_c distribution. This is shown in Figure 13.2.

1310 To apply these uncertainties in n_c distributions in data, per-jet event weights
1311 are associated with each uncertainty according to:

$$w_i(n_c) = \frac{P(n_c | n_c > \pm \sigma_{n_c}^i)}{P(n_c | n_c >)} \quad (12.3)$$

1312 In Eq. (??), i denotes the uncertainty considered, P is the Poisson probability,
1313 and $\sigma_{n_c}^i$ represents the average impact of the uncertainty on n_c .

1314 The previous uncertainties described accounted for modeling uncertainty as-
1315 sociated with the number of charged particles in a jet. However, n_c is not a
1316 measurable quantity. Instead the number of tracks in a jet is measured, which is
1317 a proxy for n_c . Therefore the uncertainties associated with the measurement of
1318 nTracks must also be considered ([9]). These uncertainties were calculated using
1319 a Pythia 8 dijet sample with NNPDF 23 and Run 2 data. Track reconstruction
1320 efficiency and fake rates are the dominant sources of nTrack uncertainties.

1321 The track reconstruction efficiency is affected by the uncertainty of the de-
1322 scription of the ID material in simulation and the modeling of charged-particle
1323 interactions with this material. These uncertainties are accounted for by varying
1324 the ID material by 5-25% (dependent on the region of the detector considered).

1325 The difference in the tracking efficiency between the nominal and varied simula-
1326 tion give the uncertainty on the track reconstruction efficiency. Another important
1327 source of track reconstruction inefficiency arises in the core of jets. The high den-
1328 sity of tracks in the jet cores can cause ID clusters to merge. The fraction of lost
1329 tracks due to merging is given by the fraction of tracks that have a charge of two
1330 minimum ionizing particles. This quantity is compared between data and simu-
1331 lation resulting in an uncertainty of 0.4% on tracks with $\Delta R < 0.1$. Combining
1332 these effects gives a total uncertainty as a function of p_T and η that is generally
1333 $< 2\%$ [references figure 44 from [9]).

1334 Fake tracks are the other dominant source of nTrk uncertainty. Fake tracks
1335 are tracks that cannot be associated to a single particle. Often these tracks are a
1336 result of random combinations of hits from charged particles that overlap in space.
1337 In dense environments, such as the core of jets or high-pileup environments, fake
1338 tracks are more likely. Fake tracks are estimated with a 'control region method'
1339 which is briefly summarized here [[8]]. By applying a series of track selections
1340 to enrich the fraction of fake tracks (e.g. $|d_0| > 0.1$, track $\chi^2 > 1.4$, etc) in
1341 simulation, templates for fake track parameters are calculated. These templates
1342 are then fit to data to determine the fraction of fake tracks. On average the fake
1343 rate is found to be 30% (independent of p_T and η).

1344 To assess the impact of these two detector level uncertainties, tracks are ran-
1345 domly dropped according to the rates described above. Reconstruction and fake
1346 uncertainties both lower the number of tracks, hence these uncertainties are one-
1347 sided. By dropping tracks in this way a varied nTrk distribution is calculated for
1348 both uncertainties. The associated per-jet event weights are then calculated in
1349 the same way as the modeling weights as:

$$w_i(n_c) = \frac{P(n_{trk} | < n_{trk} > \pm \sigma_{n_{trk}}^i)}{P(n_{trk} | < n_{trk} >)} \quad (12.4)$$

1350 Adding the modeling and detector level uncertainties in quadrature gives the
 1351 overall nTrack uncertainty. The effects of the individual uncertainties on the nTrk
 1352 distributions can be seen in Fig 13.4. Fig 13.3 shows the m_{lvqq} and nTrk distri-
 1353 butions for the W and Top control regions before likelihood fitting. In these plots
 1354 the nTrk uncertainties improve agreement between data and MC. The remaining
 1355 differences are likely covered by likelihood fitting and improving the analysis itself.

₁₃₅₆ **Chapter 13**

₁₃₅₇ **Application**

₁₃₅₈ Using the 90% WP of the n_{trk} tagger improves S/\sqrt{B} is $\sim 3\%$ as shown in
₁₃₅₉ Figure 11.9. Although, n_{trk} is the single most powerful discriminating variable
₁₃₆₀ for quark and gluon jets, the addition of other jet variables would improve the
₁₃₆₁ classification efficiency. Figure 13.1 shows the possible improvement of 10%
₁₃₆₂ in jet classification using the truth label of the jets to classify jets. This type of
₁₃₆₃ improvement is possible by using variables such as jet width, and energy correlata-
₁₃₆₄ tors. Figure [add BDT figure/use 1612.01551.pdf] shows for a 90% quark tagging
₁₃₆₅ efficiency for a 100 GeV jet, a BDT improve the gluon rejection by 0.4. Once this
₁₃₆₆ tagger is calibrated it would improve the analysis sensitivity of this channel.

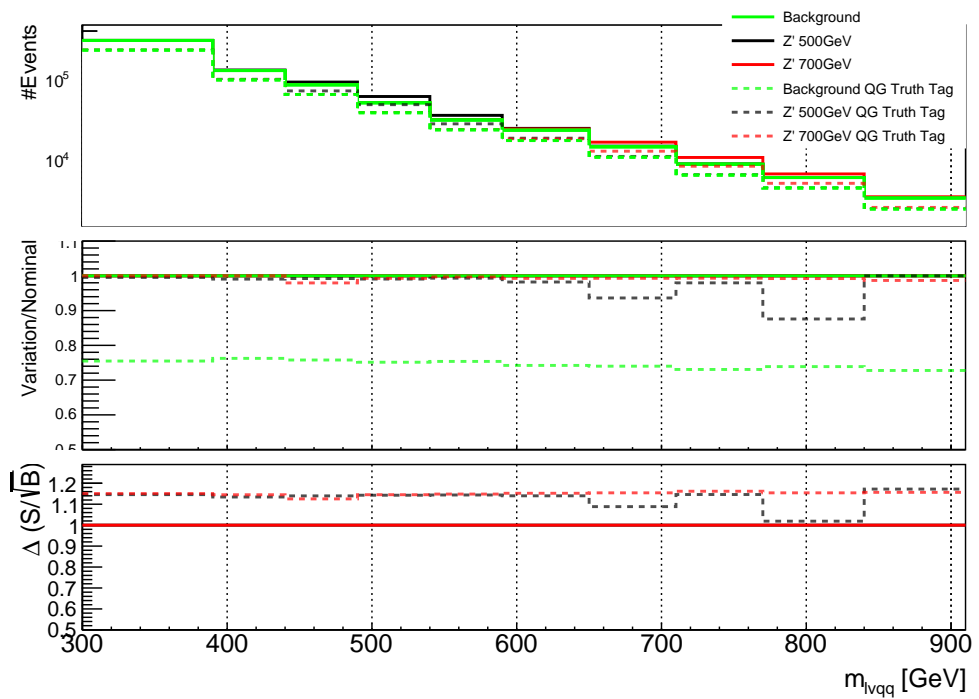


Figure 13.1: The top panel shows the distribution of m_{lvqq} with and without requiring jets to be true quarks. The middle panel shows the ratio of the signals and backgrounds with and without requiring jets to be true quarks. The bottom panel shows the change in S/\sqrt{B} when requiring jets to be true quarks..

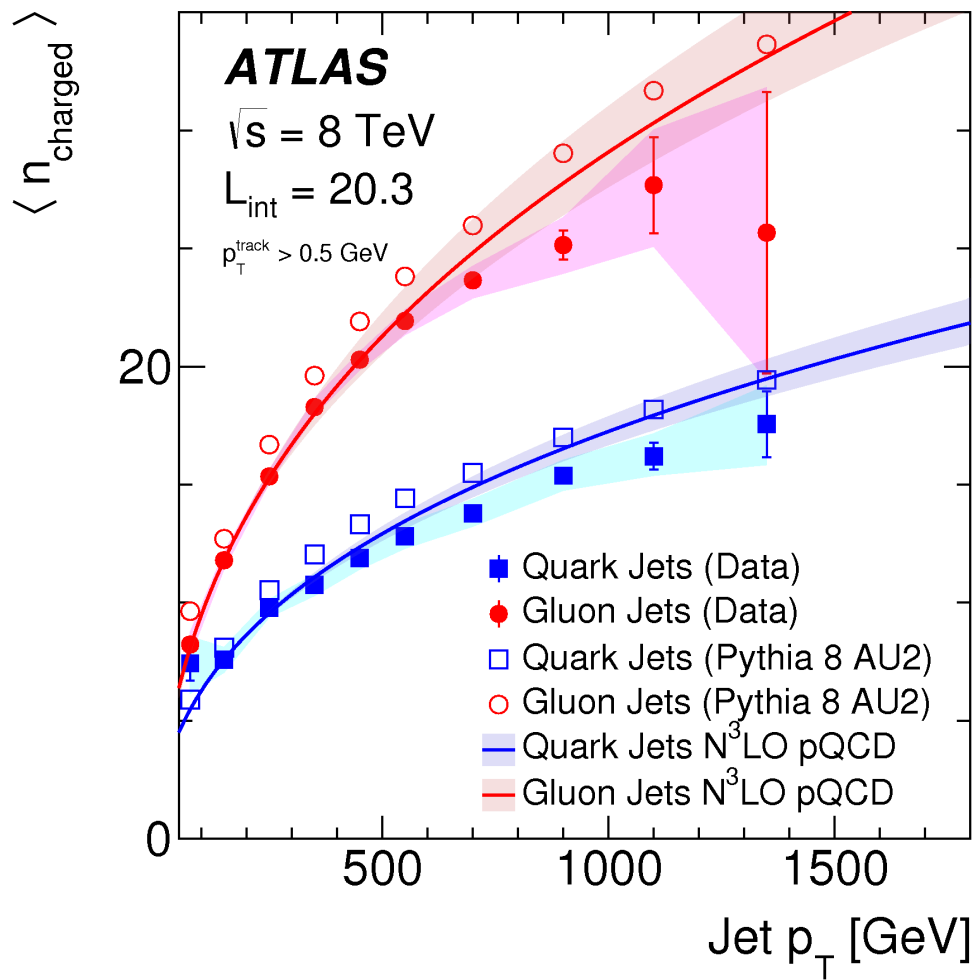


Figure 13.2: Unfolded and extracted n_C qg dstbs..

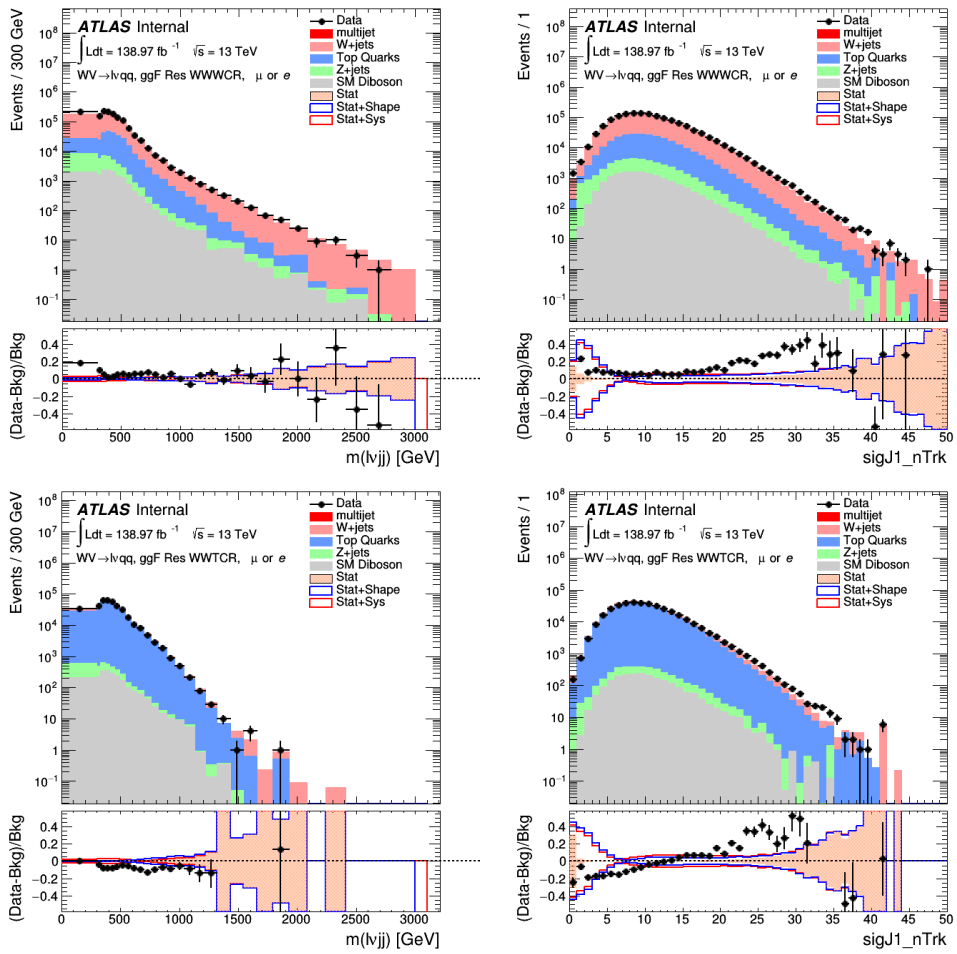


Figure 13.3: PDGID of the truth-level parton matched to the small-R jets passing the Resolved GGF WW Signal Region selections for the (a) Leading (b) Sub-Leading jets . These distributions are shown for 300, 500, and 700GeV Z' signals and the background.

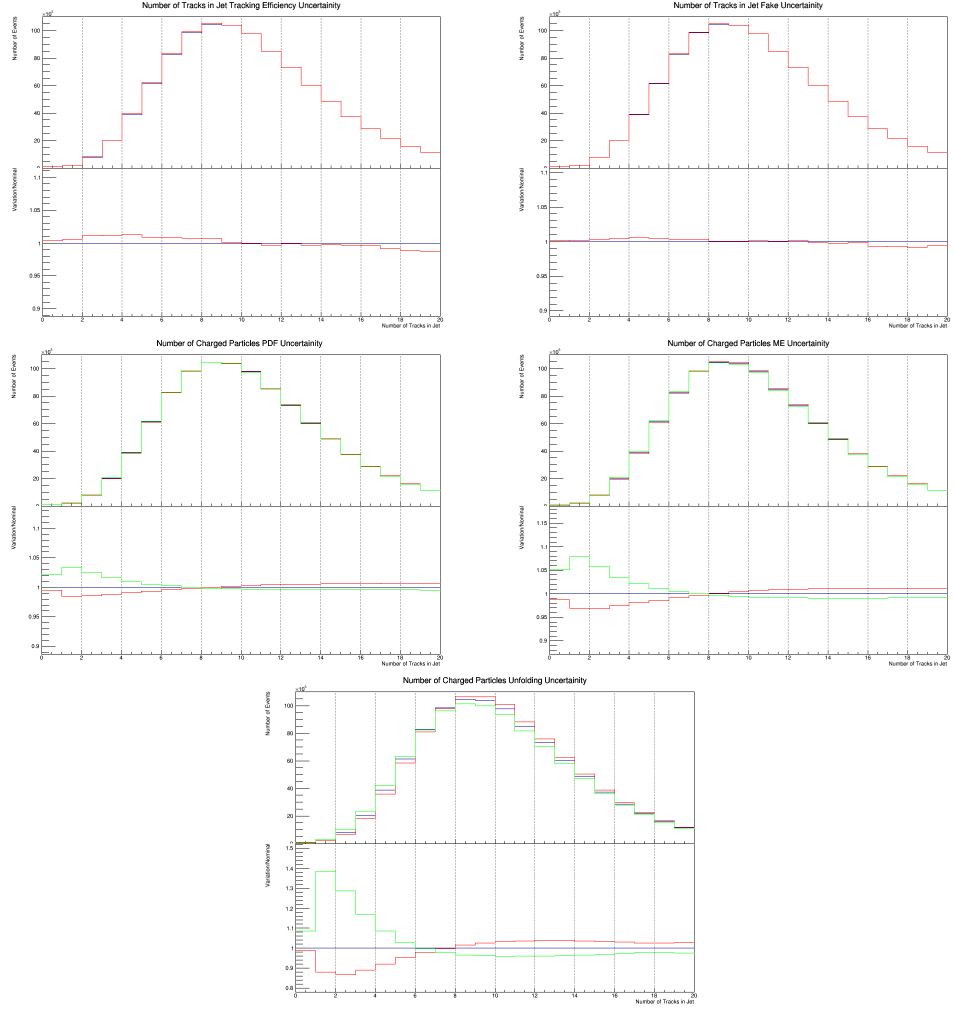


Figure 13.4: These figures show the impact of the uncertainties on the number of tracks in the leading jet in the sum of the background sample in the Resolved GGF WW SR (a) tracking efficiency (b) fake (c) PDF (d) ME (e) unfolding uncertainties.

Part VI

1367

Conclusion

1368

₁₃₆₉ **Chapter 14**

₁₃₇₀ **Conclusions**

₁₃₇₁ This is where I am going to add my final thoughts.

¹³⁷² Bibliography

- ¹³⁷³ [1] Lecture notes particle physics ii.
- ¹³⁷⁴ [2] Kaustubh Agashe, Hooman Davoudiasl, Gilad Perez, and Amarjit Soni.
¹³⁷⁵ Warped Gravitons at the LHC and Beyond. *Phys. Rev.*, D76:036006, 2007.
- ¹³⁷⁶ [3] G. Altarelli and G. Parisi. Asymptotic freedom in parton language. *Nuclear*
¹³⁷⁷ *Physics B*, 126(2):298 – 318, 1977.
- ¹³⁷⁸ [4] ATLAS Collaboration. Atlas muon reconstruction performance in lhc run 2.
- ¹³⁷⁹ [5] ATLAS Collaboration. Summary plots from the atlas standard model physics
¹³⁸⁰ group.
- ¹³⁸¹ [6] ATLAS Collaboration. Jet energy scale measurements and their systematic
¹³⁸² uncer- tainties in proton–proton collisions at $\sqrt{s} = 13$ tev with the atlas
¹³⁸³ detector. arXiv: 1703.09665 [hep-ex].
- ¹³⁸⁴ [7] ATLAS Collaboration. Measurement of the charged-particle multiplicity
¹³⁸⁵ inside jets from $s=\sqrt{8}$ tev pp collisions with the atlas detector.
¹³⁸⁶ arXiv:1602.00988 [hep-ex].
- ¹³⁸⁷ [8] ATLAS Collaboration. Performance of the atlas track reconstruction algo-
¹³⁸⁸ rithms in dense environments in lhc run 2. arXiv:1704.07983 [hep-ex].
- ¹³⁸⁹ [9] ATLAS Collaboration. Properties of jet fragmentation using charged par-
¹³⁹⁰ ticles measured with the atlas detector in pp collisions at $\sqrt{s} = 13$ tev.
¹³⁹¹ arXiv:1906.09254 [hep-ex].
- ¹³⁹² [10] Alex Dias and V. Pleitez. Grand unification and proton stability near the
¹³⁹³ peccei-quinn scale. *Physical Review D*, 70, 07 2004.
- ¹³⁹⁴ [11] Stefan Höche, Frank Krauss, Marek Schönherr, and Frank Siegert. Qcd ma-
¹³⁹⁵ trix elements + parton showers. the nlo case. *Journal of High Energy Physics*,
¹³⁹⁶ 2013(4), Apr 2013.
- ¹³⁹⁷ [12] Gregory Soyez Matteo Cacciari, Gavin P. Salam. The anti- k_T jet clustering
¹³⁹⁸ algorithm. arXiv:0802.1189 [hep-ph].

- 1399 [13] Duccio Pappadopulo, Andrea Thamm, Riccardo Torre, and Andrea Wulzer.
1400 Heavy vector triplets: bridging theory and data. *Journal of High Energy*
1401 *Physics*, 2014(9), Sep 2014.
- 1402 [14] Antonio Pich. The Standard Model of Electroweak Interactions. In *Proceed-
1403 ings, High-energy Physics. Proceedings, 18th European School (ESHEP 2010):
1404 Raseborg, Finland, June 20 - July 3, 2010*, pages 1–50, 2012. [,1(2012)].
- 1405 [15] Lisa Randall and Raman Sundrum. A Large mass hierarchy from a small
1406 extra dimension. *Phys. Rev. Lett.*, 83:3370–3373, 1999.
- 1407 [16] Tania Robens and Tim Stefaniak. Lhc benchmark scenarios for the real higgs
1408 singlet extension of the standard model. *The European Physical Journal C*,
1409 76(5), May 2016.
- 1410 [17] Alex Sherstinsky. Fundamentals of recurrent neural network (RNN) and long
1411 short-term memory (LSTM) network. *CoRR*, abs/1808.03314, 2018.